AEROELASTIC FORMULATIONS FOR PERFORMANCE AND STABILITY PREDICTIONS OF HORIZONTAL AXIS WIND TURBINES

SCUOLA DOTTORALE IN INGEGNERIA

SEZIONE DI INGEGNERIA MECCANICA E INDUSTRIALE

CICLO XXVIII

AEROELASTIC FORMULATIONS FOR PERFORMANCE AND STABILITY PREDICTIONS OF HORIZONTAL AXIS WIND TURBINES

Angelo Calabretta

Tutor: Prof. Massimo Gennaretti

Tutor esterno: Luca Greco

Tutor esterno: Claudio Testa

ACKNOWLEDGEMENTS

The activity carried out for the present PhD work has been supported by CNR-INSEAN (Marine Technology Research Institute - National Research Council, Italy) in the framework of the Flagship Project 'RITmare, Italian Research for the sea' funded by the Italian Ministry of University and Research (MIUR). The author also wish to thank the research project Safrema Energy llc. for providing experimental results on oscillating wing performed at CNR-INSEAN towing tank.

Contents

List of Figures

List of Tables

Abstract

Today wind turbines are assuming great importance in the generation of electrical power worldwide. Due to the increased dimensions of the rotor blades, design of a wind turbine is a very complex and multidisciplinary task in which aeroelasticity plays a crucial role. In this context, the present thesis proposes the development of numerical aeroelastic tools for the analysis of performance, response and aeroelastic stability of horizontal-axis wind turbines. The objective of the present work is the formulation of numerical solvers combining accuracy and numerical efficiency that can be useful in the preliminary phase of the design process. A nonlinear beam model for blades structural dynamics is coupled with different aerodynamic models of increasing complexity able to predict unsteady effects due to wake vorticity, flow separations and dynamic stall. Several computational fluid dynamics and structural dynamics coupling approaches are investigated to take into account rotor wake inflow influence on downwash. Sectional steady aerodynamic coefficients are extended to high angles of attack in order to characterize wind turbine operations in deep stall regimes. The first aeroelastic tool proposed is based on a spectral approach in which the Galerkin method is applied to the aeroelastic differential system; to improve the efficiency of the proposed solver, a novel approach for the spatial integration of additional aerodynamic states, related to wake vorticity and dynamic stall, is introduced and assessed. The second aeroelastic formulation is based on the Finite Element Method (FEM); Hamilton's principle is applied to derive blade equations of motion on which a devoted fifteen-degrees-of-freedom finite element is introduced to model kinematics and elastic behavior of rotating blades. Spatial discretization of the aeroelastic equations is carried-out to derive a set of coupled nonlinear ordinary differential equations solved by a time marching algorithm. Different time marching schemes are discussed and compared. Due to the aeroelastic similarity between wind turbine and helicopter rotor blades, validation of the FEM-based solver firstly deals with the response and performance of helicopter rotors in hovering and forward flight. Then, the performance of a wind turbine examined in terms of blade elastic response and delivered thrust and power is predicted and the results are compared with those provided by the solver based on modal approach, as well as with experimental data.

Chapter 1

Introduction

Wind is a source of renewable energy coming from air flowing across the earth's surface and, historically, people have always used this kind of energy. Probably, the most important application has been ship propulsion using sails before the invention of the steam and the internal combustion engines. Wind has also been used in windmills to grind grain (Figure 1.1) or to pump water for irrigation. At the beginning of the twentieth century, electricity came into use and windmills gradually became wind turbines as the rotor was connected to an electric generator. The first electrical grids were characterized by high losses, thus electricity had to be generated close to the site of use. However, diesel engines and steam turbines gradually took over the production of electricity and only during the two world wars, when the supply of fuel was scarce, wind power flourished again. The development of more efficient wind turbines was pursued in several countries as Germany, United States, France, United Kingdom, Denmark and with the oil crisis in 1973, wind turbines became interesting again for many countries that wanted to be less dependent on oil imports. Thus, many national research programs were initiated to investigate the possibilities of utilizing wind energy.

Figure 1.1: Windmills

Today wind turbines are playing an increasing role in the generation of electrical power worldwide. According to the orientation of the rotor shaft axis, wind turbines can be divided into horizontal (HAWT) and vertical (VAWT) axis. The first (see Figure 1.2a) have the shaft (almost) parallel to the ground whilst the second (Figure 1.2b) in vertical position. HAWTs, which are the most common types, are more efficient compared to the VAWTs and they can be easily scaled up to the large size required for commercial production; however, VAWTs have the advantage that they can generate power with wind from any direction without using a yaw control mechanism.

(a) Horizontal Axis Wind Turbine (b) Vertical Axis Wind Turbine

Figure 1.2: Modern wind turbines

Offshore installations of wind turbines are assuming a greater importance, due to many advantages with respect to onshore applications: the availability of wind resource is more frequent and more powerful; offshore wind farms (group disposition of wind turbines, see Figure 1.3) have smaller negative impact on landscape aesthetics since they are not completely visible from the shore; transport of big wind turbine components is significantly easier with ships than trucks or trains on land. Thus, offshore wind energy market is constantly growing, despite the high construction costs of new projects.

Figure 1.3: Offshore wind farm

Wind represents a good alternative to more conventional energy sources: electricity produced by the wind doesn't generate CO_2 emissions; it can be combined with a diesel engine to save fuel; in a windy site, the price of the produced electricity is competitive with the production price from more common methods. However, drawbacks are also present: noise, especially due to the aerodynamics of rotating blades, visual and nature supplies which can reduce energy production if sufficient wind is not present.

The design of a wind turbine is a complex multidisciplinary problem; indeed, in order to obtain a good trade-off between performance and costs, many considerations and analysis in different research and design areas have to be made and taken into account. Wind turbine power generation is directly connected with the aerodynamic performance of the blade, which is strictly related to its structural dynamics; thus, with today larger turbines, structural aspects become increasingly important [1, 2]. However, the interest in multidisciplinary design is not just limited to aero-structural optimization: electronical devices to control wind turbine are continuously developed (i.e. the yaw mechanism to keep the rotor in the flow direction), blade materials to increase performance are investigated and also the optimal placement of a wind turbine is analyzed [3].

From an aeroelastic point of view, wind turbines rotor modelling represents a challenging task involving different physical aspects. The accurate prediction of unsteady airloads under attached and separated flow conditions as well as structural behavior requires suitable modelling and devoted solution techniques to characterize rotor stability and response. Wind turbines operations are also affected by atmospheric turbulence, ground boundary layer, temporal and spatial variations in wind and thermal convection. The influence of an upstream unsteady wake emanated by the tower or another wind turbine also represents a problem to correctly predict wind turbine performance. Thus, reliable and economic design of wind turbines that can operate over long periods of time is very difficult. Moreover, the increasing size of commercial wind turbines (today rotor diameter size reach values higher than 160 m [4]) leads to more flexible and lower stiffness blades and hence to strong coupling between aerodynamics and structural dynamics. Thus, aeroelasticity has become a critical issue in the preliminary design of wind turbines. Due to the increased dimensions of wind turbine blades, many important factors have to be taken into account in the preliminary design phase: aeroelastic problem linearization is valid under the assumption of small deformations and displacements, whilst flexibility of the modern blades leads to

important nonlinearities that cannot be ignored in the numerical solution; the introduction of active aeroelastic control technology represents a possible solution for large wind turbines since it can alleviate blade loads and increase the turbine blade length without exceeding fatigue damage on the system, and resulting in an increased power production; due to the abundant wind energy on the sea and the decreasing cost per kilowatt, greater consideration and interest on offshore applications is posed, thus, aerohydroelastic models have to be developed to predict interactions between the floating platform and wave loads.

Advanced design tools are required to perform fast aeroelastic response simulations of the entire wind turbine, including tower, drive train, rotor and control system. Hence, multidisciplinary numerical tools with good levels of accuracy and operating at low computational costs are of great interest for designers. Successful analysis and design of wind turbines relies on adequate aerodynamics and structural dynamics rotor modelling, including application of suitable techniques for space and time aeroelastic system integration [5]. Concerning rotor aerodynamics modelling, solution tools able to take into account unsteady operating conditions induced by both wind gradients and motion of deformable blades, are mandatory. State-of-the-art aerodynamics codes for wind turbines design involve well assessed engineering methods based on enhanced Blade Element Momentum Theory (BEMT) techniques, that include tuned-up corrections to model blade tip flow, wake dynamic inflow and dynamic stall [6]. More recently, Computational Fluid Dynamics (CFD) tools based on Reynolds Averaged Navier-Stokes Equations (RANSE), and Direct and Large Eddy Simulation (DES and LES) aerodynamics solvers have shown the capability to achieve a physically consistent description of turbine flow-field, thus interest in coupled CFD-CSD (Computational Structural Dynamics) techniques is increasing as well [7, 8]. Nevertheless, due to the high computational costs, they are not well suited for aeroelastic analyses in practical preliminary design and aero-servo-elastic applications [9]. In this scenario, three-dimensional, potential-flow methods [10, 11] represent an advanced convenient alternative to BEMT codes. Specifically, solvers based on Boundary Element Methods (BEM) efficiently predict rotor airloads and wake inflow in attached flow operating conditions [12]. A drawback of these methods is that viscosity effects (like, for instance, unsteady flow separation occurring in off-design operations) can be only approximately described through inclusion of engineering models, such as dynamic inflow or dynamic stall models. From a blade structural point of view, Friedmann [13] derived the earliest formulation to describe wind turbine blade motion; the blade was assumed to be an elastic beam fixed to the hub and its dynamics was governed by a set of coupled flap-lag-torsional nonlinear partial differential equations. Hodges and Dowell [14], using Hamilton's principle, derived nonlinear equations for an hingeless helicopter rotor blade undergoing moderate displacements, and this formulation was then extended by Kallesoe [15] to wind turbine rotor blades. Specific codes for the construction of 3D finite element models of wind turbine blades were developed [16]; however, due to the high computational effort, blades were modeled as a series of 1D equivalent beam elements in many aeroelastic codes.

These considerations have inspired the present work with the objective of developing aeroelastic models to predict performance of horizontal axis wind turbines in steady or unsteady conditions. The proposed solvers can be suitably positioned amongst the current literature on the subject and are based on well-assessed structural and sectional aerodynamics. The first aeroelastic formulation proposed is based on a spectral approach; the aerodynamic model is coupled with a nonlinear, integro-differential formulation governing structural dynamics of bending-torsional blades subject to moderate deformations. The main distinguishing feature of this model is the use of a three-dimensional, unsteady BEM solver for incompressible, potential, attached flows, combined with the widely used Beddoes-Leishman (B-L) dynamic stall model, also including leading and trailing edge

separation effects. In the absence of a well assessed and accepted procedure for including three-dimensional effects in aerodynamic load formulations based on sectional theories, different coupling strategies are proposed and investigated in order to assess their effectiveness in the prediction of global (rotor thrust and power) and local (blade loading) quantities by comparison with available experimental and numerical data. The resulting aeroelastic differential system is integrated through the Galerkin approach, with the introduction of a novel, and computationally efficient, technique for spatial integration of additional aerodynamic states related to wake vorticity and dynamic stall. Steady-periodic rotor response is evaluated by a harmonic balance technique at reduced computational costs, whilst a time marching solution algorithm is applied to evaluate responses to arbitrary inputs. Deep stall regimes are analyzed by extension of airfoil static coefficients to high angles of attack based on flat plate theory, whilst centrifugal effects are considered by widely used empirical corrections. The second formulation proposed is based on the Finite Element Method (FEM) technique and is intended for moderate displacements. The level of accuracy in the physical description of the fluid-structure interaction makes this approach among those having a leading position in wind turbine aeroelastic simulations; furthermore, analyzing blades with complex geometries, the FEM technique gives the possibility to increase the number of elements in specific blade portions. Blade aerodynamics is simulated using different quasi-steady and unsteady sectional models, whilst the structural dynamics of the blade is modeled using the same formulation of the first model. Wake inflow effects are modeled by the simple momentum theory approach, by the Drees model, or by a more advanced description obtained through an unsteady, three dimensional, free wake panel method. Aeroelastic blade equations are firstly obtained in weak-form through the application of Hamilton's principle; the resulting nonlinear partial-integral equations of motion are then reduced to a set of nonlinear ordinary differential equations by the spatial FEM-based discretization, then solved through a time-marching scheme. Due to the aeroelastic similarity between helicopter and wind turbine rotor blades, validation results obtained with this formulation with respect to literature data are firstly presented by studying the structural and aeroelastic behavior of helicopter main rotors in hovering and forward flight; finally, blade response and delivered performance of a horizontal axis wind turbine are predicted.

In the following chapters, the developed aeroelastic formulations will be described in detail and results obtained from the numerical applications will be discussed. In particular, in the next chapter FEM-based rotor aeroelastic modelling will be proposed and the Galerkin method, applied in the aeroelastic solver based on a spectral approach, is also presented. Several sectional aerodynamic formulations will be discussed in Chapter 3, where the enhancement of 2D loads modelling for three dimensional applications will be also proposed along with semi empirical corrections for high angle of attack regimes. Finally, results obtained by the numerical applications of the proposed tools will be collected in Chapter 4 where the validation of the aeroelastic formulations will be outlined considering helicopter and wind turbine rotors in different operating conditions.

Chapter 2

Rotor aeroelastic modelling

In the present chapter, the FEM-based formulation to study rotor blades aeroelasticity is presented. Firstly, reference frames are introduced, then the Hamilton's principle is applied to derive the equations of blade motion, forced by the aerodynamic loads. These equations are written in nondimensional form to avoid scaling issues, and terms up to second-order are kept according to the ordering scheme presented. A devoted fifteen-degrees of freedom finite element for the spatial discretization of the blade dynamics is introduced and the methodology used to obtain the generalized aerodynamic nodal forces is discussed. The set of nonlinear ordinary differential equations governing rotor aeroelasticity are solved by a time marching technique.

The last section of this chapter deals with the introduction of the aeroelastic formulation based on a spectral approach; the Galerkin method applied to the resulting aeroelastic differential system is presented.

2.1 Reference frames definition

The following frames of reference are used herein (see Figure 2.1):

- **Hub-fixed non rotating** (X_H, Y_H, Z_H): centered at the rotor hub with unit vectors $\hat{I}_H$, $\hat{J}_H$, $\hat{K}_H$.
- **Hub-rotating** (X, Y, Z): has the origin coincident with (X_H, Y_H, Z_H) frame and rotates about the Z_H axis with a constant angular velocity $\Omega\hat{K}$. Its unit vectors are indicated as $\hat{I}$, $\hat{J}$, $\hat{K}$. The transformation between the non rotating and rotating system is defined as

$$\left\{ \begin{array}{c} \hat{I} \\ \hat{J} \\ \hat{K} \end{array} \right\} = \left[\begin{array}{ccc} \cos\psi & \sin\psi & 0 \\ -\sin\psi & \cos\psi & 0 \\ 0 & 0 & 1 \end{array} \right] \left\{ \begin{array}{c} \hat{I}_H \\ \hat{J}_H \\ \hat{K}_H \end{array} \right\} = \mathbf{T}_{RH} \left\{ \begin{array}{c} \hat{I}_H \\ \hat{J}_H \\ \hat{K}_H \end{array} \right\} \tag{2.1}$$

  where the azimuth angle ψ is equal to Ωt.

- **Undeformed blade** (x, y, z): has the origin at the hub, is fixed with the undeformed blade and is rotated about the Y axis of the precone angle β_{pc}. The x axis is coincident with the elastic axis of the blade and the y axis is in the plane of rotation pointed towards the leading edge of the blade. Its unit vectors are $\hat{i}$, $\hat{j}$, $\hat{k}$. The coordinate transformation between the hub-fixed rotating and the undeformed blade reference

frame is

$$\left\{ \begin{array}{c} \hat{i} \\ \hat{j} \\ \hat{k} \end{array} \right\} = \left[\begin{array}{ccc} \cos\beta_{pc} & 0 & \sin\beta_{pc} \\ 0 & 1 & 0 \\ -\sin\beta_{pc} & 0 & \cos\beta_{pc} \end{array} \right] \left\{ \begin{array}{c} \hat{I} \\ \hat{J} \\ \hat{K} \end{array} \right\} = \mathbf{T}_{UR} \left\{ \begin{array}{c} \hat{I} \\ \hat{J} \\ \hat{K} \end{array} \right\} \tag{2.2}$$

The transformation matrix from the hub-fixed non rotating frame of reference to the undeformed blade reference is achieved by combining transformation matrices in equations (2.1) and (2.2) to obtain $\mathbf{T}_{UH} = \mathbf{T}_{UR}\mathbf{T}_{RH}$.

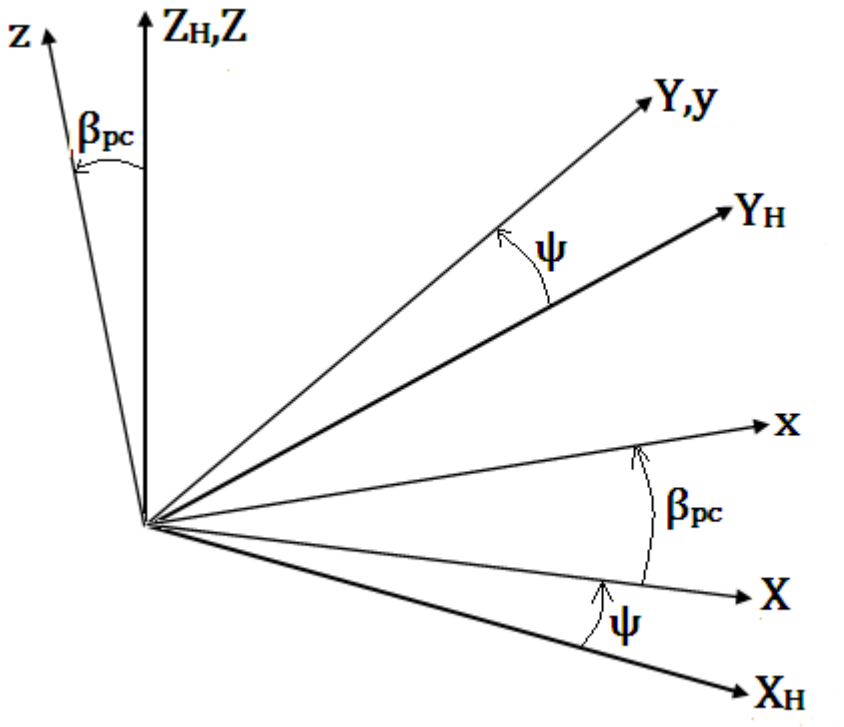

Figure 2.1: Definition of frames of reference: hub fixed non rotating (X_H, Y_H, Z_H), hub rotating (X, Y, Z) and undeformed blade (x, y, z)

– **Deformed blade** (ξ, η, ζ): η and ζ have origin on the elastic axis and are principal axes of the cross section; the corresponding unit vectors are $\hat{i}_\xi$, $\hat{j}_\eta$, $\hat{k}_\zeta$.

Blade section elastic displacements are defined in Figure 2.2. An adequate description of the deformed blade requires six variables: three translational and three rotational, and any out of plane deformations of the cross section. Using the Eulero-Bernoulli beam assumption, out of plane deformations are neglected, which results in plane sections remaining plane after deformation; a further simplification consists in expressing two of the three angles as derivatives of the deflection variables. Thus four deformation variables, three deflections and one rotational angle, completely determine the deformed geometry. A point P on the undeformed elastic axis undergoes deflections u, v, w in the x, y, z directions, respectively, and moves to a point P'. Then blade cross

section containing P' is subjected to a rotation θ_1 about the deformed elastic axis. The total blade pitch is defined as

$$\theta_1 = \theta_0 + \hat{\phi} \tag{2.3}$$

where θ_0 is the rigid pitch angle due to cyclic and collective controls (if present) and pretwist, while $\hat{\phi}$ is the elastic twist. Rigid pitch angle expression for a blade with linear pretwist is

$$\theta_0 = \theta_{root} + \theta_{tw} x + \theta_{coll} + \theta_{1c} \cos\psi + \theta_{1s} \sin\psi \tag{2.4}$$

where θ_{root} is the pitch at blade root, θ_{tw} is blade linear pretwist, x is the nondimensional position along the blade span in the undeformed frame of reference, θ_{coll} is collective pitch, θ_{1c} and θ_{1s} are cyclic pitch controls. The elastic twist is defined as

$$\hat{\phi} = \phi - \int_0^x \frac{\partial w}{\partial x} \frac{\partial^2 v}{\partial x^2} dx \tag{2.5}$$

where ϕ is the elastic twist about the undeformed elastic axis, whilst $\hat{\phi}$ is defined about the deformed elastic axis. The nonlinear term appearing in the above equation is designed as *kinematic pitch rotation* in [17]. In the following, the ordering scheme will allow $\hat{\phi}$ to be simplified to ϕ, due to moderate deflections and to the nonlinearity of the term.

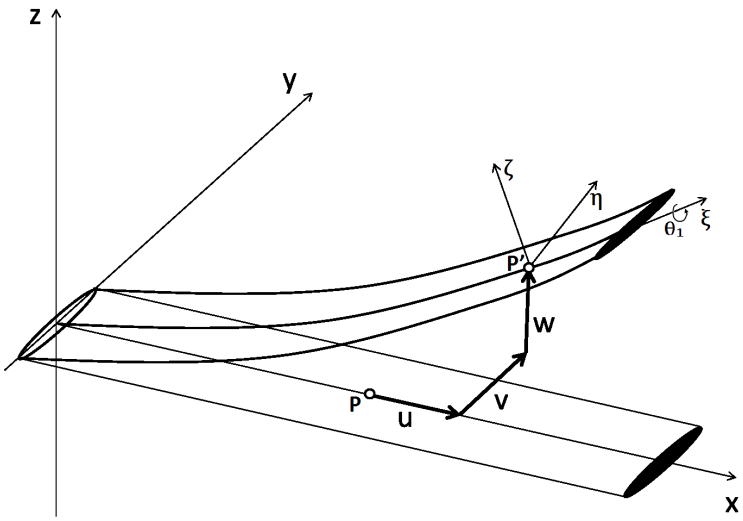

Figure 2.2: Definition of blade elastic displacements and undeformed/deformed blade frames of reference

Following [18], the coordinate transformation between the undeformed and the deformed blade reference frames is given by

$$\left\{\begin{array}{c}\hat{i}_\xi\\ \hat{j}_\eta\\ \hat{k}_\zeta\end{array}\right\}=\left[\begin{array}{ccc}\cos\bar{\beta}\cos\bar{\zeta} & \cos\bar{\beta}\sin\bar{\zeta} & \sin\bar{\beta}\\ -\sin\bar{\theta}\sin\bar{\beta}\cos\bar{\zeta}-\cos\bar{\theta}\sin\bar{\zeta} & \cos\bar{\theta}\cos\bar{\zeta}-\sin\bar{\zeta}\sin\bar{\beta}\sin\bar{\theta} & \cos\bar{\beta}\sin\bar{\theta}\\ -\cos\bar{\theta}\sin\bar{\beta}\cos\bar{\zeta}+\sin\bar{\theta}\sin\bar{\zeta} & -\sin\bar{\theta}\cos\bar{\zeta}-\sin\bar{\zeta}\sin\bar{\beta}\cos\bar{\theta} & \cos\bar{\beta}\cos\bar{\theta}\end{array}\right]\left\{\begin{array}{c}\hat{i}\\ \hat{j}\\ \hat{k}\end{array}\right\}=\mathbf{T}_{DU}\left\{\begin{array}{c}\hat{i}\\ \hat{j}\\ \hat{k}\end{array}\right\} \tag{2.6}$$

where the Euler angles $\bar{\zeta}$, $\bar{\beta}$, $\bar{\theta}$ can be written in terms of blade deformation as

$$\begin{array}{cc}\cos\bar{\zeta}=\frac{\sqrt{1-v'^2-w'^2}}{\sqrt{1-w'^2}} & \sin\bar{\zeta}=\frac{v'}{\sqrt{1-w'^2}}\\ \cos\bar{\beta}=\sqrt{1-w'^2} & \sin\bar{\beta}=w'\\ \multicolumn{2}{c}{\bar{\theta}=\theta_1}\end{array} \tag{2.7}$$

Substituting the above relations and simplifying to second order terms yields the transformation matrix between deformed and undeformed blade positions:

$$\mathbf{T}_{DU}=\left[\begin{array}{ccc}1-\frac{v'^2}{2}-\frac{w'^2}{2} & v' & w'\\ -v'\cos\bar{\theta}-w'\sin\bar{\theta} & \left(1-\frac{v'^2}{2}\right)\cos\bar{\theta}-v'w'\sin\bar{\theta} & \left(1-\frac{w'^2}{2}\right)\sin\bar{\theta}\\ v'\sin\bar{\theta}-w'\cos\bar{\theta} & -\left(1-\frac{v'^2}{2}\right)\sin\bar{\theta}-v'w'\cos\bar{\theta} & \left(1-\frac{w'^2}{2}\right)\cos\bar{\theta}\end{array}\right] \tag{2.8}$$

2.2 Nondimensionalization and ordering scheme

The present formulation is written in nondimensional form. This avoids scaling problems during computations and increases the generality of the analysis. The fundamental physical quantities are nondimensionalized by the reference parameters given in Table 2.1 where R is the blade radius, m_0 and Ω_0 are the reference mass for unit length and angular speed, respectively, that can be different from the blade mass m, and the rotor angular speed Ω.

Physical quantity	**Reference parameter**
Length	R
Time	$1/\Omega$
Mass for unit length	m_0
Velocity	ΩR
Acceleration	$\Omega^2 R$
Force	$m_0\Omega_0^2 R^2$
Moment	$m_0\Omega_0^2 R^3$
Energy or Work	$m_0\Omega_0^2 R^3$

Table 2.1: Nondimensionalization of physical quantities

The azimuth angle ψ can be considered as the nondimensional time, therefore, time derivatives are written as

$$\begin{array}{c}(\dot{}) = \frac{\partial()}{\partial t}=\frac{\partial()}{\partial\psi}\frac{\partial\psi}{\partial t}=\Omega\frac{\partial()}{\partial\psi}\\ (\ddot{}) = \frac{\partial^2()}{\partial t^2}=\frac{\partial^2()}{\partial\psi^2}\frac{\partial^2\psi}{\partial t^2}=\Omega^2\frac{\partial^2()}{\partial\psi^2}\end{array} \tag{2.9}$$

In deriving a nonlinear equations system, it is necessary to neglect higher-order terms to avoid over-complicating the equations of motion. To this aim, the same ordering scheme used in [14] has been adopted in this work;

specifically, terms up to second order are retained in the analysis by introducing the nondimensional quantity ϵ, such that $\epsilon \ll 1$. Some third order terms related to elastic torsion are also retained in the energy expressions. The order of magnitude of the non dimensional quantities is:

$$\begin{gathered}
\frac{EA}{m_0\Omega_0^2R^2} = O\left(\epsilon^{-2}\right) \\
\frac{v}{R}, \frac{w}{R}, \hat{\phi}, \beta_{pc}, \frac{k_A}{R}, \frac{k_{m1}}{R}, \frac{k_{m2}}{R}, \alpha_s, \lambda, \frac{EB_2}{m_0\Omega_0^2R^5}, \frac{EC_2}{m_0\Omega_0^2R^5} = O\left(\epsilon\right) \\
\frac{e_d}{R}, \frac{e_g}{R}, \frac{e_a}{R} = O\left(\epsilon^{3/2}\right) \\
\frac{u}{R}, \frac{EB_1}{m_0\Omega_0^2R^6}, \frac{EC_1}{m_0\Omega_0^2R^6}, \lambda_T = O\left(\epsilon^2\right) \\
\frac{x}{R}, \frac{m}{m_0}, \frac{\partial}{\partial\psi}, \frac{\partial}{\partial x}, \mu, cos\psi, sin\psi, \theta_0, \theta_{tw}, \theta_{1c}, \theta_{1s}, \frac{EI_y}{m_0\Omega_0^2R^4}, \frac{EI_z}{m_0\Omega_0^2R^4}, \frac{GJ}{m_0\Omega_0^2R^4} = O\left(1\right)
\end{gathered} \tag{2.10}$$

where EA is the axial stiffness, EI_y and EI_z are flap and lag bending stiffness, respectively and GJ is the torsional stiffness. The antisymmetric warping function λ_T [14], representing the out of plane distortions of the section, specifies the distribution of the axial warping displacements around the cross section, $EC_1$and EC_2 are constants related to the warping rigidity of the beam section, $EB_1$and EB_2 are other sectional constant due to blade pitch [18], k_A is the radius of gyration, k_{m1} and k_{m2} are the flapwise and chordwise mass moments of inertia for unit blade length, respectively, whereas α_s represents the shaft angle, λ the total induced inflow and μ the advance ratio defined as $\mu = \frac{V\cos\alpha_S}{\Omega R}$. Finally, three sectional offset are introduced: the aerodynamic offset e_d between the aerodynamic and elastic centres positive backward, the blade center of gravity offset e_g from the elastic axis (positive forward) and the tensile axis offset e_a from the elastic axis (positive forward). The ordering scheme is systematically and consistently adopted in the calculation of the total energy.

2.3 Aeroelastic formulation: Hamilton's Principle

A nonlinear elastic blade model ([14], [19]) is used in the developed aeroelastic solver. The blade is assumed to be a long, straight, slender, elastic, homogeneous and isotropic beam undergoing flap and lag bending, elastic twist (or torsion) and axial deformation. The theory is intended for moderate displacements. The analysis is developed for an isolated rotor having blades with pretwist, precone and chord-wise offsets of the center of mass, aerodynamic center, and tension center from the elastic axis. The possible presence of hinge offset is considered. Structural dissimilarities among rotor blades are neglected whereas advanced tip shapes, such as swept-tip or tapered-tip, are not modeled. Governing equations of motion are derived from the generalized Hamilton's principle applicable to non-conservative systems

$$\delta\Pi = \int_{\psi_1}^{\psi_2} \left(\delta U - \delta T - \delta W\right) d\psi = 0 \tag{2.11}$$

with $\psi_{1,2}$ defining the azimuth angles between which motion is analyzed whereas δU, δT and δW represent the virtual variation of the strain energy, kinetic energy and work done by external forces, respectively, written as the sum of contributions from each rotor blade. For the $b-th$ blade, equation (2.11) is written in the discretized form as

$$\delta\Pi = \int_{\psi_1}^{\psi_2} \left[\sum_{b=1}^{N_b} \left(\delta U_b - \delta T_b - \delta W_b\right)\right] d\psi \tag{2.12}$$

where N_b is the total number of rotor blades. The following sections describe the derivations of each term in

(2.12).

2.3.1 Strain energy

Since each rotor blade is considered to be a long slender isotropic beam, the uniaxial stress assumption ($\sigma_{yy} = \sigma_{yz} = \sigma_{zz} = 0$) is applicable. Using Hooke's law, the relationship between stresses and strains is given by

$$\begin{aligned} \sigma_{xx} &= E\epsilon_{xx} \\ \sigma_{x\eta} &= G\epsilon_{x\eta} \\ \sigma_{x\zeta} &= G\epsilon_{x\zeta} \end{aligned} \tag{2.13}$$

where ϵ_{xx} is the axial strain, whilst $\epsilon_{x\eta}$ and $\epsilon_{x\zeta}$ are engineering shear strains.
Under these assumptions, strain energy variation of the $b-th$ blade can be expressed as

$$\delta U_b = \int_0^R \iint_A \left(E\epsilon_{xx}\delta\epsilon_{xx} + G\epsilon_{x\eta}\delta\epsilon_{x\eta} + G\epsilon_{x\zeta}\delta\epsilon_{x\zeta}\right) d\eta d\zeta\, dx \tag{2.14}$$

where the general nonlinear strain displacement equations to second order are [14]

$$\begin{aligned} \epsilon_{xx} = u' + \tfrac{v'^2}{2} + \tfrac{w'^2}{2} - \lambda_T\phi'' + \left(\eta^2+\zeta^2\right)\left(\theta_0'\phi' + \tfrac{\phi'^2}{2}\right) + \\ -v''\left[\eta cos\left(\theta_0+\hat{\phi}\right) - \zeta sin\left(\theta_0+\hat{\phi}\right)\right] - w''\left[\eta sin\left(\theta_0+\hat{\phi}\right) + cos\left(\theta_0+\hat{\phi}\right)\right] \end{aligned} \tag{2.15}$$

$$\epsilon_{x\eta} = -\left(\zeta + \frac{\partial\lambda_T}{\partial\eta}\right)\phi' \tag{2.16}$$

$$\epsilon_{x\zeta} = \left(\eta - \frac{\partial\lambda_T}{\partial\zeta}\right)\phi' \tag{2.17}$$

The axial deflection u, can be written as the sum of a contribution from the elastic axis axial deflection (u_e) and another one from the foreshortening effect which results in a kinematic axial deflection due to flap and lag deflections of the section:

$$u = u_e - \frac{1}{2}\int_0^x \left(v'^2 + w'^2\right) dx \tag{2.18}$$

For the $b-th$ blade, a virtual variation of the degrees of freedom yields a virtual variation of strain energy; the resulting expression in nondimensional form is given by

$$\tfrac{\delta U_b}{m_0\Omega_0^2R^3} = \int_0^1 \left(U_{u_e'}\delta u_e' + U_{v''}\delta v'' + U_{w'}\delta w' + U_{w''}\delta w'' + U_{\hat{\phi}}\delta\hat{\phi} + U_{\hat{\phi}'}\delta\hat{\phi}' + U_{\hat{\phi}''}\delta\hat{\phi}''\right) d\bar{x} \tag{2.19}$$

where all quantities are written in nondimensional form:

$$U_{u_e'} = EA\left[u_e' + k_A^2\theta_0'\left(\hat{\phi}' + w'v''\right) + k_A^2\frac{\hat{\phi}'}{2}\right] - EAe_a\left[v''\left(\cos\theta_0 - \hat{\phi}\sin\theta_0\right) + w''\left(\sin\theta_0 + \hat{\phi}\cos\theta_0\right)\right] \tag{2.20}$$

$$\begin{aligned} U_{v''} = v''\left(EI_z\cos^2\theta_0 + EI_y\sin^2\theta_0\right) + w''\left(EI_z - EI_y\right)\cos\theta_0\sin\theta_0 - EAe_a u_e^{'}\left(\cos\theta_0 - \hat{\phi}\sin\theta_0\right) + \\ -\hat{\phi}^{'}EB_2\theta_0^{'}\cos\theta_0 + w''\hat{\phi}\left(EI_z - EI_y\right)\cos 2\theta_0 - v''\hat{\phi}\left(EI_z - EI_y\right)\sin 2\theta_0 + \\ + \left(GJ + EB_1\theta_0^{'2}\right)\hat{\phi}^{'}w' + EAk_A^2\theta_0^{'}w'u_e^{'} \end{aligned} \tag{2.21}$$

$$U_{w'} = \left(GJ + EB_1\theta_0^{'2}\right)\hat{\phi}^{'}v'' + EAk_A^2\theta_0^{'}v''u_e^{'} \tag{2.22}$$

$$\begin{aligned} U_{w''} = w''\left(EI_y\cos^2\theta_0 + EI_z\sin^2\theta_0\right) + v''\left(EI_z - EI_y\right)\cos\theta_0\sin\theta_0 - EAe_a u_e^{'}\left(\sin\theta_0 + \hat{\phi}\cos\theta_0\right) + \\ -\hat{\phi}^{'}EB_2\theta_0^{'}\sin\theta_0 + w''\hat{\phi}\left(EI_z - EI_y\right)\sin 2\theta_0 + v''\hat{\phi}\left(EI_z - EI_y\right)\cos 2\theta_0 + \end{aligned} \tag{2.23}$$

$$U_{\hat{\phi}} = w''^2\left(EI_z - EI_y\right)\cos\theta_0\sin\theta_0 + v''w''\left(EI_z - EI_y\right)\cos 2\theta_0 - v''^2\left(EI_z - EI_y\right)\cos\theta_0\sin\theta_0 \tag{2.24}$$

$$U_{\hat{\phi}'} = \left(GJ + EB_1\theta_0^{'2}\right)w'v'' + \left(GJ + EB_1\theta_0^{'2}\right)\hat{\phi}^{'} + EAk_A^2\left(\theta_0^{'} + \hat{\phi}^{'}\right)u_e^{'} - EB_2\theta_0^{'}\left(v''\cos\theta_0 + w''\sin\theta_0\right) \tag{2.25}$$

$$U_{\hat{\phi}''} = EC_1\hat{\phi}^{''} + EC_2\left(w''\cos\theta_0 - v''\sin\theta_0\right) \tag{2.26}$$

For the sake of clarity, some terms of equation (2.19) are derived in Appendix A.

2.3.2 Kinetic energy

The kinetic energy of the $b-th$ blade, δT_b, depends on the blade velocity. This velocity is generally due to: blade motion relative to the hub, as well as the motion of the hub itself. This relationship is expressed mathematically as

$$\vec{V} = \vec{V}_b + \vec{V}_h \tag{2.27}$$

where $\vec{V}_b$ is the velocity of the blade relative to the hub and $\vec{V}_h$ is the velocity (at the blade) induced by the motion of the hub. Given a point P belonging to the undeformed blade elastic axis with coordinates (x, 0, 0), after the deformation it has moved to the point P' ($x + u$, v, w). Then the blade section undergoes a rotation θ_1 about the deformed elastic axis (see Figure 2.2). The components of the position vector $\vec{r}$ of a material blade point P after deformation are indicated as (x_1, y_1, z_1) in the undeformed blade coordinate system

$$\vec{r} = x_1\hat{i} + y_1\hat{j} + z_1\hat{k} \tag{2.28}$$

where

$$\begin{aligned} x_1 &= u + x - \lambda_T \phi' - v'(y_1 - v) - w'(z_1 - w) \\ y_1 &= v + (y_1 - v) \\ z_1 &= w + (z_1 - w) \end{aligned} \tag{2.29}$$

in which $v'(y_1 - v)$ and $w'(z_1 - w)$ are radial shortenings due to lagwise and flapwise deflections respectively, whilst the deformations due to the rotation of the section about the deformed elastic axis are defined as

$$\begin{aligned} (y_1 - v) &= \eta cos\theta_1 - \zeta sin\theta_1 \\ (z_1 - w) &= \eta sin\theta_1 + \zeta cos\theta_1 \end{aligned} \tag{2.30}$$

Noting that the unit vectors in equation (2.28) depend on time, time derivation of the position vector $\vec{r}$ yields the following components of the absolute velocity of a blade point in the undeformed blade reference system

$$\begin{aligned} V_{bx} &= \dot{x}_1 - \Omega y_1 cos\beta_{pc} \\ V_{by} &= \dot{y}_1 + \Omega x_1 cos\beta_{pc} - \Omega z_1 sin\beta_{pc} \\ V_{bz} &= \dot{z}_1 + \Omega y_1 sin\beta_{pc} \end{aligned} \tag{2.31}$$

The variation of kinetic energy of the $b-th$ blade is given by

$$\delta T_b = \int_0^R \iint_A \left(\rho_s \vec{V}_b \cdot \delta\vec{V}_b\right) d\eta d\zeta \, dx \tag{2.32}$$

where A is the cross section and ρ_s represents its mass density. Substituting equation (2.31) in (2.32), the resulting nondimensional variation of kinetic energy is

$$\frac{\delta T_b}{m_0 \Omega_0^2 R^3} = \int_0^1 \mu_s \left(T_{u_e}\delta u_e + T_v \delta v + T_w \delta w + T_{v'}\delta v' + T_{w'}\delta w' + T_{\hat{\phi}}\delta\hat{\phi} + T_F\right) d\bar{x} \tag{2.33}$$

where

$$T_{u_e} = \frac{\Omega}{\Omega_0}(x + u_e + 2\dot{v} - \ddot{u}_e) \tag{2.34}$$

$$\begin{aligned} T_v = \tfrac{\Omega}{\Omega_0}\left[e_g\left(\cos\theta_0 + \ddot{\theta}_0 \sin\theta_0\right) + v - \hat{\phi} e_g \sin\theta_0 + 2\dot{w}\beta_{pc} + 2\dot{v}' e_g \cos\theta_0\right] + \\ + \tfrac{\Omega}{\Omega_0}\left[2\dot{w}' e_g \sin\theta_0 - \ddot{v} + \ddot{\hat{\phi}} e_g \sin\theta_0 - 2\dot{u}_e + 2\int_0^x (v'\dot{v}' + w'\dot{w}')\, d\xi\right] \end{aligned} \tag{2.35}$$

$$T_w = \frac{\Omega}{\Omega_0}\left[-x\beta_{pc} - \ddot{\theta}_0 e_g \cos\theta_0 - 2\dot{v}\beta_{pc} - \ddot{w} - \ddot{\hat{\phi}} e_g \cos\theta_0\right] \tag{2.36}$$

$$T_{v'} = \frac{\Omega}{\Omega_0}\left[-e_g\left(x\cos\theta_0 - \hat{\phi} x \sin\theta_0 + 2\dot{v}\cos\theta_0\right)\right] \tag{2.37}$$

$$T_{w'} = \frac{\Omega}{\Omega_0}\left[-e_g\left(x\sin\theta_0 + \hat{\phi} x \cos\theta_0 + 2\dot{v}\sin\theta_0\right)\right] \tag{2.38}$$

$$\begin{aligned} T_{\hat{\phi}} = \tfrac{\Omega}{\Omega_0}\left[-k_m^2 \ddot{\hat{\phi}} - \left(k_{m2}^2 - k_{m1}^2\right)\sin\theta_0\cos\theta_0 - x\beta_{pc} e_g \cos\theta_0 - v e_g \sin\theta_0 + v' x e_g \sin\theta_0\right] + \\ + \tfrac{\Omega}{\Omega_0}\left[-w' x e_g \cos\theta_0 + \ddot{v} e_g \sin\theta_0 - \hat{\phi}\left(k_{m2}^2 - k_{m1}^2\right)\cos 2\theta_0 - \ddot{w} e_g \cos\theta_0 - k_m^2 \ddot{\theta}_0\right] \end{aligned} \tag{2.39}$$

$$T_F = -\frac{\Omega}{\Omega_0}\left(x + 2\dot{v}\right)\int_0^x \left(v'\delta v' + w'\delta w'\right) d\xi \tag{2.40}$$

Some example of the procedure to obtain terms in equation (2.33) are presented in Appendix A.

2.3.3 External forces virtual work

External forces and moments on blades contribute to the virtual work on the system. In the present work only distributed aerodynamic loads are considered. Thus, for a given virtual variation of the degrees of freedom of the system, the virtual work (in nondimensional form) done by the aerodynamic loads recasts

$$\frac{\delta W_b}{m_0\Omega_0^2 R^3} = \int_0^1 \left(L_u^A\delta u + L_v^A\delta v + L_w^A\delta w + M_{\hat{\phi}}^A\delta\hat{\phi}\right) d\bar{x} = \int_0^1 \left(\delta\mathbf{u}^T\mathbf{L}_A\right) d\bar{x} \tag{2.41}$$

where $\delta\mathbf{u}^T = \left(\delta u,\, \delta v,\, \delta w,\, \delta\hat{\phi}\right)$ is the virtual elastic displacement and $\mathbf{L}_A^T = \left(L_u^A,\, L_v^A,\, L_w^A,\, M_{\hat{\phi}}^A\right)$ is the vector collecting sectional forces and moments referred to the deformed blade configuration, projected in the undeformed frame of reference (O_{xyz}). For clarity, the method used for the computation of aerodynamic forces and moment is discussed in detail in Section 2.4.2.

2.4 Blade equations of motion

2.4.1 Finite element discretization in space

Each blade is discretized into a number of beam elements, having fifteen degrees of freedom (DOFs) distributed over five element nodes (two boundary nodes and three internal nodes). There are six degrees of freedom at each element boundary node, corresponding to u (axial displacement), v (lag deflection), v' (lag bending-slope), w (flap deflection), w' (flap bending-slope) and $\hat{\phi}$ (twist) (see Figure 2.3 for details).

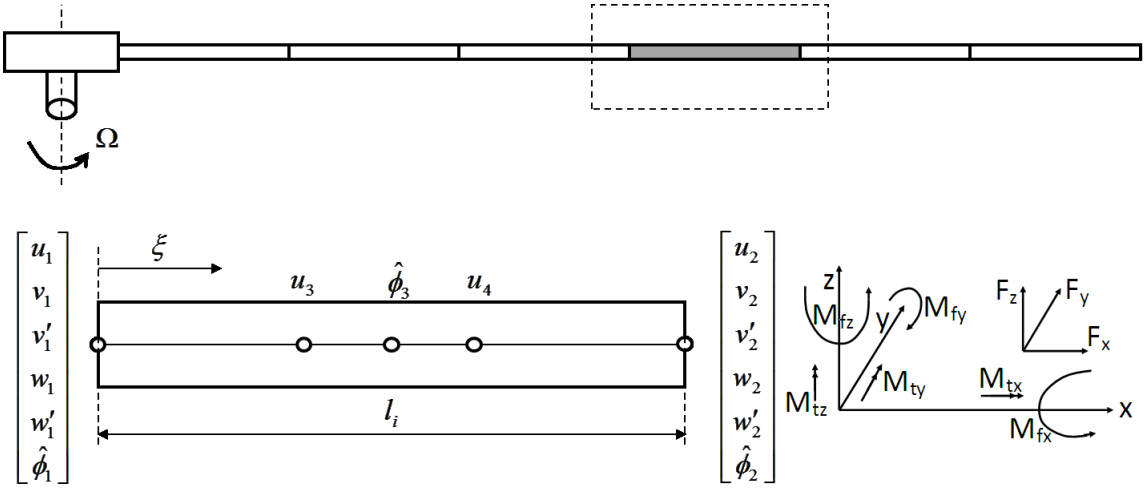

Figure 2.3: Sketch of the rotor blade discretized into finite elements (top); local nodes and elemental degrees of freedoms (bottom, left); elemental forces and moments (bottom, right).

Moreover, there are two internal nodes for the elastic axial deflection u and one internal node for the elastic twist $\hat{\phi}$ (Figure 2.3). These DOFs correspond to cubic variations of the axial and flap-lag bending deflections and quadratic variation of the elastic torsion. Between elements, continuity of displacements and slope for flap-lag deflections, as well as continuity of displacements for elastic twist and axial deflections, are assured. This kind of element provides physically consistent linear variations of bending and torsional moments, and quadratic variation of axial force within each element. Geometrical and structural properties are assumed to be constant within each element, with the exception of blade pre-twist. Such elemental DOFs comply with Hermite polynomials for lag/flap bendings and Lagrange polynomials for axial and torsional deflections. Thus, deflections distribution over a beam element may be expressed in terms of the elemental DOFs vector $\mathbf{q}_i^T = \left\{u_1, u_3, u_4, u_2, v_1, v_1', v_2, v_2', w_1, w_1', w_2, w_2', \hat{\phi}_1, \hat{\phi}_3, \hat{\phi}_2\right\}$, defined accordingly to the nodal topology shown in Figure 2.3. For the $i-th$ beam element, the elastic displacements is

$$\mathbf{u}_i(\xi,t) = \begin{Bmatrix} u(\xi) \\ v(\xi) \\ w(\xi) \\ \hat{\phi}(\xi) \end{Bmatrix} = \begin{bmatrix} \mathbf{H}_u(\xi) & 0 & 0 & 0 \\ 0 & \mathbf{H}(\xi) & 0 & 0 \\ 0 & 0 & \mathbf{H}(\xi) & 0 \\ 0 & 0 & 0 & \mathbf{H}_{\hat{\phi}}(\xi) \end{bmatrix} \mathbf{q}_i(t) \tag{2.42}$$

where the interpolating polynomials for the shape functions are:

$$\begin{aligned} \mathbf{H}_u^T &= \begin{Bmatrix} H_{u1} \\ H_{u2} \\ H_{u3} \\ H_{u4} \end{Bmatrix} = \begin{Bmatrix} -4.5\xi^3 + 9\xi^2 - 5.5\xi + 1 \\ 13.5\xi^3 - 22.5\xi^2 + 9\xi \\ -13.5\xi^3 + 18\xi^2 - 4.5\xi \\ 4.5\xi^3 - 4.5\xi^2 + \xi \end{Bmatrix} \\ \mathbf{H}^T &= \begin{Bmatrix} H_1 \\ H_2 \\ H_3 \\ H_4 \end{Bmatrix} = \begin{Bmatrix} 2\xi^3 - 3\xi^2 + 1 \\ l_i\left(\xi^3 - 2\xi^2 + \xi\right) \\ -2\xi^3 + 3\xi^2 \\ l_i\left(\xi^3 - \xi^2\right) \end{Bmatrix} \\ \mathbf{H}_{\hat{\phi}}^T &= \begin{Bmatrix} H_{\hat{\phi}1} \\ H_{\hat{\phi}2} \\ H_{\hat{\phi}3} \end{Bmatrix} = \begin{Bmatrix} 2\xi^2 - 3\xi + 1 \\ -4\xi^2 + 4\xi \\ 2\xi^2 - \xi \end{Bmatrix} \end{aligned} \tag{2.43}$$

in which ξ is the nondimensional local element position on the $i-th$ beam element.

In order to integrate equations (2.19), (2.33) and (2.41) along the span, let consider the following discretization procedure applied to a generic function $f(x)$ defined throughout the blade. Starting from the definition of a nondimensional radial position $\bar{x} = x/R$ (see Figure 2.4) in the undeformed frame of reference ranging from the hub to the blade tip ($0 \leq \bar{x} \leq 1$), introducing FEM discretization and defining a local nondimensional variable $\hat{\xi}$ on each element ($0 \leq \hat{\xi} \leq l_i/R$, where l_i is the dimensional length of the $i-th$ element), one obtains

$$\int_0^R f(x)\,dx = \int_0^1 f(\bar{x})\,d\bar{x} = \sum_{i=1}^{N} \int_{x_{Li}/R}^{(x_{Li}+l_i)/R} f(\bar{x})\,d\bar{x} = \sum_{i=1}^{N} \int_0^{l_i/R} f\left(\hat{\xi}\right) d\hat{\xi} \tag{2.44}$$

where x_{Li} represents the dimensional position on the blade of the left node of the $i-th$ element.
Finally, denoting with $\xi = \hat{\xi}R/l_i$ a new local nondimensional variable such that $0 \leq \xi \leq 1$, the final expression is obtained:

$$\int_0^R f(x)\,dx = \sum_{i=1}^{N} el_i \int_0^1 f(\xi)\,d\xi \tag{2.45}$$

where el_i is the nondimensional length of the $i-th$ element. The last integral is solved by the Gauss quadrature procedure that will be discussed later in this section.

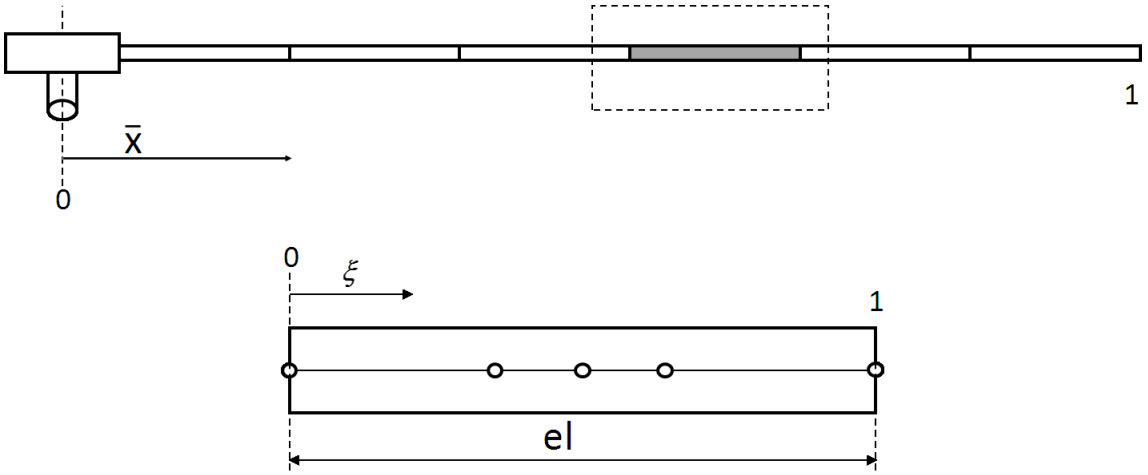

Figure 2.4: Definition of nondimensional coordinates along the blade

Applying FEM discretization to equation (2.12) and focusing the analysis on a single blade, the Hamilton Principle recasts

$$\delta\Pi = \int_{\psi_1}^{\psi_2} \left[\sum_{i=1}^{N} (\delta U_i - \delta T_i - \delta W_i)\right] d\psi = \int_{\psi_1}^{\psi_2} \left[\sum_{i=1}^{N} \Delta_i\right] d\psi = 0 \tag{2.46}$$

where subscript i indicates the $i-th$ element and N is the number of the spatial finite elements on the blade. By substituting relation $\mathbf{u}_i(\xi,t) = \mathbf{H}(\xi)\,\mathbf{q}_i(t)$ in equations (2.19), (2.33) and (2.41), the elemental variation Δ_i can be written in the following form:

$$\Delta_i = \delta\mathbf{q}_i^T \left(\hat{\mathbf{M}}\ddot{\mathbf{q}} + \hat{\mathbf{C}}\dot{\mathbf{q}} + \hat{\mathbf{K}}\mathbf{q} - \hat{\mathbf{F}}\right)_i \tag{2.47}$$

where $\hat{\mathbf{M}}_i$, $\hat{\mathbf{C}}_i$ and $\hat{\mathbf{K}}_i$ are elemental mass, gyroscopic and stiffness matrices, respectively, and $\hat{\mathbf{F}}_i$ is the elemental load vector which collects structural and aerodynamic contributions. Mass matrix is a function of the radial position, whereas gyroscopic and stiffness matrices and the load vector can also be functions of the azimuthal location (elemental expressions are reported in Section 2.4.1.1).
Matrices in equation (2.47) are obtained from structural linear terms only, whilst the force vector on the right-hand side of the energy equation of the $i-th$ element can be written as

$$\hat{\mathbf{F}}_i = (\mathbf{F}_0)_i + (\mathbf{F}_{nl})_i + (\mathbf{F}^{aer})_i \tag{2.48}$$

where $\mathbf{F}_0$ and $\mathbf{F}_{nl}$ represent constant and nonlinear contributions structural dynamics and $\mathbf{F}^{aer}$ denotes the

aerodynamic force vector. Throughout the thesis, both the aerodynamic and structural nonlinear loads are kept as fully nonlinear or linearized about a steady-state configuration ($\mathbf{q}_0$) to avoid numerical issues (see Section 4.3.1) during the time-integration of the aeroelastic system. For instance, making reference to the nonlinear structural force $\mathbf{F}_{nl}$, the first-order Taylor expansion about the reference state yields:

$$(\mathbf{F}_{nl})_i = (\mathbf{F}_{nl})_i \mid_{(\mathbf{q}_0)_i} + \frac{\partial (\mathbf{F}_{nl})_i}{\partial \mathbf{q}_i} \mathbf{q}_i \tag{2.49}$$

The first term on the right hand side of equation (2.49) is constant and therefore it is combined with $(\mathbf{F}_0)_i$. The linearized part of nonlinear force is derived analytically by differentiating the nonlinear force vector elements with respect to each term in the element displacement vector $\mathbf{q}_i$. This results in a displacement Jacobian matrix $(\mathbf{J_f})_{ij} = \frac{\partial \mathbf{f}_i(\mathbf{q})}{\partial \mathbf{q}_j}$.
Calculation of elemental matrices and load vector requires integration over the nondimensional local length ($0 \leq \xi \leq 1$); these integrals are evaluated numerically using a Gauss quadrature procedure

$$\int_0^1 f(\xi)\, d\xi = \sum_{j=1}^{N_G} f(s_j)\, w_j \tag{2.50}$$

where s_j is the local element position, w_j is the weighting factor of the $j-th$ quadrature point and N_G is the total number of quadrature points used in the interval $0 \leq \xi \leq 1$.
Finally, assembling elemental matrices and load vector over N spatial beam elements, yields the global nonlinear equations of motion in terms of nodal displacements. Assembly must assure compatibility between degrees of freedom at adjoining elemental nodes. The final expression for the total energy virtual variation is

$$\delta\Pi = \int_{\psi_1}^{\psi_2} \delta\mathbf{q}^T \left(\mathbf{M}\ddot{\mathbf{q}} + \mathbf{C}\dot{\mathbf{q}} + \mathbf{K}\mathbf{q} - \mathbf{F}\right) d\psi = 0 \tag{2.51}$$

where global nodal displacement vector, global matrices and global load vector are obtained with the summation over the N spatial beam elements of the elemental quantities.
Then, noting that the virtual displacements, $\delta\mathbf{q}$, are arbitrary, the following final form of blade equation of motion is derived

$$\mathbf{M}\ddot{\mathbf{q}} + \mathbf{C}\dot{\mathbf{q}} + \mathbf{K}\mathbf{q} = \mathbf{F} \tag{2.52}$$

Equation (2.52) is a set of nonlinear, ordinary differential equations (ODEs) for the global elastic DOFs, forced by inertial terms which are solved through a time-marching numerical scheme (details are provided in Appendix B).

2.4.1.1 Elemental expressions of structural matrices and load vector

The elemental mass, gyroscopic and stiffness matrices can be partitionated to indicated contributions from axial deflection, lag bending, flap bending and elastic torsion. Thus, the linear contribution of these matrices can be written as:

$$\mathbf{M}_i = \begin{bmatrix} \mathbf{M}_{uu} & \mathbf{M}_{uv} & \mathbf{M}_{uw} & \mathbf{M}_{u\hat{\phi}} \\ \mathbf{M}_{vu} & \mathbf{M}_{vv} & \mathbf{M}_{vw} & \mathbf{M}_{v\hat{\phi}} \\ \mathbf{M}_{wu} & \mathbf{M}_{wv} & \mathbf{M}_{ww} & \mathbf{M}_{w\hat{\phi}} \\ \mathbf{M}_{\hat{\phi}u} & \mathbf{M}_{\hat{\phi}v} & \mathbf{M}_{\hat{\phi}w} & \mathbf{M}_{\hat{\phi}\hat{\phi}} \end{bmatrix} \tag{2.53}$$

$$\mathbf{C}_i = \begin{bmatrix} \mathbf{C}_{uu} & \mathbf{C}_{uv} & \mathbf{C}_{uw} & \mathbf{C}_{u\hat{\phi}} \\ \mathbf{C}_{vu} & \mathbf{C}_{vv} & \mathbf{C}_{vw} & \mathbf{C}_{v\hat{\phi}} \\ \mathbf{C}_{wu} & \mathbf{C}_{wv} & \mathbf{C}_{ww} & \mathbf{C}_{w\hat{\phi}} \\ \mathbf{C}_{\hat{\phi}u} & \mathbf{C}_{\hat{\phi}v} & \mathbf{C}_{\hat{\phi}w} & \mathbf{C}_{\hat{\phi}\hat{\phi}} \end{bmatrix} \tag{2.54}$$

$$\mathbf{K}_i = \begin{bmatrix} \mathbf{K}_{uu} & \mathbf{K}_{uv} & \mathbf{K}_{uw} & \mathbf{K}_{u\hat{\phi}} \\ \mathbf{K}_{vu} & \mathbf{K}_{vv} & \mathbf{K}_{vw} & \mathbf{K}_{v\hat{\phi}} \\ \mathbf{K}_{wu} & \mathbf{K}_{wv} & \mathbf{K}_{ww} & \mathbf{K}_{w\hat{\phi}} \\ \mathbf{K}_{\hat{\phi}u} & \mathbf{K}_{\hat{\phi}v} & \mathbf{K}_{\hat{\phi}w} & \mathbf{K}_{\hat{\phi}\hat{\phi}} \end{bmatrix} \tag{2.55}$$

Note that the elemental structural mass and stiffness matrices are symmetric, whilst the gyroscopic one is antisymmetric. The linear mass matrix nondimensional terms are defined as:

$$\begin{gathered} \mathbf{M}_{uu} = \left(\frac{\Omega}{\Omega_0}\right)^2 el_i \int_0^1 \left(\frac{m}{m_0}\right) \mathbf{H}_u^T \mathbf{H}_u d\xi \\ \mathbf{M}_{vv} = \left(\frac{\Omega}{\Omega_0}\right)^2 el_i \int_0^1 \left(\frac{m}{m_0}\right) \mathbf{H}^T \mathbf{H} d\xi \\ \mathbf{M}_{ww} = \left(\frac{\Omega}{\Omega_0}\right)^2 el_i \int_0^1 \left(\frac{m}{m_0}\right) \mathbf{H}^T \mathbf{H} d\xi \\ \mathbf{M}_{\hat{\phi}\hat{\phi}} = \left(\frac{\Omega}{\Omega_0}\right)^2 el_i \int_0^1 \left(\frac{m}{m_0}\right) k_m^2 \mathbf{H}_{\hat{\phi}}^T \mathbf{H}_{\hat{\phi}} d\xi \\ \mathbf{M}_{v\hat{\phi}} = -\left(\frac{\Omega}{\Omega_0}\right)^2 el_i \int_0^1 \left(\frac{m}{m_0}\right) e_g \sin\theta_0 \mathbf{H}^T \mathbf{H}_{\hat{\phi}} d\xi \\ \mathbf{M}_{w\hat{\phi}} = \left(\frac{\Omega}{\Omega_0}\right)^2 el_i \int_0^1 \left(\frac{m}{m_0}\right) e_g \cos\theta_0 \mathbf{H}^T \mathbf{H}_{\hat{\phi}} d\xi \\ \mathbf{M}_{uv} = \mathbf{M}_{uw} = \mathbf{M}_{vw} = \mathbf{M}_{u\hat{\phi}} = \mathbf{0} \end{gathered} \tag{2.56}$$

The linear gyroscopic matrix nondimensional terms are defined as:

$$\begin{gathered} \mathbf{C}_{vv} = \left(\frac{\Omega}{\Omega_0}\right)^2 el_i \int_0^1 \left(\frac{m}{m_0}\right) \left(2e_g \cos\theta_0 \mathbf{H}'^T \mathbf{H} - 2e_g \cos\theta_0 \mathbf{H}^T \mathbf{H}'\right) d\xi \\ \mathbf{C}_{uv} = -\left(\frac{\Omega}{\Omega_0}\right)^2 el_i \int_0^1 2\left(\frac{m}{m_0}\right) \mathbf{H}_u^T \mathbf{H} d\xi \\ \mathbf{C}_{vw} = -\left(\frac{\Omega}{\Omega_0}\right)^2 el_i \int_0^1 \left(\frac{m}{m_0}\right) \left(2\beta_{pc} \mathbf{H}^T \mathbf{H} + 2e_g \sin\theta_0 \mathbf{H}^T \mathbf{H}'\right) d\xi \\ \mathbf{C}_{uu} = \mathbf{C}_{ww} = \mathbf{C}_{\hat{\phi}\hat{\phi}} = \mathbf{C}_{uw} = \mathbf{C}_{u\hat{\phi}} = \mathbf{C}_{v\hat{\phi}} = \mathbf{C}_{w\hat{\phi}} = \mathbf{0} \end{gathered} \tag{2.57}$$

The linear stiffness matrix nondimensional terms are defined as:

$$
\begin{aligned}
\mathbf{K}_{uu} &= el_i \int_0^1 \left(\tfrac{m}{m_0}\right) EA\, \mathbf{H}_u^{'T}\mathbf{H}_u^{'} d\xi \\
\mathbf{K}_{vv} &= el_i \int_0^1 \left[-\left(\tfrac{\Omega}{\Omega_0}\right)^2 \left(\tfrac{m}{m_0}\right) \mathbf{H}^T\mathbf{H} + \left(\tfrac{\Omega}{\Omega_0}\right)^2 F_A \mathbf{H}^{'T}\mathbf{H}^{'} + \left(EI_y \sin^2\theta_0 + EI_z \cos^2\theta_0\right) \mathbf{H}^{''T}\mathbf{H}^{''} \right] d\xi \\
\mathbf{K}_{ww} &= el_i \int_0^1 \left[\left(\tfrac{\Omega}{\Omega_0}\right)^2 F_A \mathbf{H}^{'T}\mathbf{H}^{'} + \left(EI_z \sin^2\theta_0 + EI_y \cos^2\theta_0\right) \mathbf{H}^{''T}\mathbf{H}^{''} \right] d\xi \\
\mathbf{K}_{\hat{\phi}\hat{\phi}} &= el_i \int_0^1 \left[\left(\tfrac{\Omega}{\Omega_0}\right)^2 \left(\tfrac{m}{m_0}\right) \left(k_{m2}^2 - k_{m1}^2\right) \cos 2\theta_0 \mathbf{H}_{\hat{\phi}}^T \mathbf{H}_{\hat{\phi}} + \left(GJ + EB_1\theta_0^{'2}\right) \mathbf{H}_{\hat{\phi}}^{'T}\mathbf{H}_{\hat{\phi}}^{'} + EC_1 \mathbf{H}_{\hat{\phi}}^{''T}\mathbf{H}_{\hat{\phi}}^{''} \right] d\xi \\
\mathbf{K}_{uv} &= -el_i \int_0^1 EAe_a \cos\theta_0 \mathbf{H}_u^{'T}\mathbf{H}^{''} d\xi \\
\mathbf{K}_{uw} &= -el_i \int_0^1 EAe_a \sin\theta_0 \mathbf{H}_u^{'T}\mathbf{H}^{''} d\xi \\
\mathbf{K}_{u\hat{\phi}} &= el_i \int_0^1 EAk_A^2 \theta_0^{'} \mathbf{H}_u^{'T}\mathbf{H}_{\hat{\phi}}^{'} d\xi \\
\mathbf{K}_{vw} &= el_i \int_0^1 \left(EI_z - EI_y\right) \sin\theta_0 \cos\theta_0 \mathbf{H}^{''T}\mathbf{H}^{''} d\xi \\
\mathbf{K}_{v\hat{\phi}} &= el_i \int_0^1 \left[\left(\tfrac{\Omega}{\Omega_0}\right)^2 \left(\tfrac{m}{m_0}\right) \left(\mathbf{H}^T\mathbf{H}_{\hat{\phi}} - x\mathbf{H}^{'T}\mathbf{H}_{\hat{\phi}}\right) e_g \sin\theta_0 - \left(EB_2\theta_0^{'} \cos\theta_0 \mathbf{H}^{''T}\mathbf{H}_{\hat{\phi}}^{'} + EC_2 \sin\theta_0 \mathbf{H}^{''T}\mathbf{H}_{\hat{\phi}}^{''} \right) \right] d\xi \\
\mathbf{K}_{w\hat{\phi}} &= el_i \int_0^1 \left[\left(\tfrac{\Omega}{\Omega_0}\right)^2 \left(\tfrac{m}{m_0}\right) \mathbf{H}^{'T}\mathbf{H}_{\hat{\phi}} x e_g \cos\theta_0 - EB_2\theta_0^{'} \sin\theta_0 \mathbf{H}^{''T}\mathbf{H}_{\hat{\phi}}^{'} + EC_2 \cos\theta_0 \mathbf{H}^{''T}\mathbf{H}_{\hat{\phi}}^{''} \right] d\xi
\end{aligned}
\tag{2.58}
$$

If the axial displacements are not allowed, the following equivalent term must be added in the matrix $\mathbf{K}_{\hat{\phi}\hat{\phi}}$ to those already presented, to take into account the axial force contribution to the stiffness of the blade:

$$
\mathbf{K}_{\hat{\phi}\hat{\phi}} = \left(\frac{\Omega}{\Omega_0}\right)^2 el_i \int_0^1 \left[\frac{1}{2} \left(\frac{m}{m_0}\right) k_m^2 \left(1 - x^2\right) \mathbf{H}_{\hat{\phi}}^{'T}\mathbf{H}_{\hat{\phi}}^{'} \right] d\xi \tag{2.59}
$$

As already seen for the structural matrices, the elemental force vector can be partitionated as follows:

$$
\mathbf{F}_i = \begin{bmatrix} \mathbf{F}_u \\ \mathbf{F}_v \\ \mathbf{F}_w \\ \mathbf{F}_{\hat{\phi}} \end{bmatrix} \tag{2.60}
$$

and can be written as

$$
\mathbf{F}_i = \mathbf{F}_{0i} + \mathbf{F}_{NLi} \tag{2.61}
$$

The constant force vector terms are given below as

$$
\mathbf{F}_{u0} = \left(\frac{\Omega}{\Omega_0}\right)^2 el_i \int_0^1 \left[\left(\frac{m}{m_0}\right) x \mathbf{H}_u^T \right] d\xi \tag{2.62}
$$

$$
\mathbf{F}_{v0} = \left(\frac{\Omega}{\Omega_0}\right)^2 el_i \int_0^1 \left[\left(\frac{m}{m_0}\right) \left(\left(e_g \cos\theta_0 + \ddot{\theta}_0 e_g \sin\theta_0\right) \mathbf{H}^T - e_g \cos\theta_0 x \mathbf{H}^{'T} \right) \right] d\xi \tag{2.63}
$$

$$
\mathbf{F}_{w0} = \left(\frac{\Omega}{\Omega_0}\right)^2 el_i \int_0^1 \left[\left(\frac{m}{m_0}\right) \left(-\left(\beta_{pc} x + \ddot{\theta}_0 e_g \cos\theta_0\right) \mathbf{H}^T - e_g \sin\theta_0 x \mathbf{H}^{'T} \right) \right] d\xi \tag{2.64}
$$

$$
\mathbf{F}_{\hat{\phi}0} = \left(\tfrac{\Omega}{\Omega_0}\right)^2 el_i \int_0^1 \left[\left(\tfrac{m}{m_0}\right) \left(-k_m^2 \ddot{\theta}_0 + \left(k_{m2}^2 - k_{m1}^2\right) \sin\theta_0 \cos\theta_0 - \beta_{pc} e_g \cos\theta_0 x \right) \mathbf{H}_{\hat{\phi}}^T \right] d\xi \tag{2.65}
$$

The nonlinear contributions to the force vector are

$$\mathbf{F}_{uNL} = -el_i \int_0^1 EA \left[e_a \left(v''\hat{\phi}\sin\theta_0 - w''\hat{\phi}\cos\theta_0 \right) + k_A^2 \frac{\hat{\phi}'^2}{2} + k_A^2 \theta_0' w' v'' \right] \mathbf{H}_u'^T d\xi \tag{2.66}$$

$$\begin{aligned} \mathbf{F}_{vNL} = & el_i \int_0^1 \left[\left((EI_z - EI_y)\, v''\hat{\phi}\sin 2\theta_0 - (EI_z - EI_y)\, w''\hat{\phi}\cos 2\theta_0 \right) \mathbf{H}''^T \right] d\xi + \\ & -el_i \int_0^1 \left[\left(EAe_a u_e' \hat{\phi}\sin\theta_0 + \left(GJ + EB_1\theta_0'^2 \right) \hat{\phi}' w' + EAk_A^2 \theta_0' w' u_e' \right) \mathbf{H}''^T \right] d\xi + \\ & -el_i \int_0^1 \left[2\left(\tfrac{\Omega}{\Omega_0} \right)^2 \left(-\left(\tfrac{m}{m_0} \right) \int_0^x \left(v'\dot{v}' + w'\dot{w}' \right) ds \mathbf{H}^T + v' \int_x^1 \left(\tfrac{m}{m_0} \right) \dot{v} ds \mathbf{H}'^T \right) \right] d\xi \end{aligned} \tag{2.67}$$

$$\begin{aligned} \mathbf{F}_{wNL} = & -el_i \int_0^1 \left[\left((EI_z - EI_y)\, v''\hat{\phi}\cos 2\theta_0 + (EI_z - EI_y)\, w''\hat{\phi}\sin 2\theta_0 - EAe_a u_e' \hat{\phi}\cos\theta_0 \right) \mathbf{H}''^T \right] d\xi + \\ & -el_i \int_0^1 \left[\left(\left(GJ + EB_1\theta_0'^2 \right) \hat{\phi}' v'' + EAk_A^2 \theta_0' v'' u_e' \right) \mathbf{H}'^T + 2\left(\tfrac{\Omega}{\Omega_0} \right)^2 w' \int_x^1 \left(\tfrac{m}{m_0} \right) \dot{v} ds \mathbf{H}'^T \right] d\xi \end{aligned} \tag{2.68}$$

$$\begin{aligned} \mathbf{F}_{\hat{\phi}NL} = & -el_i \int_0^1 \left[(EI_z - EI_y) \left(w''^2 \sin\theta_0 \cos\theta_0 + v''w'' \cos 2\theta_0 - v''^2 \sin\theta_0 \cos\theta_0 \right) \mathbf{H}_{\hat{\phi}}^T \right] d\xi + \\ & -el_i \int_0^1 \left(\left(GJ + EB_1\theta_0'^2 \right) w' v'' + EAk_A^2 \hat{\phi}' u_e' \right) \mathbf{H}_{\hat{\phi}}'^T d\xi \end{aligned} \tag{2.69}$$

2.4.2 Finite element discretization of blade aerodynamic loads

The procedure to express the virtual work done by aerodynamic loads acting on each rotor blade is similar to what has been discussed for the other energy terms in the Hamiltonian for the $b-th$ blade. In particular, all the rotor aerodynamic formulations that will be used in the present work yield a nonlinear dependence of sectional airloads on blade elastic deflections. Thus the determination of the generalized aerodynamic loads is strongly coupled with blade structural dynamics.

Starting from equation (2.41), the nondimensional variation of the virtual work done by the aerodynamic loads on the $b-th$ blade is

$$\delta W_b = \int_0^1 \delta \mathbf{u}^T \mathbf{L}_A d\xi \tag{2.70}$$

By applying FEM discretization, equation (2.70) is recast in the following form

$$\delta W_b = \sum_{i=1}^{N} \delta \mathbf{q}_i^T \int_0^{l_i/R} \mathbf{H}^T \mathbf{L}_{A_i} d\xi \tag{2.71}$$

where $\mathbf{L}_{A_i}$ is the vector of sectional loads evaluated within the $i-th$ finite element and it is a nonlinear function of global DOFs and of the azimuth.

Finally, making reference to N_G quadrature points on the $i-th$ finite element, denoting with ξ_k the radial position of each point (see Figure 2.5), equation (2.71) becomes

$$\delta W_b = \sum_{i=1}^{N} \delta \mathbf{q}_i^T \sum_{k=1}^{N_G} \left(\mathbf{H}^T \mathbf{L}_{A_i} \right)_k w_k \tag{2.72}$$

where $\left(\mathbf{H}^T \mathbf{L}_{A_i} \right)_k$ indicates aerodynamic force contribution evaluated at ξ_k and w_k is the weighting factor.

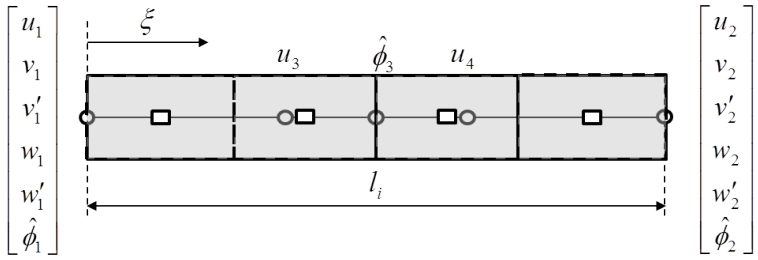

Figure 2.5: Finite element nodes (circles) and Gauss points (squares)

2.5 Hub loads calculation

Hub loads are given by the integration from the tip to the blade root, of both inertial and aerodynamic loads along the blade. In magnitude, they are equal to the champ reaction forces; in the rotating frame, they are given by the reaction forces and moments to those occurring outboard.

$$\begin{aligned} F_x &= \int_0^R L_u^{tot} dx \\ F_y &= \int_0^R L_v^{tot} dx \\ F_z &= \int_0^R L_w^{tot} dx \\ M_x &= \int_0^R \left(-L_v^{tot} w + L_w^{tot} v + M_u^{tot}\right) dx \\ M_y &= \int_0^R \left(L_u^{tot} w - L_w^{tot} \left(x + u\right) + M_v^{tot}\right) dx \\ M_z &= \int_0^R \left(-L_u^{tot} v + L_v^{tot} \left(x + u\right) + M_w^{tot}\right) dx \end{aligned} \tag{2.73}$$

where the total load come from the sum of aerodynamic and inertial contributions:

$$\begin{aligned} L_u^{tot} &= L_u + L_u^I \\ L_v^{tot} &= L_v + L_v^I \\ L_w^{tot} &= L_w + L_w^I \\ M_u^{tot} &= M_{\hat{\phi}} + M_u^I \\ M_v^{tot} &= v' M_{\hat{\phi}} + M_v^I \\ M_w^{tot} &= w' M_{\hat{\phi}} + M_w^I \end{aligned} \tag{2.74}$$

Aerodynamic loads derive from the formulations presented in Sections 3.1.1.1 and 3.1, whilst inertial contributions are here introduced. Both are written in the deformed configuration and projected in the undeformed blade of reference.

From Newton's second law, sectional inertial forces are

$$\mathbf{F}^I = -\iint \rho \vec{a} d\eta d\zeta \tag{2.75}$$

$$\mathbf{M}^I = -\iint \vec{s} \times \vec{a} d\eta d\zeta \tag{2.76}$$

where ρ is the blade density, $\vec{s}$ the moment arm with respect to the blade root and $\vec{a}$ the acceleration of a blade section written in the undeformed frame of reference, given by

$$\vec{a} = \ddot{\vec{r}} + \Omega \times (\Omega \times \vec{r}) + 2\left(\Omega \times \dot{\vec{r}}\right) \tag{2.77}$$

in which $\vec{r}$ is defined in Section 2.3.2. Inertial loads components in nondimensional form can be expressed as

$$L_u^I = -\left(\frac{m}{m_0}\right)\left[\ddot{u}_e - x - u_e - 2\dot{v} + \beta_{pc} w + e_g\left(v' - \ddot{v}'\right)\cos\theta_1 + e_g\left(w' + \beta_{pc} - \ddot{w}' + 2\dot{\theta}_1\right)\sin\theta_1\right] \tag{2.78}$$

$$\begin{gathered} L_v^I = -\left(\frac{m}{m_0}\right)\left[\ddot{v} - v + 2\dot{u}_e - 2\beta_{pc}\dot{w} - e_g\left(1 + 2\dot{v}'\right)\cos\theta_1 - 2v'\dot{v} - e_g\left(\ddot{\theta}_1 - \hat{\phi} + 2\dot{w}'\right)\sin\theta_1\right] + \\ -2v''\int_x^1\left(\frac{m}{m_0}\right)\dot{v}d\xi \end{gathered} \tag{2.79}$$

$$L_w^I = -\left(\frac{m}{m_0}\right)\left[\ddot{w} + \beta_{pc} x + 2\beta_{pc}\dot{v} + e_g\ddot{\theta}_1\cos\theta_1 - 2w'\dot{v}\right] - 2w''\int_x^1\left(\frac{m}{m_0}\right)\dot{v}d\xi \tag{2.80}$$

$$\begin{gathered} M_u^I = -\left(\frac{m}{m_0}\right)\left[k_m^2\ddot{\theta}_1 + \left(1 + 2\dot{v}' - 2\dot{\theta}_1\right)\left(k_{m2}^2 - k_{m1}^2\right)\cos\theta_1\sin\theta_1 + 2\dot{w}'\left(k_{m2}^2\sin^2\theta_1 + k_{m1}^2\cos^2\theta_1\right)\right] + \\ -\left(\frac{m}{m_0}\right)\left[\left(x\beta_{pc} + 2\dot{v} + \ddot{w}\right)e_g\cos\theta_1 + \left(v - \ddot{v}\right)e_g\sin\theta_1\right] \end{gathered} \tag{2.81}$$

$$\begin{gathered} M_v^I = -\left(\frac{m}{m_0}\right)\left[\left(v' + \beta_{pc} - \ddot{v}'\right)\left(k_{m2}^2 - k_{m1}^2\right)\cos\theta_1\sin\theta_1\right] + \\ -\left(\frac{m}{m_0}\right)\left[\left(w' - \ddot{w}' + 2\dot{\theta}_1\right)\left(k_{m2}^2\sin^2\theta_1 + k_{m1}^2\cos^2\theta_1\right) - \left(x + 2\dot{v}\right)e_g\sin\theta_1\right] \end{gathered} \tag{2.82}$$

$$\begin{gathered} M_w^I = -\left(\frac{m}{m_0}\right)\left[\left(\ddot{w}' - w' - 2\dot{\theta}_1 - \beta_{pc}\right)\left(k_{m2}^2 - k_{m1}^2\right)\cos\theta_1\sin\theta_1\right] + \\ -\left(\frac{m}{m_0}\right)\left[\left(\ddot{v} - v'\right)\left(k_{m2}^2\sin^2\theta_1 + k_{m1}^2\cos^2\theta_1\right) + \left(x + 2\dot{v}\right)e_g\cos\theta_1\right] \end{gathered} \tag{2.83}$$

Finally, rotor hub loads are obtained by summing load contributions from each individual blade. In the fixed frame, they are expressed as

$$F_X^H(\psi) = \sum_{m=1}^{N}\left(F_x^m cos\psi_m - F_y^m sin\psi_m - F_z^m cos\psi_m\beta_{pc}\right) \tag{2.84}$$

$$F_Y^H(\psi) = \sum_{m=1}^{N}\left(F_x^m sin\psi_m + F_y^m cos\psi_m - F_z^m sin\psi_m\beta_{pc}\right) \tag{2.85}$$

$$F_Z^H(\psi) = \sum_{m=1}^{N}\left(F_z^m + F_x^m\beta_{pc}\right) \tag{2.86}$$

$$M_X^H(\psi) = \sum_{m=1}^{N}\left(M_x^m cos\psi_m - M_y^m sin\psi_m - M_z^m cos\psi_m\beta_{pc}\right) \tag{2.87}$$

$$M_Y^H(\psi) = \sum_{m=1}^{N}\left(M_x^m sin\psi_m + M_y^m cos\psi_m - M_z^m sin\psi_m\beta_{pc}\right) \tag{2.88}$$

$$M_Z^H(\psi) = \sum_{m=1}^{N} (M_z^m + M_x^m \beta_{pc}) \tag{2.89}$$

where the index m refers to the $m-th$ blade.
Hub loads harmonic content is characterized only by those frequencies that are integral multiple of rotor frequency. These harmonics are generated by harmonics of rotating frame blade loads which are one higher and one lower than the rotor frequency. For example, for an N_b bladed rotor, the harmonics in the fixed frame hub loads are kN_b/rev, where k is an integer. These harmonics are generated by $kN_b \pm 1/rev$ in plane shear forces (F_x, F_y), kN_b/rev vertical shear force (F_z), $kN_b \pm 1/rev$ flap and torsion bending moments (M_x, M_y) and kN_b/rev chord bending moment (M_z) [18].

2.6 Aeroelastic formulation based on a spectral approach

A pre-existent numerical tool based on a modal approach [20] and developed at University Roma Tre, Dept. of Engineering is herein briefly introduced. Blade structural model is the same discussed in Section (2.3) and is based on the work of Hodges and Dowell ([14], [19]) whereas the Beddoes-Leishman model (discussed in detail in Section 3.1.3) is introduced to describe sectional aerodynamic loads. Blade motion equation is coupled to the unsteady aerodynamic model to yield the aeroelastic integro-partial differential equations to be integrated for rotor performance, response and stability analyses. This aeroelastic formulation has been successfully applied to helicopter and tiltrotor configurations [20, 21]. Space (blade spanwise) integration of the aeroelastic system is performed through the Galerkin approach (see Section 2.6.1). Steady-periodic rotor response to arbitrary wind conditions (like, for instance, axial wind, yawed wind and vertical shear layer conditions) is evaluated by a harmonic-balance technique [20, 22] at reduced computational costs. Concerning the aeroelastic stability analysis, an extensively technique applied in rotorcraft [23] and wind turbine aeroelasticity is based on the eigenanalysis of the aeroelastic system linearized about a steady-periodic equilibrium condition [24]; in order to define the eigenproblem to be solved a state-space representation of blade loads is required.

2.6.1 The Galerkin method

The equation governing the dynamic of the blade, can be written in a general form as

$$\rho \ddot{\mathbf{u}}(x,t) + \mathcal{L}\mathbf{u}(x,t) = \mathbf{f}(x,t) \tag{2.90}$$

where $\mathbf{u}$ is the vector which collects blade degrees of freedom, ρ the mass for unit length, $\mathcal{L}$ the differential aeroelastic operator and $\mathbf{f}$ the forcing vector. A technique for the solution of partial differential equations is provided by the Galerkin method which consists in expressing the solution through the following linear combination:

$$\mathbf{u}(x,t) = \sum_m \mathbf{u}_m(t)\, \mathbf{\Psi}_m(x) \tag{2.91}$$

denoting with $\mathbf{u}_m(t)$ the time dependent coefficients and with $\mathbf{\Psi}_m(x)$ suitable sets of linearly independent shape functions that satisfy the homogeneous boundary conditions. Then, substituting equation (2.91) into equation

(2.90) and supposing, for simplicity, a constant distribution of the mass for unit length in the domain yields:

$$\rho \sum_m \ddot{\mathbf{u}}_m(t)\,\mathbf{\Psi}_m(x) + \sum_m \mathcal{L}\mathbf{u}_m(t)\,\mathbf{\Psi}_m(x) = \mathbf{f}(x,t) \tag{2.92}$$

and projecting equations on the shape functions one obtains

$$\rho \sum_m \ddot{\mathbf{u}}_m(t)\,\mathbf{m}_{mn} + \sum_m \mathbf{u}_m(t)\,\mathbf{k}_{mn} = \mathbf{f}_n \tag{2.93}$$

where

$$\begin{aligned} \mathbf{m}_{mn} &= \textstyle\int_D \mathbf{\Psi}_m(x)\,\mathbf{\Psi}_n(x)\,dD \\ \mathbf{k}_{mn} &= \textstyle\int_D \mathbf{\Psi}_m(x)\,\mathcal{L}\mathbf{\Psi}_n(x)\,dD \\ \mathbf{f}_n &= \textstyle\int_D \mathbf{f}\mathbf{\Psi}_n(x)\,dD \end{aligned} \tag{2.94}$$

The final expression in a matricial form is

$$\mathbf{M}\ddot{\mathbf{u}} + \mathbf{K}\mathbf{u} = \mathbf{f} \tag{2.95}$$

where the unknowns of the problem are the time dependent coefficients. Following this method, the original partial differential problem has been transformed into a system of ordinary differential equations.

Chapter 3

Rotor aerodynamic modelling

Application of Hamilton's principle analyzed in the previous chapter requires the definition of the external virtual work on the system which is a function of the external forces, i.e. the aerodynamic loads acting on the blade. Distributed sectional loads are provided by aerodynamic formulations based on the definition of the angle of attack at a certain point ($\eta = \eta_r$ and $\xi = 0$) along the chord of each cross section. Then, sectional theories describing the airfoil aerodynamic behavior are presented. Unsteady, incompressible aerodynamic loads generated on translating airfoils undergoing plunge motion, h, and pitch motion, α are predicted by the Theodorsen theory [25]. The extension of this theory by Greenberg [19] to deal with pulsating free stream is presented. Finally, the Beddoes-Leishman formulation to simulate flow separation effects due to dynamic stall is presented. The influence of three-dimensional effects due to wake induced inflow and their inclusion in the present model will be discussed in Section 3.2, where the simple momentum theory approach, the Drees model, and a more advanced description obtained through an unsteady, three dimensional, free wake panel method are presented; then, four coupling strategies between sectional aerodynamic models and the 3D BEM wake inflow are proposed. Deep stall regimes are analyzed through the Viterna-Corrigan approach by extension of airfoil static coefficients to high angles of attack based on flat plate theory, whilst Snel model is used to take into account centrifugal effects. The last section deals with the definition of the airfoil velocity components at a certain point along the chord of each cross section.

3.1 Unsteady aerodynamic models

Three different sectional unsteady aerodynamic models are presented in this section. The fundamental assumption of these models is that each blade section can be modeled, from an aerodynamics standpoint, as an independent airfoil moving in an unsteady potential flow. The first aerodynamic formulation is based on the Theodorsen theory [25] to predict unsteady, incompressible aerodynamic loads generated on translating airfoils undergoing plunge motion, h, and pitch motion, ϵ; a quasi-steady approximation of this theory is also presented. Then the extension of this theory by Greenberg [19] to deal with a pulsating free stream is introduced. Finally, the Beddoes-Leishman formulation to simulate flow separation effects and the inclusion of three-dimensional effects due to wake induced inflow, are presented.

3.1.1 Theodorsen Theory

The Theodorsen theory describes unsteady aerodynamic forces and moment acting on a thin airfoil under the assumption of incompressible and inviscid flow. The airfoil has two degrees of freedom: a vertical translation h (plunge) positive downward and a rotation ϵ (pitch) positive nose up, about an axis located at a distance $a_h b$ from the mid-chord point, a_h being positive towards the trailing edge. The flow is assumed to be two-dimensional, h and ϵ are considered infinitesimal, and the free stream velocity V is constant (see Figure 3.1).

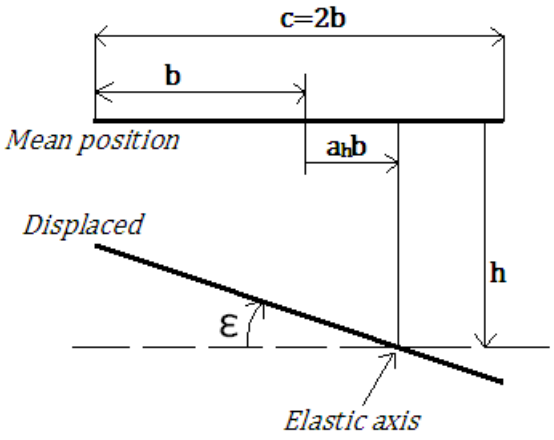

Figure 3.1: Airfoil pitching and plunge motion

Sectional lift is modeled as the sum of a circulatory and a noncirculatory contribution. The first one arises from circulation and depends on the normal velocity component of airfoil at the 3/4 chord point ($v_n^{3/4}$). Shed vorticity is modeled through the Theodorsen Lift Deficiency Function $C(k)$ and the expression of L_c is

$$L_c = 2\pi\rho b V C(k) v_n^{3/4} \tag{3.1}$$

where ρ is the air density and $b = c/2$ being c the airfoil chord.
The downwash at the three quarter chord point is due to a chordwise uniform contribution corresponding to a pitching angle ϵ and a vertical translation $\dot{h}$, and a nonuniform term due to the angular velocity $\dot{\epsilon}$:

$$v_n^{3/4} = \dot{h} + \epsilon V + b\dot{\epsilon}\left(\frac{1}{2} - a_h\right) \tag{3.2}$$

The Theodorsen Lift Deficiency Function $C(k)$ is a transcendental function of the reduced frequency $k = \omega b/V$, being ω the pitching frequency. In order to derive a finite-state formulation, a second-degree Padè approximation based on the Wagner function is assumed [26]

$$C(k) = 0.5\frac{(ik + 0.135)(ik + 0.651)}{(ik + 0.0965)(ik + 0.4555)} \tag{3.3}$$

where i indicates the imaginary unit.

Non circulatory lift (also indicated as apparent mass force) depends on airfoil acceleration at mid-chord point (L_{nc1}) and at the three-quarter point (L_{nc2}) and can be expressed as following

$$L_{nc} = L_{nc1} + L_{nc2} = \rho\pi b^2 \left(\ddot{h} - a_h b\ddot{\epsilon}\right) + \rho\pi b^2 \left(V\dot{\epsilon}\right) \tag{3.4}$$

Finally, the total lift per unit span is

$$L = L_c + L_{nc1} + L_{nc2} \tag{3.5}$$

whilst the expression of the total moment per unit span about the elastic axis is

$$M = \left(\frac{1}{2} + a_h\right) bL_c + a_h bL_{nc1} - \left(\frac{1}{2} - a_h\right) bL_{nc2} + M_a \tag{3.6}$$

where $M_a = -\frac{\rho\pi b^4}{8}\ddot{\epsilon}$ is a nose-down moment. An aerodynamic profile drag force for unit length, acting parallel to the resultant blade velocity, is included based on a constant profile drag coefficient c_{D0}

$$D = \frac{\rho c_{L\alpha} c}{2} \frac{c_{D0}}{c_{L\alpha}} \left(U_T^2 + U_P^2\right) \tag{3.7}$$

Normal (T) and parallel (S) to the airfoil chord line force components (see Figure 3.2) are obtained as follows

$$\begin{aligned} T &= L_C \cos\alpha + L_{NC} + D\sin\alpha \\ S &= L_C \sin\alpha - D\cos\alpha \end{aligned} \tag{3.8}$$

Finally, loads expression in the undeformed frame of reference required in equation (2.41) are obtained as

$$\begin{Bmatrix} \left(L_u^A\right)_C \\ \left(L_v^A\right)_C \\ \left(L_w^A\right)_C \end{Bmatrix} = \mathbf{T}_{DU}^T \begin{Bmatrix} 0 \\ S \\ T \end{Bmatrix} \tag{3.9}$$

$$M_{\hat{\phi}}^A = M \tag{3.10}$$

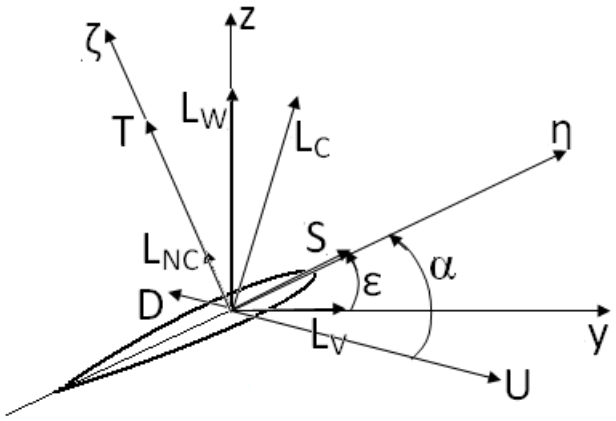

Figure 3.2: Directions of aerodynamic loading

3.1.1.1 Quasi-steady aerodynamics

This section presents a quasi-steady approximation sectional aerodynamic model in which circulatory terms are assumed to be steady whilst the non circulatory ones are retained as in the Theodorsen formulation. The quasi-steady approximation is judged to be adequate for low frequency analyses, thus $C(k)$ can be set equal to 1. This type of quasi-steady aerodynamics is herein introduced on the basis of Ref.[27] and will be used to validate the proposed aeroelastic model with available numerical data.
Circulatory nondimensional blade airloads in the deformed frame of reference can be directly written as:

$$\begin{aligned} \left(\bar{L}\right)_C &= \tfrac{1}{m_0\Omega^2 R}\left(\tfrac{1}{2}\rho V^2 c C_l\right) \\ \left(\bar{D}\right)_C &= \tfrac{1}{m_0\Omega^2 R}\left(\tfrac{1}{2}\rho V^2 c C_d\right) \\ \left(\bar{M}\right)_C &= \tfrac{1}{m_0\Omega^2 R^2}\left(\tfrac{1}{2}\rho V^2 c^2 C_m\right) \end{aligned} \tag{3.11}$$

where ρ is the air density, V is the total incident velocity, c is the section chord and $C_l,\ C_d,\ C_m$ are the section lift, drag, and pitching moment coefficients, respectively. The aerodynamic coefficients are expressed as

$$\begin{aligned} C_l &= c_0 + c_1\alpha \\ C_d &= d_0 + d_1|\alpha| + d_2\alpha^2 \\ C_m &= f_0 + f_1\alpha \end{aligned} \tag{3.12}$$

where α is the angle of attack at the three-quarter chord point, c_0 the zero angle lift coefficient, c_1 the lift curve slope, d_0 the viscous drag coefficient, f_0 the zero angle pitching moment coefficient about the aerodynamic center, and $d_1,\ d_2,\ f_1$ the additional drag and moment coefficients due to the camber of the airfoil. These relations are valid for incompressible attached flow conditions. Compressibility effects are accounted for by modifying the lift curve slope as

$$c_1 = \frac{c_{1_{M=0}}}{\beta} = \frac{c_{1_{M=0}}}{\sqrt{1-M^2}} \tag{3.13}$$

where $c_{1_{M=0}}$ represents the lift curve slope for incompressible flows, β is the Prandtl-Glauert factor and M is the Mach number [28].
External loads along the deformed axes that appear in the principle of virtual work are normal, chord, axial forces and moment about the elastic axis (see Figure 3.3):

$$\begin{aligned} \left(\bar{L}^A_w\right)_C &= \left(\bar{L}\right)_C\cos\alpha + \left(\bar{D}\right)_C\sin\alpha \\ \left(\bar{L}^A_v\right)_C &= \left(\bar{L}\right)_C\sin\alpha - \left(\bar{D}\right)_C\cos\alpha \\ \left(\bar{L}^A_u\right)_C &= -\left(\bar{D}\right)_C\sin\Lambda \\ \left(\bar{M}^A_{\hat{\phi}}\right)_C &= \left(\bar{M}_{ac}\right)_C - e_d\left(\bar{L}_w\right)_C \end{aligned} \tag{3.14}$$

where Λ is the axial skew angle due to the radial velocity component acting on the blade, and e_d is the chordwise offset between the elastic axis and the aerodynamic center, positive towards the trailing edge. In order to be coupled to blade equation of motion (see equation (2.52)) the forces are nondimensionalized by dividing by $m_0\Omega^2 R$, whilst moment is divided by $m_0\Omega^2 R^2$.

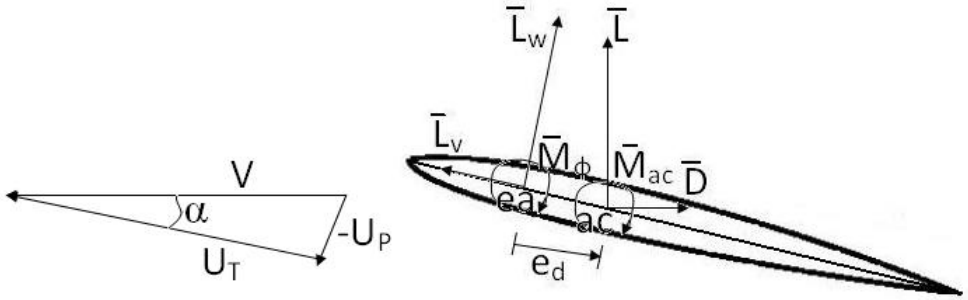

Figure 3.3: Circulatory aerodynamic loads in the deformed frame of reference

Substituting expressions (3.12) into (3.11) and into (3.14), and using the approximations

$$\begin{array}{c} \sin\alpha \approx \alpha \\ \cos\alpha \approx 1 \\ V \approx U_T \\ \alpha \approx -\frac{U_P}{U_T} \\ \sin\Lambda \approx \frac{U_R}{U_T} \end{array} \tag{3.15}$$

yields the following expressions for the nondimensional forces and moments in the deformed frame of reference:

$$\begin{array}{c} \left(\bar{L}_w^A\right)_C = \frac{\gamma}{6c_{L\alpha}}\left[c_0 U_T^2 - (c_1+d_0)\,U_T U_P + d_1 U_P^2\right] \\ \left(\bar{L}_v^A\right)_C = \frac{\gamma}{6c_{L\alpha}}\left[-d_0 U_T^2 - (c_0-d_1)\,U_T U_P + (c_1-d_2)\,U_P^2\right] \\ \left(\bar{L}_u\right)_C = \frac{\gamma}{6c_{L\alpha}}\left[-d_0 U_T U_R\right] \\ \left(\bar{M}_{\hat{\phi}}^A\right)_C = \frac{\gamma}{6c_{L\alpha}}\left[\frac{c}{R}\left(f_0\left(U_T^2+U_P^2\right) - f_1 U_T U_P\right)\right] - e_d\left(\bar{L}_w\right)_C \end{array} \tag{3.16}$$

Circulatory aerodynamic forces in the undeformed frame are obtained using the transformation matrix $\mathbf{T}_{DU}$ in equation (2.8)

$$\left\{\begin{array}{c} \left(L_u^A\right)_C \\ \left(L_v^A\right)_C \\ \left(L_w^A\right)_C \end{array}\right\} = \mathbf{T}_{DU}^T \left\{\begin{array}{c} \left(\bar{L}_u^A\right)_C \\ \left(\bar{L}_v^A\right)_C \\ \left(\bar{L}_w^A\right)_C \end{array}\right\} \tag{3.17}$$

whilst the following approximation for the moment about the elastic axis is used

$$\left(M_{\hat{\phi}}^A\right)_C \approx \left(\bar{M}_{\hat{\phi}}^A\right)_C \tag{3.18}$$

For an airfoil section undergoing plunge motion h and pitch motion θ_1 (it is a cinematic angle), non circulatory lift and pitching moment are given by

$$\begin{array}{c} \left(L_w^A\right)_{NC} = \frac{1}{m_0\Omega^2 R}\left[\rho\pi b^2\left(\ddot{h} - a_h b\ddot{\theta}_1\right) + \rho\pi b^2 U\dot{\theta}_1\right] = \frac{1}{m_0\Omega^2 R}\left[L_{nc1} + L_{nc2}\right] \\ \left(M_\phi^A\right)_{NC} = \frac{1}{m_0\Omega^2 R^2}\left[a_h b L_{nc1} - \left(\frac{1}{2} - a_h\right) b L_{nc2} - \frac{\rho\pi b^4}{8}\ddot{\theta}_1\right] \end{array} \tag{3.19}$$

where

$$\begin{gathered} U = \Omega R\left(x + \mu \sin\psi\right) \\ a_h b = -\left(e_d + \tfrac{c}{4}\right) \\ \ddot{h} = -\ddot{w} \\ \ddot{\theta}_1 = \ddot{\theta}_0 + \ddot{\hat{\phi}} \\ \dot{\theta}_1 = \dot{\theta}_0 + \dot{\hat{\phi}} \\ b = \tfrac{c}{2} \end{gathered} \tag{3.20}$$

Note that U is the free stream tangential velocity (see Figure 3.4), $a_h b$ is the distance from mid-chord to the elastic axis (positive aft), $\ddot{h}$ is the plunge acceleration (positive down), $\ddot{\theta}_1$ is the pitch acceleration (positive nose up), $\dot{\theta}_1$ is the pitch angular velocity and b is the airfoil semi-chord. L_{nc1} component of the non circulatory lift acts at the mid-chord and L_{nc2} component acts at the third-quarter chord point. Also note that non circulatory airloads are assumed to act directly on the blade undeformed section. Substituting (3.20) in equations (3.19), yield the following nondimensional loads

$$\begin{gathered} \left(L_w^A\right)_{NC} = \tfrac{\gamma\pi\frac{c}{R}}{12c_{L\alpha}}\left(-\tfrac{\ddot{w}}{R} + \tfrac{\frac{c}{4}+e_d}{R}\ddot{\theta}_1 + \left(x + \mu\sin\psi\right)\dot{\theta}_1\right) \\ \left(M_{\hat{\phi}}^A\right)_{NC} = \tfrac{\gamma\pi\frac{c}{R}}{12c_{L\alpha}}\left(\tfrac{\frac{c}{4}+e_d}{R}\tfrac{\ddot{w}}{R} - \left(\tfrac{\frac{c}{4}+e_d}{R}\right)^2\ddot{\theta}_1 - \tfrac{\frac{c}{2}+e_d}{R}\left(x + \mu\sin\psi\right)\dot{\theta}_1 - \tfrac{c^2}{R^2}\tfrac{1}{32}\ddot{\theta}_1\right) \end{gathered} \tag{3.21}$$

Non circulatory airloads are added to the circulatory ones to obtain the total aerodynamic loads acting on the blade section.

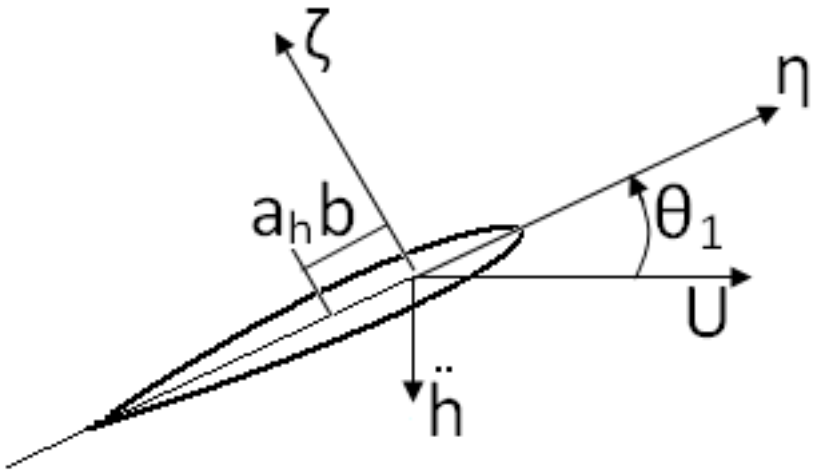

Figure 3.4: Airfoil definitions used in the quasi-steady aerodynamic formulation

3.1.2 Greenberg theory

A two-dimensional airfoil is assumed to be pivoted about an axis which may be distinct, in general, from the aerodynamic center axis. The airfoil is pitched at an angle $\epsilon(t)$ with respect to the free stream flowing at pulsating velocity $V(t)$. The airfoil is vertically displaced with velocity $\dot{h}(t)$ positive downward as shown in Figure 3.5.

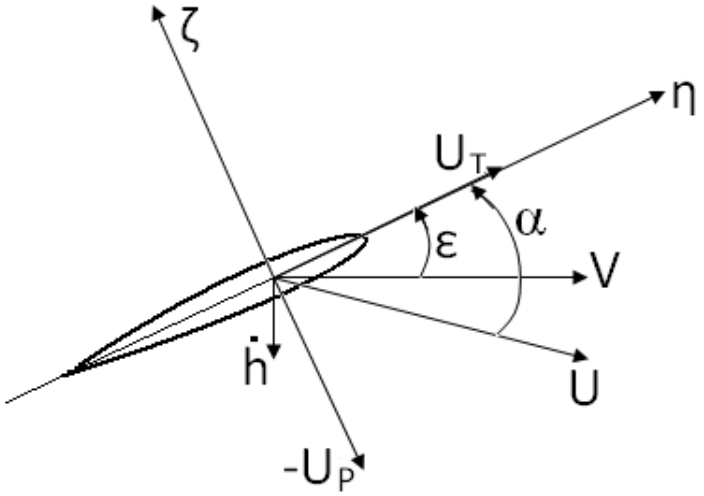

Figure 3.5: Rotor blade airfoil section in general unsteady motion

The relations for lift and pitching moment for unit length may be expressed in terms of the circulatory and non circulatory components

$$\begin{aligned} L &= L_C + L_{NC} \\ M &= M_C + M_{NC} \end{aligned} \tag{3.22}$$

With the airfoil pivot axis (which, in the present work is assumed coincident with the rotor blade elastic axis) at the airfoil quarter chord (the airfoil aerodynamic center) these components are:

$$\begin{aligned} L_{NC} &= \tfrac{\rho c_{L_\alpha} c}{2} \tfrac{c}{4} \left(\ddot{h} + V\dot{\epsilon} + \dot{V}\epsilon + \tfrac{c}{4}\ddot{\epsilon} \right) \\ L_C &= \tfrac{\rho c_{L_\alpha} c}{2} V \left(\dot{h} + V\epsilon + \tfrac{c}{2}\dot{\epsilon} \right) C(k) \\ M_{NC} &= -\tfrac{c}{4} L_{NC} - \tfrac{\rho c_{L_\alpha} c}{2} \left(\tfrac{c}{4} \right)^3 \tfrac{\ddot{\epsilon}}{2} \\ M_C &= -\tfrac{\rho c_{L_\alpha} c}{2} \left(\tfrac{c}{4} \right)^2 V\dot{\epsilon} \end{aligned} \tag{3.23}$$

where $C(k)$ is the Theodorsen Lift Deficiency function already discussed in Section 3.1.1; a quasi-steady approximation of this model is obtained by setting $C(k) = 1$.
It should be noted that ϵ is the angular position of the airfoil with respect to space; $\dot{\epsilon}$ and $\ddot{\epsilon}$ are the angular velocity and the angular acceleration of the airfoil. The instantaneous angle of attack of the airfoil $\alpha = -tan^{-1}(U_p/U_T)$ is the angle between the airfoil chord line and the resultant fluid velocity U of the airfoil. The airfoil velocity components in the section principal axis system (η, ζ) are shown in Figure 3.5. Section airloads must then be expressed in terms of U_P and U_T. Assuming that the angles ϵ and α are small yields

$$\begin{aligned} U_P &\cong -\dot{h} - V\epsilon \\ U &= \sqrt{U_T^2 + U_P^2} \cong V \end{aligned} \tag{3.24}$$

Substitution of equations (3.24) into (3.23) yields

$$\begin{aligned} L_{NC} &= \frac{\rho c_{L\alpha} c}{2} \frac{c}{4} \left(-\dot{U}_P + \frac{c}{4} \ddot{\epsilon} \right) \\ L_C &= \frac{\rho c_{L\alpha} c}{2} U \left(-U_P + \frac{c}{2} \dot{\epsilon} \right) C(k) \\ M_{NC} &= -\frac{\rho c_{L\alpha} c}{2} \left(\frac{c}{4} \right)^2 \left(-\dot{U}_P + \frac{3c}{8} \ddot{\epsilon} \right) \\ M_C &= -\frac{\rho c_{L\alpha} c}{2} \left(\frac{c}{4} \right)^2 U \dot{\epsilon} \end{aligned} \tag{3.25}$$

The non circulatory lift is taken to act normal to the chord line, and the circulatory lift is taken to act normal to the resultant blade velocity V. An aerodynamic sectional drag force is also considered, see equation (3.7). The force components and positive directions are shown in Figure 3.6. The total aerodynamic force components T, normal to the airfoil chord line, and S, parallel to the airfoil chord line, are therefore

$$\begin{aligned} T &= L_C \cos\alpha + L_{NC} + D \sin\alpha \\ S &= L_C \sin\alpha - D \cos\alpha \end{aligned} \tag{3.26}$$

From Figure 3.5,

$$\begin{aligned} \cos\alpha &= \frac{U_T}{U} = \frac{U_T}{\sqrt{U_T^2 + U_P^2}} \\ \sin\alpha &= \frac{-U_P}{U} = \frac{-U_P}{\sqrt{U_T^2 + U_P^2}} \end{aligned} \tag{3.27}$$

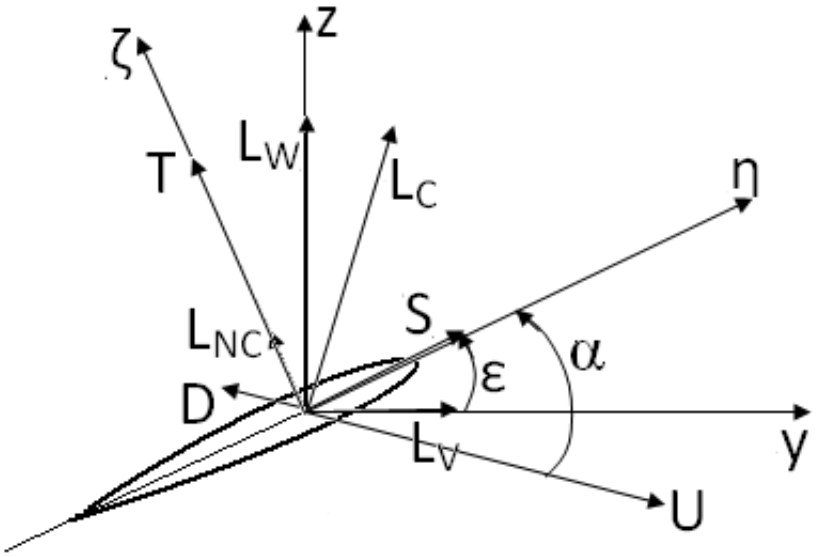

Figure 3.6: Directions of aerodynamic loading

Substitution of equations (3.25), (3.7) and (3.27) into equations (3.26), with $c_{D0}/c_{L\alpha}$ neglected with respect to unity, yields

$$\begin{aligned} T &= \frac{\rho c_{L\alpha} c}{2} \left[-U_P U_T C(k) + \frac{c}{2} U_T \dot{\epsilon} C(k) - \frac{c}{4} \dot{U}_P + \left(\frac{c}{4} \right)^2 \ddot{\epsilon} \right] \\ S &= \frac{\rho c_{L\alpha} c}{2} \left[U_P^2 C(k) - \frac{c}{2} U_P \dot{\epsilon} C(k) - \frac{c_{D0}}{c_{L\alpha}} U_T^2 \right] \end{aligned} \tag{3.28}$$

The total pitching moment, in which U has been approximated by U_T, is given by

$$M_\phi = M_{NC} + M_C = -\frac{\rho c_{L\alpha} c}{2}\left(\frac{c}{4}\right)^2\left(-\dot{U}_P + \frac{3c}{8}\ddot{\epsilon} + U_T\dot{\epsilon}\right) \tag{3.29}$$

Finally, loads expression in the undeformed frame of reference required in equation (2.41) are obtained as

$$\left\{\begin{array}{c}\left(L_u^A\right)_C\\ \left(L_v^A\right)_C\\ \left(L_w^A\right)_C\end{array}\right\} = \mathbf{T}_{DU}^T\left\{\begin{array}{c}0\\ S\\ T\end{array}\right\} \tag{3.30}$$

$$M_{\hat{\phi}}^A = M_\phi \tag{3.31}$$

3.1.2.1 Hover condition

In hover condition, the expressions of blade velocity components and angular velocity in terms of the blade bending and torsion deflections (see equations (3.87), (3.88) and (3.89)) are

$$\begin{array}{c} U_P = -\Omega x\left(\theta + \phi + \int_0^x v'w''dx\right) - (\theta+\phi)\,\dot{v} + v_i + \dot{w} + \Omega v\left(\beta_{pc} + w'\right)\\ U_T = \Omega x + \dot{v}\\ \dot{\epsilon} = \dot{\phi} + \Omega\left(\beta_{pc} + w'\right)\end{array} \tag{3.32}$$

in which all terms of $O\left(\epsilon^2\right)$ are neglected with respect to unity, and for $\theta = O(\epsilon)$ the approximation $\sin\theta \cong \theta$ and $\cos\theta \cong 1$ has been used. The induced inflow v_i is taken to be steady and uniform along the blade radius equal to the value of nonuniform inflow given by blade element momentum theory at the radial station $x = 0.75R$ (see Section 3.2.1).

The matrix transformation $\mathbf{T}_{DU}$ in equation (2.8) may be used to project blade forces S and T in the deformed frame of reference, into L_v and L_w parallel to the y and z axes of the undeformed blade coordinate system. For small deformations this transformation yields:

$$\begin{array}{c} L_v = S - T(\theta+\phi)\\ L_w = T + S(\theta+\phi)\end{array} \tag{3.33}$$

Finally, substituting equations (3.32) into equations (3.28), then in (3.33) yield the following expressions for forces and moment in the undeformed frame of reference:

$$\begin{array}{c} L_v = \frac{\rho c_{L\alpha} c}{2}\{v_i^2 - \Omega^2 x^2\frac{c_{D0}}{c_{L\alpha}} - \Omega x v_i(\theta+\phi) - \left[2\Omega x\frac{c_{D0}}{c_{L\alpha}} + v_i(\theta+\phi)\right]\dot{v} + \left[2v_i - \Omega x(\theta+\phi)\right]\dot{w}\}\\ L_w = \frac{\rho c_{L\alpha} c}{2}\{-\Omega x v_i + \Omega^2 x^2\left(\theta+\phi+\int_0^x v'w''dx\right) - \Omega^2 x v\left(\beta_{pc}+w'\right) + \Omega^2\frac{xc}{2}\left(\beta_{pc}+w'\right) + ...\\ ... + \left[2\Omega x(\theta+\phi) - v_i\right]\dot{v} - \Omega x\dot{w} + \frac{3c}{4}\Omega x\dot{\phi} - \frac{c}{4}\ddot{w}\}\\ M_\phi = -\frac{\rho c_{L\alpha} c}{2}\left(\frac{c^2}{8}\Omega x\dot{\phi}\right)\end{array} \tag{3.34}$$

note that they are written assuming the quasi-steady approximation, thus $C(k) = 1$.

Nonlinear contributions and all $O\left(\epsilon^3\right)$ terms, except those that contribute to lead-lag or torsion damping, are neglected (including $\ddot{\epsilon}$ terms).

3.1.3 Beddoes-Leishman theory

Dynamic stall phenomenon is characterized by a delay in the onset of flow separation to a higher angle of attack than would occur under static conditions. This delay represents an advantage for performance of the airfoil because lift generated can be higher than the maximum attainable under static conditions. However, when dynamic separation eventually occurs, a leading edge vortex is released over the airfoil and is convected downstream. During the short time in which the vortex travels over the airfoil upper surface, it generates extra lift forces. Once the vortex has been convected beyond the trailing edge, the absence of contribution from the vortex results in large nose-down pitching moments on the airfoil which can result very dangerous for the stability of the wind turbine. Figure 3.7 shows airfoil aerodynamic loadings during a dynamic stall cycle and compares dynamic behavior with the static one.

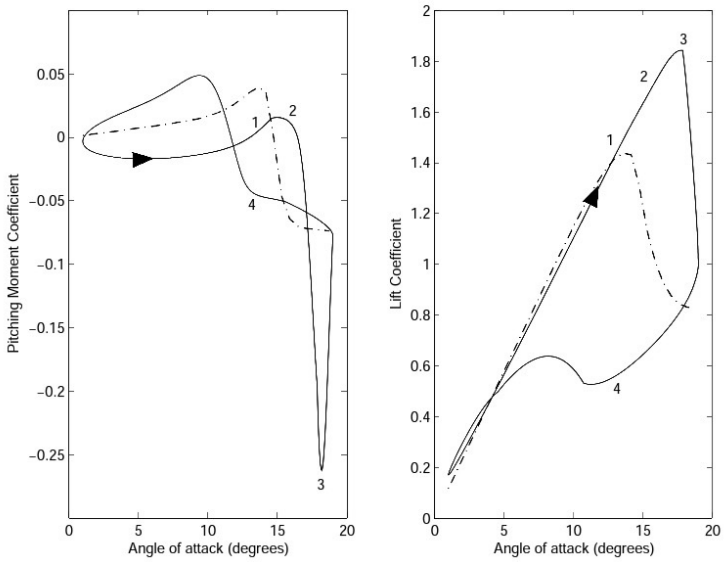

Figure 3.7: Pitching moment and lift coefficients of an airfoil in pure pitching moment

The various stages of the dynamic stall process can be briefly summarized in four main stages (figures 3.7 and 3.8). Stage 1 coincides with the static stall, then, due to the delay in the onset of flow separation, airfoil exceeds static stall angle but flow reversals begin to take place in the boundary layer. Stage 2 is characterized by flow separation at the leading edge and by the formation of a vortex disturbance that provides additional lift on the airfoil as long as it is convected on the upper surface, whilst the pitching moment stall; then, significant increase in nose-down pitching moment generated by the aft moving of the center of pressure is visible. Stage 3 coincides with the lift stall and the maximum value of the nose-down pitching moment; vortex reaches airfoil trailing edge and flow progresses to a state of full separation which corresponds to a sudden loss of lift. Finally, full flow reattachment may not be obtained until the airfoil is well below its normal static stall angle and represents Stage 4 of this dynamic process.

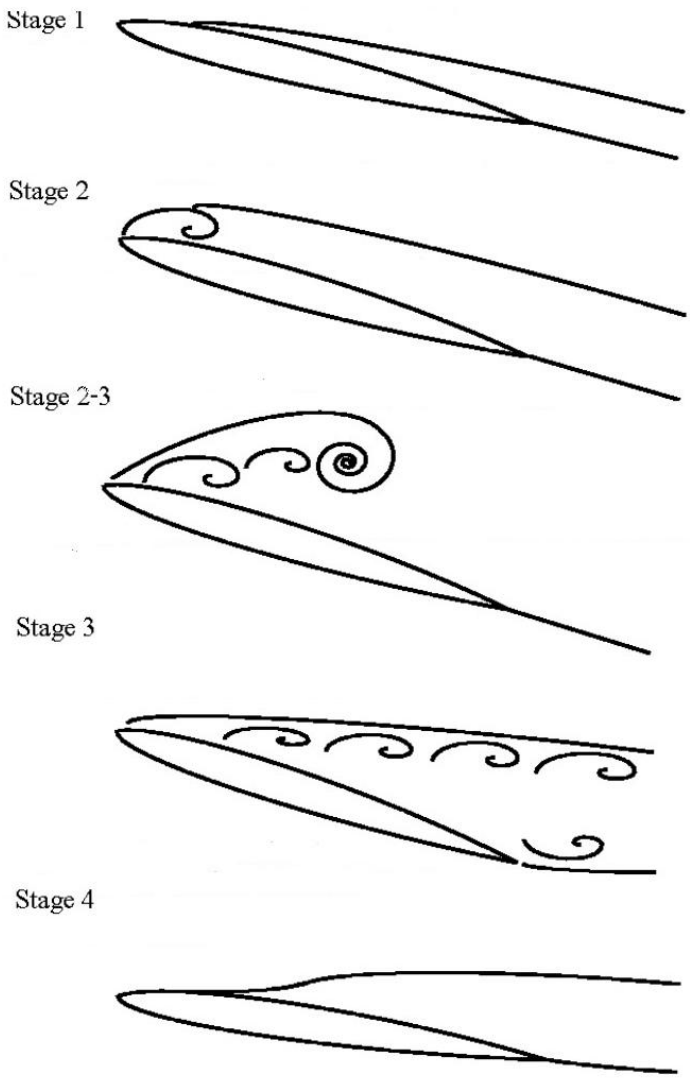

Figure 3.8: Flow morphology during the dynamic stall process on an oscillating 2-D airfoil

State-space formulation proposed by Beddoes and Leishman (B-L model in the following) ([29], [30], [31], [32]) is herein presented. Combined with the airfoil motion, a set of aerodynamic states, $\mathbf{x}$, governed by ordinary differential equations (ODEs) describes, at an engineering level of approximation, airloads arising in two-dimensional unsteady aerodynamics. This model predicts aerodynamic loads generated on translating airfoils undergoing plunge motion, h, and pitch motion, α, in the presence of dynamic stall, leading and trailing edge separation conditions. Specifically, airfoil forces and pitching moment coefficients (see Figure 3.9) will be obtained in terms of a set of differential forms, $\mathbf{g}$, as formally indicated by

$$\left\{ \begin{array}{c} C_N \\ C_M \\ C_C \end{array} \right\} = \mathbf{g}\left(\mathbf{x}, \alpha, q, h\right) \tag{3.35}$$

with aerodynamic states derived from a set of forced first order ODEs

$$\mathbf{x}' = \mathbf{f}(\mathbf{x}, \alpha, q, h) \tag{3.36}$$

where $\mathbf{x}'$ represents the derivative with respect to nondimensional time $s = t\frac{2V}{c}$ and $q = \dot{\alpha}\frac{2V}{c}$ is the pitch rate. Different formulations to simulate incompressible and compressible attached flow conditions are presented in the following.

In a incompressible flow, a time domain unsteady aerodynamic formulation has been developed by Wagner [33] who obtained the solution for the indicial lift on a thin airfoil undergoing a transient step change in angle of attack. If the indicial response ϕ is known, then the unsteady loads due to arbitrary changes in angle of attack can be obtained through the superposition of indicial aerodynamic responses using the Duhamel integral [26] in equation (3.37); thus, the circulatory part of the lift coefficient, C_L^C, in response to an arbitrary variation in angle of attack is

$$C_L^C = 2\pi\left(\alpha(0)\,\phi_\alpha^C(s) + \int_0^s \frac{d\alpha(\tau)}{dt}\phi_\alpha^C(s-\tau)\,d\tau\right) \tag{3.37}$$

where τ is the time integration variable. In addition, noncirculatory lift contribution and pitching moment can be predicted by the Theodorsen theory (see Section 3.1.1) without inclusion of additional states, thus only two aerodynamic states are sufficient to fully describe attached-flow, unsteady loads. In details, these two states arise in the solution of the Duhamel integral in equation (3.37). This integral can be solved analytically or numerically. Analytical solutions are mostly restricted to simple forcing functions, thus numerical approach are employed in the general case. Equation (3.37) in frequency domain $\tilde{s}$ is

$$\tilde{C}_L^C = 2\pi\left[\alpha(0)\,\tilde{\phi}_\alpha^C(\tilde{s}) + \tilde{s}\tilde{\phi}_\alpha^C(\tilde{s})\,\tilde{\alpha} - \alpha(0)\,\tilde{\phi}_\alpha^C(\tilde{s})\right] = 2\pi\tilde{s}\tilde{\phi}_\alpha^C(\tilde{s})\,\tilde{\alpha} \tag{3.38}$$

Two term exponential approximation by Leishman [34] of the Wagner function is herein considered:

$$\phi_\alpha^C(t) = 1 - A_1 e^{-b_1\frac{2V}{c}t} - A_2 e^{-b_2\frac{2V}{c}t} \tag{3.39}$$

where A_1, A_2, b_1 and b_2 are empirical parameters which depend on the airfoil [32]. Then the corresponding impulse response, $h_\alpha^C(t)$, is given by

$$h_\alpha^C(t) = \frac{d}{dt}\left(\phi_\alpha^C(t)\right) = A_1 b_1 \frac{2V}{c} e^{-b_1\frac{2V}{c}t} + A_2 b_2 \frac{2V}{c} e^{-b_2\frac{2V}{c}t} \tag{3.40}$$

and its Laplace transform is

$$\mathcal{L}\left[h_\alpha^C(t)\right] = \frac{A_1 b_1 \frac{2V}{c}}{\tilde{s} + b_1\frac{2V}{c}} + \frac{A_2 b_2 \frac{2V}{c}}{\tilde{s} + b_2\frac{2V}{c}} = \tilde{s}\tilde{\phi}_\alpha^C(\tilde{s}) \tag{3.41}$$

Substituting equation (3.41) into equation (3.38) yields

$$\tilde{C}_L^C = 2\pi\left[\frac{A_1 b_1 \frac{2V}{c}}{\tilde{s} + b_1\frac{2V}{c}} + \frac{A_2 b_2 \frac{2V}{c}}{\tilde{s} + b_2\frac{2V}{c}}\right]\tilde{\alpha} \tag{3.42}$$

and denoting with $\tilde{x}_1 = \frac{\tilde{\alpha}}{\tilde{s}+b_1\frac{2V}{c}}$ and $\tilde{x}_2 = \frac{\tilde{\alpha}}{\tilde{s}+b_2\frac{2V}{c}}$ the final expression of the circulatory lift coefficient, in frequency domain, due to an arbitrary change in angle of attack is obtained:

$$\tilde{C}_L^C = 2\pi \left(A_1 b_1 \frac{2V}{c} \tilde{x}_1 + A_2 b_2 \frac{2V}{c} \tilde{x}_2 \right) \tag{3.43}$$

Time domain state-space form for the first two additional aerodynamic states is

$$\begin{cases} \dot{x}_1 = -\frac{2V}{c} b_1 x_1 + \alpha(t) \\ \dot{x}_2 = -\frac{2V}{c} b_2 x_2 + \alpha(t) \end{cases} \tag{3.44}$$

and, finally, from equation (3.43), the expression for the lift coefficient in time domain is

$$C_L^C = 2\pi \frac{2V}{c} \left(A_1 b_1 x_1 + A_2 b_2 x_2 \right) \tag{3.45}$$

For compressible flows, circulatory terms are modeled in the same way analyzed for incompressible flows, with the only modification to take into account comprimibility effects; impulsive terms are derived applying the piston theory[35]. To this aim, the indicial response is assumed to be idealized into two parts [36]: the first one is due to noncirculatory loading and plays the same role of the apparent mass terms presented in the incompressible formulation, whilst the second one is due to the circulatory loading. The indicial normal force and quarter chord pitching moment response to a step change in angle of attack α and a step change in pitch rate q can be written in general form as a function of nondimensional time s and Mach number M [34]

$$\begin{gathered} \frac{C_{N\alpha}(s)}{\alpha} = \frac{4}{M} \phi_\alpha^I(s, M) + \frac{2\pi}{\beta} \phi_\alpha^C(s, M) \\ \frac{C_{M\alpha}(s)}{\alpha} = -\frac{1}{M} \phi_{\alpha M}^I(s, M) + \frac{2\pi}{\beta} \phi_\alpha^C(s, M) \left(\frac{1}{4} - x_{ac}(M) \right) \\ \frac{C_{Nq}(s)}{q} = \frac{1}{M} \phi_q^I(s, M) + \frac{\pi}{\beta} \phi_q^C(s, M) \\ \frac{C_{Mq}(s)}{q} = -\frac{7}{12M} \phi_{qM}^I(s, M) - \frac{\pi}{8\beta} \phi_{qM}^C(s, M) \end{gathered} \tag{3.46}$$

where the indicial response functions are defined as

$$\begin{gathered} \phi_\alpha^C(t) = 1 - A_1 e^{-b_1 \beta^2 \frac{2V}{c} t} - A_2 e^{-b_2 \beta^2 \frac{2V}{c} t} \\ \phi_\alpha^I = e^{-\frac{t}{K_\alpha T_I}} \\ \phi_q^I = e^{-\frac{t}{K_q T_I}} \\ \phi_q^C = \phi_\alpha^C \\ \phi_{\alpha M}^I = A_3 e^{-\frac{t}{b_3 K_{\alpha M} T_I}} + A_4 e^{-\frac{t}{b_4 K_{\alpha M} T_I}} \\ \phi_{qM}^I = e^{-\frac{t}{K_{qM} T_I}} \\ \phi_{qM}^C = 1 - A_5 e^{-b_5 \beta^2 \frac{2V}{c} t} \end{gathered} \tag{3.47}$$

in which A_3, A_4, A_5, b_3, b_4 and b_5 are empirical coefficients [32], whilst, denoting with a the speed of sound in air, following definitions are used:

$$\begin{gathered} K_\alpha = \frac{0.75}{(1-M) + \pi \beta^2 M^2 (A_1 b_1 + A_2 b_2)} \\ T_I = \frac{c}{a} \\ K_q = \frac{0.75}{(1-M) + 2\pi \beta^2 M^2 (A_1 b_1 + A_2 b_2)} \\ K_{\alpha M} = \left[\frac{A_3 b_4 + A_4 b_3}{b_3 b_4 (1-M)} \right] \\ K_{qM} = \frac{7}{15(1-M) + 3\pi \beta M^2 b_5} \\ \beta = \sqrt{1 - M^2} \end{gathered} \tag{3.48}$$

Assuming a linear aerodynamic behavior of the airfoil, lift and moment response to a general input is achieved through the superposition of indicial responses. Following the procedure outlined for an arbitrary change in angle of attack (see equations (3.37) to (3.45)) [34], sectional forces and moment can be expressed as the sum of three contributions: attached flow impulsive terms (superscript I), taking into account noncirculatory effects under compressible flow assumption; circulatory terms (superscript f) corrected for trailing edge separation (if present); and vortex induced loads (superscript v):

$$\begin{aligned} C_N &= C_N^I + C_N^f + C_N^v \\ C_M &= C_M^I + C_M^f + C_M^v \\ C_C &= +C_C^f \end{aligned} \tag{3.49}$$

where $C_N = \frac{2N}{\rho V^2 c}$ and $C_C = \frac{2C}{\rho V^2 c}$ are airfoil normal and chord force coefficients, whilst $C_M = \frac{2M}{\rho V^2 c^2}$ is the pitching moment coefficient (see Figure 3.9). In the above definitions ρ is the fluid density. Finally, loads expression in the undeformed frame of reference to be introduced in equation (2.41) is:

$$\begin{Bmatrix} L_u^A \\ L_v^A \\ L_w^A \end{Bmatrix} = \mathbf{T}_{DU}^T \begin{Bmatrix} 0 \\ C \\ N \end{Bmatrix} \tag{3.50}$$

$$M_{\hat{\phi}}^A = M \tag{3.51}$$

Lift and drag coefficients in the deformed frame of reference are obtained as

$$\begin{aligned} C_L &= C_N \cos\alpha - C_C \sin\alpha \\ C_D &= C_N \sin\alpha + C_C \cos\alpha \end{aligned} \tag{3.52}$$

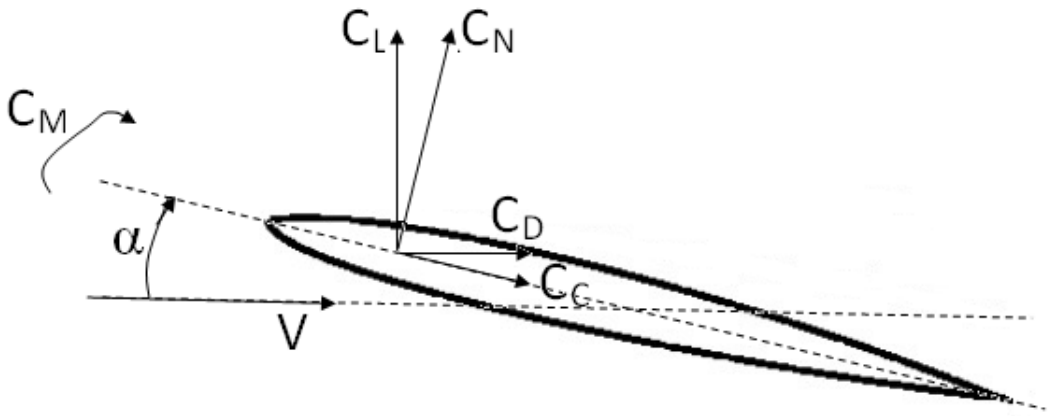

Figure 3.9: Directions of aerodynamic force and moment coefficients in the deformed frame of reference

Using expressions of indicial functions in equation (3.47) and following the same procedure illustrated for the derivation of the circulatory lift coefficient due to a step change in the angle of attack (written for incompressible flows), total aerodynamic normal force and pitching moment under unsteady attached flow are obtained and the

B-L state-space model is derived with the introduction of eight aerodynamic states $\mathbf{x} = (x_1, ..., x_8)^T$:

$$\begin{aligned} \mathbf{x}' &= \frac{c}{2V}\left(\mathbf{A}\mathbf{x} + \mathbf{B}\left\{\begin{array}{c} \alpha(s) \\ q(s) \end{array}\right\}\right) \\ \left\{\begin{array}{c} C_N^P(s) \\ C_M^P(s) \end{array}\right\} &= \mathbf{C}\mathbf{x} + \mathbf{D}\left\{\begin{array}{c} \alpha(s) \\ q(s) \end{array}\right\} \end{aligned} \tag{3.53}$$

where the time derivative is written in a nondimensional form and the superscript P indicates inviscid flow contributions. Expressions of state-space constant matrices in equation (3.53) are reported in AppendixC. Dealing with attached flow conditions, x_1 and x_2 take into account the effects of shed vorticity from trailing edge, thus being fully equivalent to the circulatory terms of the Theodorsen theory [25], as shown in Figure 3.10 where the hysteresis loop of normal force coefficient is presented. The first order ODEs governing these states are forced by the effective angle of attack at airfoil three-quarter chord point ($\alpha_{3/4}$) which can be expressed as a function of downwash, $w_{3/4}$, i.e. the component of the total airfoil velocity orthogonal to the chord and calculated at the rear neutral point

$$\alpha_{3/4} = \frac{w_{3/4}}{V} \tag{3.54}$$

where V is the free-stream velocity.

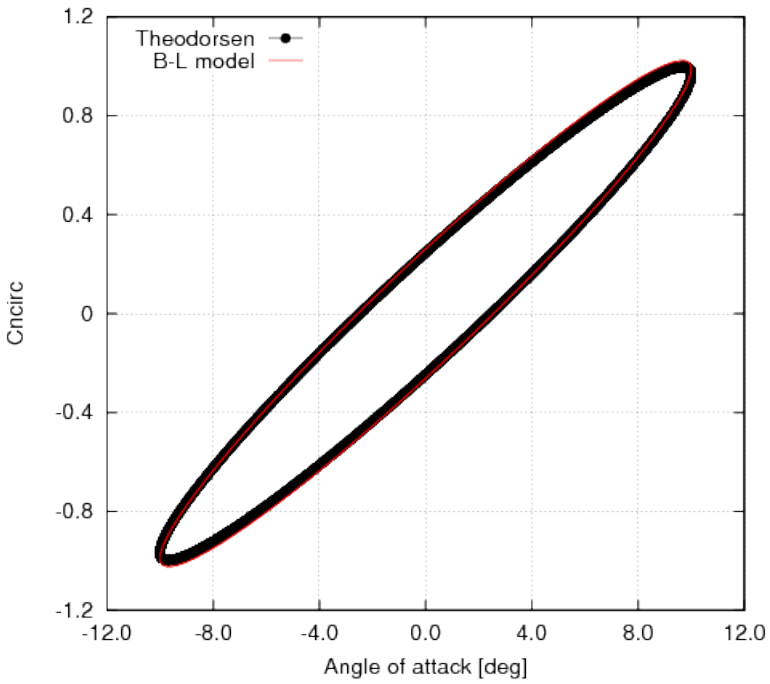

Figure 3.10: Normal force coefficient of a NACA0012 airfoil undergoing pitch motion ($k = 0.099$): comparison of B-L and Theodorsen formulations for unsteady attached flow

The next six states reproduce non circulatory loads accounting for flow compressibility. This aspect is crucial: at very low values of free stream velocity this formulation tends to provide singular values for aerodynamic loads, due to Mach number appearing at denominator of some terms of equation (3.35) [31]. Under these conditions, the

present formulation may be substituted by that for incompressible flows. The analysis of normal force coefficient hysteresis loop for a $NACA0012$ airfoil undergoing purely harmonic pitch motion between 0° and 20° (Figure 3.11) shows that for $M > 0.0015$ the original B-L model converges, whereas for lower Mach it is unstable.

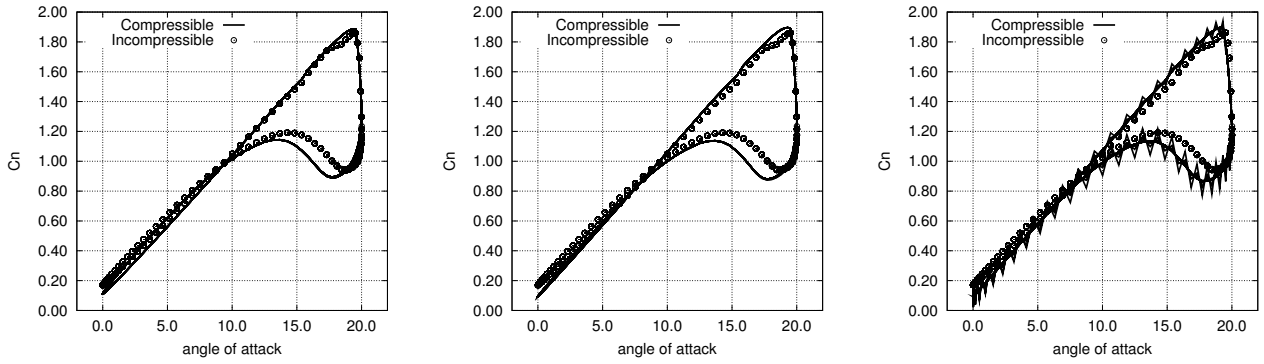

(a) $Mach = 0.3$ (b) $Mach = 0.0015$ (c) $Mach = 0.001$

Figure 3.11: Comparison between B-L model for compressible and incompressible flow

Separated flow conditions are considered through the remaining four aerodynamic states of the B-L model which can be added to both formulations for incompressible and compressible flows. Three aerodynamic states are introduced to simulate the effects of trailing edge separation. Specifically, for an airfoil undergoing unsteady motion such that the angle of attack is close to or greater than the static stall angle, flow separation onset is modeled through a time lag between separated and fully attached force coefficients (state x_9):

$$x'_9 = \frac{C_N^P - x_9}{T_p} \tag{3.55}$$

where T_p is a time constant dependent on Mach number [32].
This leads to the definition of a quasi-steady separation point characterized by a time lag with respect to the instantaneous angle of incidence. Progressive flow separation at trailing edge is governed by the dynamics of the boundary layer which leads to a time lag of the unsteady separation point (states x_{10} and x_{12}):

$$\begin{aligned} x'_{10} &= \frac{f\left(\frac{x_9}{C_{N\alpha}}, \alpha_1\right) - x_{10}}{T_f} \\ x'_{12} &= \frac{f(\alpha, \alpha_1) - x_{12}}{0.5\, T_f} \end{aligned} \tag{3.56}$$

where f is the separation point function that is equal to 1 for fully attached and 0 for fully separated flows, respectively. The parameter T_f is a time constant dependent on Mach number [32].
A widely used expression of the separation point function is

$$f(\alpha, \alpha_1) = \begin{cases} 1 - 0.3e^{\frac{|\alpha| - \alpha_1}{S_1}} & if\ 0 \le |\alpha| \le \alpha_1 \\ 0.04 + 0.66e^{\frac{\alpha_1 - |\alpha|}{S_2}} & if\ \alpha_1 < |\alpha| \end{cases} \tag{3.57}$$

The angle α_1 is defined as the point where $f = 0.70$, whilst S_1 and S_2 are empirical parameters functions of the Mach number [32].
Under separated flow conditions, unsteady sectional airloads coefficients are

$$\begin{gathered} C_N^f = C_N^C \left(\frac{1+\sqrt{x_{10}}}{2}\right)^2 \\ C_M^f = \left[K_0 + K_1\left(1-\hat{x}\right) + K_2 sin\left(\pi\hat{x}^2\right)\right] C_N^C \left(\frac{1+\sqrt{\hat{x}}}{2}\right)^2 \\ C_C^f = \eta C_{N\alpha}^S \left(\frac{C_N^C}{C_{N\alpha}^S}\right)^2 \sqrt{x_{10}} \end{gathered} \tag{3.58}$$

where

$$\hat{x} = \begin{cases} x_{10} & if\ \ x_{10} > x_{12} \\ x_{12} & if\ \ x_{10} \leq x_{12} \end{cases} \tag{3.59}$$

and K_0, K_1 and K_2 are parameters that depend on Mach number [32].
The last aerodynamic state represents leading edge separation (state x_{11}) and models the dynamic stall effect on airfoil unsteady loads ([29], [31]); this phenomenon occurs when the leading edge pressure reaches a critical value causing the shedding of a vortex traveling over the airfoil. The normal force and pitching moment generated under this condition are

$$C_N^v = x_{11} \tag{3.60}$$

$$C_M^v = \begin{cases} -0.25\left(1 - cos\left(\frac{\pi\tau_v}{T_{vl}}\right)\right) x_{11} & if\ \tau_v \leq 2T_{vl} \\ 0 & if\ \tau_v > 2T_{vl} \end{cases} \tag{3.61}$$

where τ_v is a nondimensional vortex time parameter (in semi-chords) such that $\tau_v = 0$ at the onset of separation and $\tau_v = T_{vl}$ when the vortex reaches the trailing edge. The parameter T_{vl} is determined empirically [30] from unsteady test data and depends on Mach number, whilst being relatively insensitive to the airfoil shape.
The contribution from C_N^v and C_M^v must be added to the loads in equation (3.58).
The state x_{11} is the solution of the ordinary differential equation

$$x_{11}' = \begin{cases} c_v' - \frac{x_{11}}{T_v} & if\ 0 < \tau_v < 2T_{vl} \\ -\frac{x_{11}}{T_v} & otherwise \end{cases} \tag{3.62}$$

The vortex feed, c_v, determines the strength of vortex induced normal force and it is defined as the instantaneous excess in normal force, $c_v = C_N^C - C_N^f$. The parameter T_v is determined as T_{vl} and depends only on Mach number. The lift increase effect of the traveling vortex on airfoil loads is shown in Figure 3.12 where the normal force coefficient for a $NACA0012$ airfoil undergoing harmonic pitch motion with amplitude 10° around a mean value of 10° is predicted by B-L model with and without the activation of the state x_{11}.

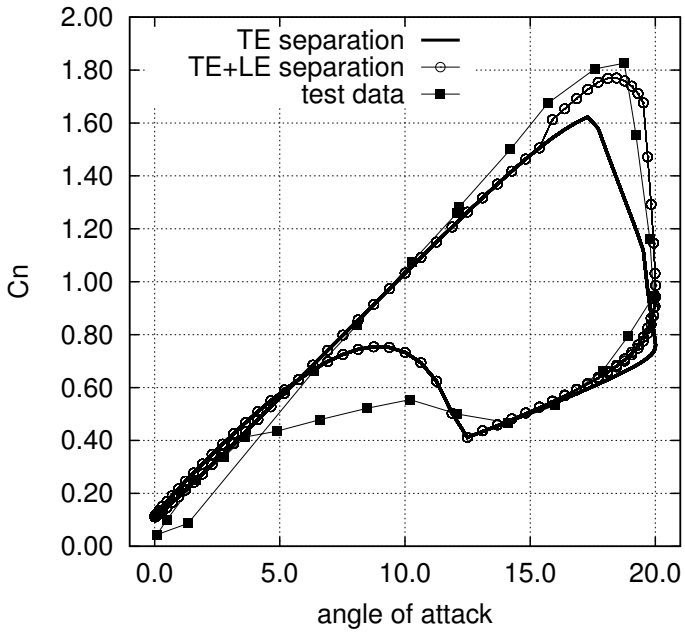

Figure 3.12: Comparison between B-L model and experimental data ($k = 0.099$)

3.1.3.1 Spectral approach for aerodynamics states integration

In this section a novel, and computationally efficient, technique for the spatial integration of additional states appearing in the sectional aerodynamic formulations is proposed; to this aim, a state-space representation of blade aerodynamics is required. The methodology is herein outlined coupling a pre-existent numerical tool based on a modal approach (see Section 2.6) to the state-space B-L aerodynamic model; the comparison with a strip theory approach (also used in the FEM formulation, see Section 2.4.2), consisting in solving the equations of the aerodynamic state variables at a discrete number of blade sections and then extending their values along the blade through interpolation, is performed in Section (4.2.2.1).

The novel approach has been specifically developed for Galerkin discretization; following Galerkin approach, blade elastic axis bending and cross-section torsion are described as linear combinations of suitable shape functions with time-dependent coefficients representing the system degrees of freedom governed by a set of ordinary differential equations. In order to introduce a number of aerodynamic states strictly related to the number of system degrees of freedom, first, sectional B-L model states $\mathbf{x}_{1-9} = \{x_1, ..., x_9\}$ are decomposed into contributions that are independent, $\mathbf{x}_{1-9}^{rig}$, and dependent on blade deformation. In turn, the latter are decomposed into contributions due to plunge and pitch motion, $\mathbf{x}_{1-9}^{bend}$ and torsion $\mathbf{x}_{1-9}^{tors}$, respectively forced by in-plane, v, and out-of-plane, w, blade bending deformation and torsion, ϕ. Specifically, starting from B-L model state equations

$$\dot{\mathbf{x}}_{1-9} + \mathbf{A}\mathbf{x}_{1-9} = \mathbf{f}\,(h,\, \alpha) \tag{3.63}$$

the corresponding subset written at any radial blade cross-section becomes

$$\begin{cases} \dot{\mathbf{x}}_{1-9}^{rig} + \mathbf{A}\mathbf{x}_{1-9}^{rig} = \mathbf{f}\left(\alpha^{rig}\right) \\ \dot{\mathbf{x}}_{1-9}^{bend} + \mathbf{A}\mathbf{x}_{1-9}^{bend} = \mathbf{f}\left(h^{bend}, \alpha^{bend}\right) \\ \dot{\mathbf{x}}_{1-9}^{tors} + \mathbf{A}\mathbf{x}_{1-9}^{tors} = \mathbf{f}\left(h^{tors}, \alpha^{tors}\right) \end{cases} \tag{3.64}$$

where

$$\begin{cases} \alpha^{rig} = \alpha\left(v = 0, w = 0, \phi = 0\right) \\ \alpha^{bend} = \alpha\left(v \neq 0, w \neq 0, \phi = 0\right) - \alpha\left(v = 0, w = 0, \phi = 0\right) \\ \alpha^{tors} = \alpha\left(v \neq 0, w \neq 0, \phi \neq 0\right) - \alpha\left(v \neq 0, w \neq 0, \phi = 0\right) \end{cases} \tag{3.65}$$

with $\alpha\left(v = 0, w = 0, \phi = 0\right)$ denoting the freestream rigid-blade local angle of attack, which depends on local blade pitch angle and wake inflow. Expressions similar to those in equation (3.65) may be written for h^{bend} and h^{tors}.

Then, the spanwise distribution of $\mathbf{x}_{1-9}^{bend}$ and $\mathbf{x}_{1-9}^{tors}$ is described through the same linear combination of shape functions used for blade bending deformation and torsion, respectively, followed by the application of the Galerkin approach to the ODEs governing $x_1 - x_9$ states (see Appendix D for details). It is worth noting that, in the present work the spanwise distribution of α^{rig} is described through a polynomial function of order n. Equations for the remaining states $x_{10} - x_{12}$ are piecewise continuous due to the presence of the separation point function [31] in functions $\mathbf{f}_{10-12}$ of equation (3.36), which is equal to 1 for attached flow, and 0 for fully separated flow. Thus, a strip theory approach is applied for their integration: blade span is divided into a finite number of segments where ODEs for $x_{10} - x_{12}$ are integrated independently.

Comparison between these two methodologies will be discussed in Section 4.2.2.1, in order to assess the numerical efficiency of the novel approach in terms of number of degrees of freedom and computational time.

3.2 Wake induced inflow models

In the framework of rotor aeroelasticity, an accurate estimate of the induced velocity field is mandatory. This is not known a priori because it depends on wake shape which, under rotor unsteady operating conditions, is quite complex and induces a highly nonuniform inflow over the rotor disk. Moreover, wake shape influences rotor airloads and trim conditions and, in turn, rotor aeroelasticity is influenced by wake inflow induced by the three-dimensional vortex system. In order to provide fast induced velocity predictions and achieve accurate sectional airloads computations, several wake inflow models are herein considered.

3.2.1 Hover condition: Blade Element Momentum Theory

The Blade Element Momentum Theory (BEMT) is a widely used method that combines the basic principle from the Blade Element and the Momentum Theory.

It is essentially a strip-theory based method and is inherently steady. It allows a quite reliable prediction of induced velocity along blade span for moderately loaded rotors working near their design condition (see [26]).

Considering a rotor in hover condition, for the present work the induced inflow is assumed to be steady and uniform along the blade radius and equal to the value of the inflow predicted by the blade element momentum

theory at the radial station $x = 0.75R$. At this station, the blade angle is set to be equal to blade collective pitch plus the equilibrium elastic twist ϕ_{75}. Thus, the expression of the nondimensional induced velocity is

$$\lambda_i = sgn\left[\theta_0 + \phi_{75}\right] \frac{\pi\sigma}{8} \left(\sqrt{1 + \frac{16}{\pi\sigma} \left|\theta_0 + \phi_{75}\, 0.75\right|} - 1 \right) \tag{3.66}$$

where $\sigma = \frac{N_b c}{\pi R}$ is blade solidity, N_b is the number of rotor blades and sgn indicates the sign function.

3.2.2 Forward flight condition: Drees linear inflow

For a rotor in forward flight, the Momentum Theory provides a simple expression of induced inflow as a function of rotor thrust coefficient (C_T), advance ratio (μ) and rotor shaft angle (α_s). Using this approach the inflow is considered uniform over the rotor disk. In details, the total inflow ratio λ is expressed as

$$\lambda = \mu \tan\alpha_s + \lambda_i = \mu \tan\alpha_s + \frac{C_T/2}{\sqrt{\lambda_i^2 + \mu^2}} \tag{3.67}$$

In order to take into account a more realistic nonuniform distribution of wake inflow, a linear variation of induced velocity across the rotor disk can be assumed as follows

$$\lambda_i = \frac{C_T/2}{\sqrt{\lambda_i^2 + \mu^2}} \left(1 + \kappa_x \cos\psi + \kappa_y \sin\psi\right) \tag{3.68}$$

where ψ is the azimuth angle.
The parameters κ_x and κ_y are weighting factors representing the deviation of the inflow from the uniform value predicted by the Momentum Theory. Several attempts to directly calculate κ_x and κ_y are found in literature ([37, 23]). A widely used model by Drees is based on the vortex theory (see [23]) and provide the following expressions:

$$\begin{gathered} \kappa_x = \tfrac{4}{3} \left[\left(1 - 1.8\mu^2\right) \sqrt{1 + \left(\tfrac{\lambda}{\mu}\right)^2} - \tfrac{\lambda}{\mu} \right] \\ \kappa_y = -2\mu \end{gathered} \tag{3.69}$$

Substituting equations (3.69) into (3.68) and applying Newton-Raphson iterative method, the numerical evaluation of the nonuniform inflow distribution over the rotor disk is straightforward.

3.2.3 Three-dimensional Boundary Element Method

An accurate three-dimensional wake inflow is herein predicted by a Boundary Element Method (BEM) for attached, incompressible flows [38, 39]. This solver is based on a boundary integral formulation for potential flows around lifting bodies, which is suitable for describing three-dimensional, unsteady flow effects through a free-wake solution scheme. Following [39] and [20], once the solution of velocity potential is provided by BEM formulation, wake inflow is determined as follows

$$\vec{v}_i\left(\vec{x}, t\right) = \nabla_x \varphi\left(\vec{x}\right) = -\int_{S_w} \Delta\varphi^{TE}\left(\vec{y}_{TE}, t - \tau\right) \nabla_x \left(\frac{\partial G}{\partial n} \right) ds\left(\vec{y}\right) \tag{3.70}$$

where $\vec{x}$ denoting a field point, S_w the convected wake (i.e. a zero-thickness layer departing from the trailing edge of lifting bodies where generated vorticity is released downstream) and $\vec{y}$ a point on the boundary surfaces. Furthermore, G and $\frac{\partial G}{\partial n}$ are the unit source and (normal) dipole, respectively, whereas ∇_x denotes gradient operating on $\vec{x}$. In addition, $\Delta\varphi^{TE}(\vec{y}_{TE}, t-\tau)$ indicates the potential jump at trailing edge position $\vec{y}_{TE}$ where the wake material point currently in $\vec{y}$ emanated at time $t-\tau$. The evaluation of $\vec{v}_i$ near the blade tip is critical due to the presence of concentrated wake singularities: in order to assure a stable and regular numerical solution, a finite-thickness vortex model yielding a finite distribution of velocity within the vortex core is introduced.
In order to reduce computational effort, blade deformation effects are neglected in the BEM flow solution. This approximation is acceptable as long as turbine blades are subject to small deformations. Moreover, for the present applications the wake inflow considered is that evaluated by the BEM solver for the steady reference (equilibrium) condition.

3.3 Enhancement of 2D sectional loads modelling

In the framework of dynamic stall modeling, CFD computations would give more accurate predictions of the unsteady loads because of their attitude in describing massive recirculating, turbulent, separated flow regimes. However, in many problems of industrial interest, CFD requires a computational effort that is prohibitive, especially in view of preliminary design and multidisciplinary optimization applications. Thus, the hybrid formulation herein proposed represents a trade-off between accuracy of simulation and computational effort. Indeed, in this section focus is posed on the modification to the B-L sectional aerodynamic formulation to take into account 3D rotor wake inflow effects on sectional airloads as well as on the inclusion of semi-empirical corrections to improve aerodynamic predictions at high angles of attack. The latter corrections are widely used to provide realistic overall performance predictions at reduced computational costs.

3.3.1 Wake inflow correction by a 3D Boundary Element Method

The B-L model is two-dimensional. For the evaluation of rotating blades cross-section airloads, a satisfactory level of prediction accuracy is obtained by including three-dimensional rotor wake inflow effects. This consists in determining the effective downwash at the 3/4 chord point of each blade section (namely, the kinematic variable including sectional circulation) [25] as the result of combination of local plunge and pitch motion due to blade deformation with flow velocity induced by wake vorticity. Here, wake inflow is predicted by a BEM formulation. Four different methods for including rotor wake effects into the B-L model are proposed and described in the following.

Method 1 This approach consists in evaluating blade section airloads through the B-L model (Section 3.1.3) with downwash corrected by the 3D wake inflow provided by the aerodynamic BEM solver (see Section 3.2.3). In details, for the B-L model applied to a discrete number of blade sections distributed spanwise, the perturbation velocity induced by the rotor wake is evaluated at the rear neutral point of each section and is used to modify/enhance the downwash forcing the ODEs governing the aerodynamic states x_1 and x_2 in equation (3.44). Note that the shed vorticity generated by blade sections is already taken into account by the attached-flow contribution to the B-L theory, thus its contribution to wake inflow is neglected. Finally, downwash induced

by the wake combined with blade motion yields the effective angle of attack $\alpha_{eff}^{3/4}$ at each blade section to be included in the B-L aerodynamic model:

$$\alpha_{eff}^{3/4}(r) = -\frac{U_P^{3/4}}{U_T^{3/4}} \tag{3.71}$$

Method 2 Section airloads associated to attached flow are evaluated by the BEM solver, therefore replacing loads given by the first eight aerodynamic states of the B-L model. Specifically, from the velocity potential solution over blade surface, the Bernoulli theorem provides pressure, and then sectional airloads are determined by integration. Thus, three-dimensional effects due to shed and trailing wake vorticity, as well as mutual interaction effects amongst blades are fully taken into account. The remaining B-L aerodynamic states are retained to predict airloads correction due to flow separation (specifically, the ordinary differential equation describing the onset of leading edge separation is forced by section normal force coefficient provided by BEM).

Method 3 The complete 12-states B-L model provides both sectional airloads (akin to Method 1) and wake vorticity released at trailing edge. Specifically, first the section lift coefficient, C_L, determined by the B-L model is used to evaluate the corresponding bound circulation, Γ_{BL}, as given by the Kutta-Joukowski theorem, $\Gamma_{BL} = \frac{1}{2}cV_wC_L$; then, observing that in velocity potential formulations bound circulation coincides with potential jump at trailing edge, equation (3.70) is applied to evaluate wake inflow at the three-quarter chord point of each section (as in Method 1), with $\Delta\varphi^{TE} = \Gamma_{BL}$.

Method 4 Methods 2 and 3 are combined: attached-flow sectional load contributions are evaluated through the aerodynamic BEM solver, whilst separated-flow corrections are determined by the B-L model. Akin to Method 3, the resulting sectional lift coefficients provide the spanwise distribution of $\Delta\varphi^{TE}$ to be used in equation (3.70) for wake inflow evaluation.

3.3.2 Semi empirical corrections for high angle of attack conditions

The capability of the proposed methodologies to predict local and global airloads of wind turbines in the presence of flow separation is limited to light stall. At high angles of attack, deep stall and post-stall regimes are characterized by massive flow separation, and a strip theory approach combining three-dimensional potential flow and airfoil viscous flow aerodynamics fails. These complex flow conditions are very hard to be simulated even through advanced CFD solvers. In theses cases, in the framework of aerodynamic formulations applied within aeroelastic tools for preliminary design of wind turbines, semi-empirical corrections are typically introduced to provide realistic overall performance predictions at reduced computational costs. To this aim, following the Viterna-Corrigan approach (see Section 3.3.2.1), static aerodynamic coefficients can be extended by flat plate theory approximation to high angle-of-attack operation range, where experimental lift and drag airfoil characteristics are not easily available [40].

Due to the centrifugal pumping effect that reduces blade surface adverse pressure gradient, stall regime for rotating blades starts at higher angles of attack with respect to airfoils statically tested in wind tunnels [40]. A widely used empirical description of this effect, based on the laminar boundary layer theory, is used (see Section 3.3.2.2).

3.3.2.1 Viterna-Corrigan approach

Dealing with rotating blades aerodynamics, it is necessary to extend 2D static aerodynamic coefficients between the range $-180^\circ < \alpha < +180^\circ$ for operations at high angles of attack of the section that occur in deep stall regimes, where no experimental data are available [40]; thus, Viterna-Corrigan model, that predicts force coefficients beyond 2D static lift and drag characteristics using a flat-plate approximation, is introduced. In details, sectional force coefficients can be expressed as

$$\begin{aligned} C_L &= \tfrac{1}{2} C_{D,max} \sin 2\alpha + K_L \tfrac{(\cos\alpha)^2}{\sin\alpha} \\ C_D &= C_{D,max} \left(\sin\alpha\right)^2 + K_D \cos\alpha \end{aligned} \tag{3.72}$$

where

$$\begin{aligned} K_L &= \tfrac{(C_{L,S} - C_{D,max} \sin\alpha_s \cos\alpha_s) \sin\alpha_s}{(\cos\alpha_s)^2} \\ K_D &= \tfrac{\left(C_{D,S} - C_{D,max} (\sin\alpha_s)^2\right)}{\cos\alpha_s} \end{aligned} \tag{3.73}$$

in which α_s is the angle of attack where the maximum of lift coefficient is observed, $C_{L,S}$ and $C_{D,S}$ denote lift and drag coefficients at stall angle α_s, respectively, and $C_{D,max}$ is the maximum drag coefficient. Within the framework of Viterna-Corrigan stall model, $C_{D,max}$ depends on the aspect ratio δ (defined as the ratio between blade span and mean chord) as follows:

$$\begin{cases} 1.11 + 0.018\delta & \delta \leq 50 \\ 2.01 & \delta > 50 \end{cases} \tag{3.74}$$

The case $\delta > 50$ may be interpreted as an infinite blade whose aerodynamic properties are fully described by 2D aerodynamic coefficients, whereas the case $\delta \leq 50$ also considers 3D (finite span) effects.

3.3.2.2 Snel model for centrifugal pumping effects

For rotating blades, it has been observed that stall regime starts at higher angles of attack as compared with wind tunnel measurements on static airfoils [40]. This has been attributed to centrifugal pumping effects, reducing the adverse pressure gradient that leads to airfoil stall. A widely used empirical description of this effects based on the laminar boundary layer theory is given by Snel [41].
The increase of the aerodynamic lift coefficient due to the effect of rotation is formulated through comparison with experimental measurements [42]. In details, the lift coefficient for a rotating blade airfoil ($C_{L,rot}$) is provided by

$$C_{L,rot} = C_{L,nrot} + 3.1 \left(\frac{\Omega r}{V_{eff}}\right)^2 \cdot \left(\frac{c}{r}\right)^2 \cdot \left(C_L^P - C_{L,nrot}\right) \tag{3.75}$$

where $C_{L,nrot}$ is the lift coefficient for non rotating blade airfoil, C_L^P is the lift coefficient associated to attached flow (see equation (3.53)), c is the section chord, r defines the radial position on the blade, Ω is the angular rotor speed and V_{eff} is the effective wind velocity on a blade section.
The maximum value of the rotating lift coefficient in equation (3.75) is obtained in a full laminar flow, due to the strongest effects of centrifugal and Coriolis loads.

3.4 Derivation of airfoil velocity components

Due to aeroelastic similarities between helicopter and wind turbine rotor the formulation is derived for a helicopter rotor blade; however, at the end of this section, the modifications for a wind turbine rotor are discussed.

A crucial issue for the determination of the sectional aerodynamic loads is the definition of the angle of attack that is defined as

$$\tan\alpha = -U_P/U_T \tag{3.76}$$

where U_P and U_T are the normal and parallel velocity components to the airfoil chord) at a certain point of the blade section chord (see Figure 3.13). It depends on the incident velocity which can be expressed as the sum of the contribution due to blade rigid motion, rotor induced velocity and blade deformation as

$$\vec{V} = -\vec{V}_w + \vec{V}_b \tag{3.77}$$

where $\vec{V}_w$ is the wind velocity with contributions from the rotor forward speed and wake and $\vec{V}_b$ is the velocity of a blade point relative to the hub fixed frame resulting from blade rotation and deformation. To have a direct coupling between the aerodynamic loads and the dynamics of the blade, the velocity components must be expressed in terms of blade degrees of freedom. This procedure is explained in the following.

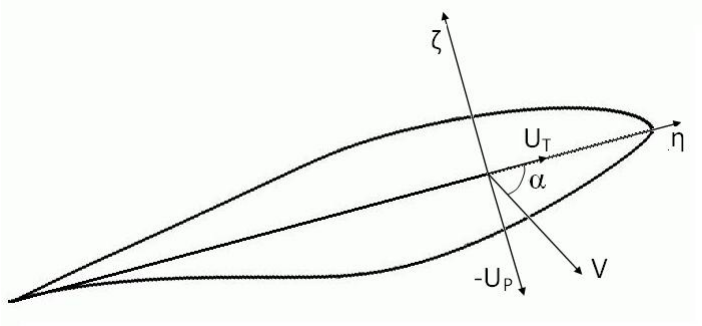

Figure 3.13: Definition of the angle of attack

Wind velocity The expression for the wind velocity is (see Figure 3.14)

$$\vec{V}_w = (\mu\Omega R)\,\hat{I}_H - (\lambda\Omega R)\,\hat{K}_H \tag{3.78}$$

where $\mu = \frac{V cos\alpha_s}{\Omega R}$ is the rotor advance ratio (being V its forward speed), α_s is the rotor shaft tilt, positive forward, λ is the rotor non-dimensional inflow and ΩR is the rotor tip speed. The rotor inflow is expressed as

$$\lambda = \mu\tan\alpha_s + \lambda_i \tag{3.79}$$

where $\mu\tan\alpha_s$ is the component of the forward flight velocity perpendicular to the rotor tip path plane and $\lambda_i = v_i/\Omega R$ is the non dimensional rotor induced inflow due to the vorticity released by the wake.

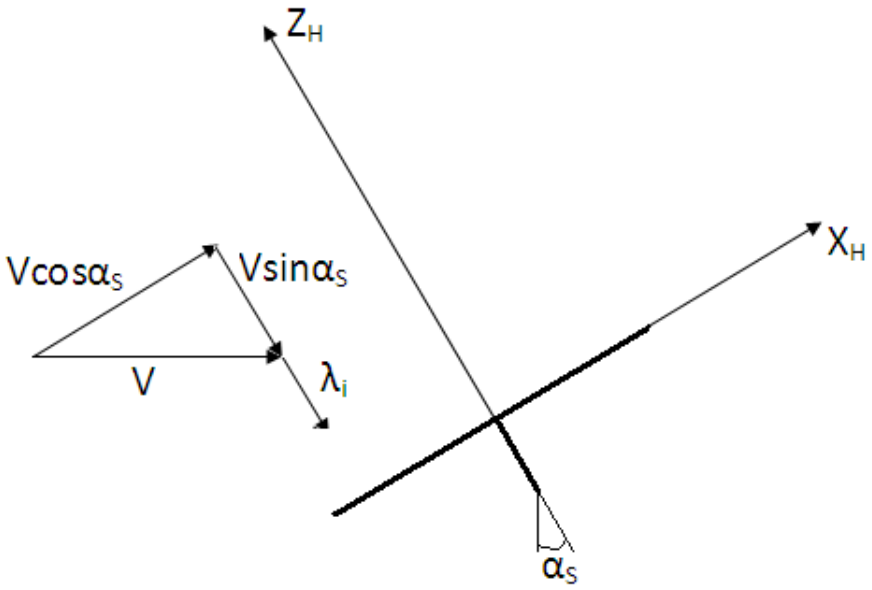

Figure 3.14: Wind velocity components

The velocity components in equation (3.78) are expressed in the non rotating system; to express them in the rotating undeformed frame two transformations (defined in Section 2.1) are required, the first from the non rotating to the rotating frame:

$$\left\{ \begin{array}{c} \hat{I} \\ \hat{J} \\ \hat{K} \end{array} \right\} = \mathbf{T}_{RH} \left\{ \begin{array}{c} \hat{I}_H \\ \hat{J}_H \\ \hat{K}_H \end{array} \right\} \tag{3.80}$$

and the second from the rotating to the undeformed reference system:

$$\left\{ \begin{array}{c} \hat{i} \\ \hat{j} \\ \hat{k} \end{array} \right\} = \mathbf{T}_{UR} \left\{ \begin{array}{c} \hat{I} \\ \hat{J} \\ \hat{K} \end{array} \right\} \tag{3.81}$$

Assuming a small precone angle β_{pc}, wind velocity components in the blade undeformed coordinate system are

$$\left\{ \begin{array}{l} V_{wx} = \mu\Omega R\cos\psi - \lambda\Omega R\beta_{pc} \\ V_{wy} = -\mu\Omega R\sin\psi \\ V_{wz} = -\mu\Omega R\cos\psi\beta_{pc} - \lambda\Omega R \end{array} \right. \tag{3.82}$$

Blade motion velocity The general expression for the velocity of a blade point with respect to the rotating undeformed frame is

$$\vec{V}_b = \dot{\vec{r}} + \vec{\Omega} \times \vec{r} \tag{3.83}$$

where

$$\begin{gathered}\vec{r} = x_1\hat{i} + y_1\hat{j} + z_1\hat{k} \\ \dot{\vec{r}} = \dot{x}_1\hat{i} + \dot{y}_1\hat{j} + \dot{z}_1\hat{k} \\ \vec{\Omega} = \Omega\hat{K}\end{gathered} \tag{3.84}$$

Vector $\vec{r}$ denotes the position vector of a point P (ξ, η, ζ) of a given cross section of the deformed rotating blade with respect to the hub. The contributions to $\vec{r}$, that depend on blade deformation and rigid rotation, are calculated at an arbitrary position (η, ζ) for each cross section identified by ξ in the deformed blade frame of reference. Vector $\dot{\vec{r}}$ represents the relative velocity of point P, expressed in the undeformed frame of reference. Finally, $\vec{\Omega}$ is the angular velocity of the rotating coordinate system. The final expressions of blade velocity contribution are

$$\begin{cases} V_{bx} = \dot{u} - \left(\dot{v}' + w'\dot{\theta}_1\right)\eta_r\cos\theta_1 - \left(\dot{w}' + v'\dot{\theta}_1\right)\eta_r\sin\theta_1 - \Omega\left(v + \eta_r\cos\theta_1\right) \\ V_{by} = \dot{v} - \dot{\theta}_1\eta_r\sin\theta_1 + \Omega\left[x + u - v'\eta_r\cos\theta_1 - w'\eta_r\sin\theta_1 - \left(w + \eta_r\sin\theta_1\right)\beta_{pc}\right] \\ V_{bz} = \dot{w} + \dot{\theta}_1\eta_r\cos\theta_1 + \Omega\beta_{pc}\left(v + \eta_r\cos\theta_1\right) \end{cases} \tag{3.85}$$

Airfoil velocity components Blade section loads are calculated using the section resultant velocity $\vec{V}$ of equation (3.77) expressed in the deformed blade frame to provide blade section angle of attack. Therefore, the velocity components in the undeformed frame need to be transformed to the deformed one:

$$\begin{Bmatrix} U_R \\ U_T \\ U_P \end{Bmatrix} = \mathbf{T}_{DU} \begin{Bmatrix} V_{wx} + V_{bx} \\ V_{wy} + V_{by} \\ V_{wz} + V_{bz} \end{Bmatrix} \tag{3.86}$$

where $\mathbf{T}_{DU}$ is defined in Section 2.1. Expanding $\cos\theta_1$ and $\sin\theta_1$ appearing in equation (2.8), assuming that $\hat{\phi}$ is a small angle and using the ordering scheme introduced in Section 2.2, the final expressions for the nondimensional airfoil velocity components in the rotating deformed frame are:

$$\begin{gathered}\tfrac{U_R}{\Omega R} = \dot{u} - v + v'\left(x + \mu\sin\psi\right) - \mu\cos\psi\left(1 - \beta_{pc}w'\right) + \lambda\left(\beta_{pc} + w'\right) - \eta_r\cos\theta_0\left(1 + \dot{v}'\right) + \\ + \eta_r\sin\theta_0\left(\hat{\phi} - \dot{w}'\right) + v'\dot{v} + w'\dot{w} + \tfrac{1}{2}\mu\cos\psi\left(v'^2 + w'^2\right)\end{gathered} \tag{3.87}$$

$$\begin{gathered}\tfrac{U_T}{\Omega R} = \cos\theta_0\left[\dot{v} + u - w\beta_{pc} + \hat{\phi}\left(\lambda + \dot{w}\right) + v'v + \left(x + \mu\sin\psi\right)\left(1 - \tfrac{v'^2}{2}\right) + \mu\cos\psi\left(v' + \hat{\phi}\left(\beta_{pc} + w'\right)\right)\right] + \\ + \sin\theta_0\left[\dot{w} + \lambda + v\left(\beta_{pc} + w'\right) - \hat{\phi}\dot{v} - \left(x + \mu\sin\psi\right)\left(v'w' + \hat{\phi}\right) + \mu\cos\psi\left(w' + \beta_{pc} - \hat{\phi}v'\right)\right]\end{gathered} \tag{3.88}$$

$$\begin{gathered}\tfrac{U_P}{\Omega R} = \cos\theta_0\left[\dot{w} + \lambda + \beta_{pc}v + vw' + \mu\cos\psi\left(\beta_{pc} + w' - \hat{\phi}v'\right) - \left(x + \mu\sin\psi\right)\left(v'w' + \hat{\phi}\right)\right] + \\ + \sin\theta_0\left[-\dot{v} - u - vv' + w\beta_{pc} - \hat{\phi}\left(\lambda + \dot{w}\right) - \left(x + \mu\sin\psi\right)\left(1 - \tfrac{v'^2}{2}\right) - \mu\cos\psi\left(v' + \hat{\phi}\left(\beta_{pc} + w'\right)\right)\right] + \\ + \eta_r\left(\dot{\theta}_0 + \dot{\hat{\phi}} + w' + \beta_{pc}\right)\end{gathered} \tag{3.89}$$

3.4.1 Equivalence for wind turbine rotor blade section

Analyzing the blade section angle of attack, the only difference between helicopter and wind turbine rotor relies in the definition of the airfoil velocity component perpendicular to the chord (see Figure 3.15). In this case, in order to have a positive lift for positive angles of attack, the airfoil incidence is computed as

$$\tan\alpha = U_P/U_T \tag{3.90}$$

where U_T and U_P are defined in equations (3.88) and (3.89).

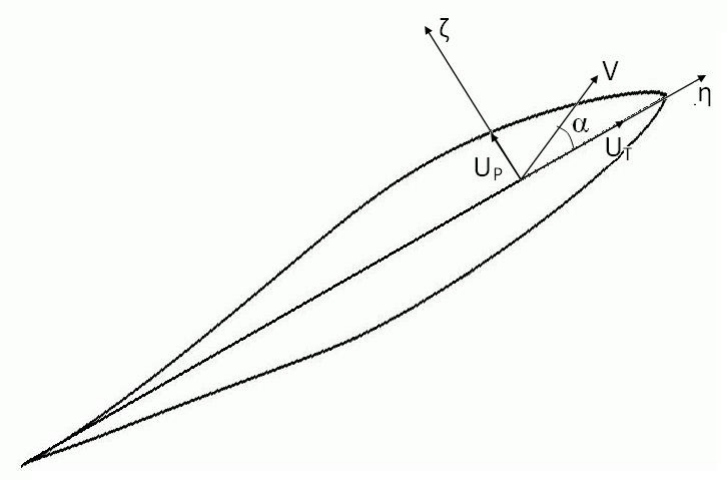

Figure 3.15: Definition of the angle of attack for a wind turbine rotor blade section

Chapter 4

Numerical results

In this chapter numerical results obtained by the developed numerical tools are presented and discussed. In order to correctly predict the performance of wind turbine rotors with a well assessed aeroelastic code, validation is carried out starting from the simplest components and adding complexity step by step. Thus, the first application is performed on 2D airfoils in pitch motion with sectional aerodynamic loads provided by the B-L model. Then, enhancements of this model for three dimensional analyses are developed and applications on translating wings and on wind turbine rotor blades are carried out using pre-existent tools in which the aerodynamic sectional B-L model is included (semi-empirical models are also considered to characterize high angle of attack regimes). Finally, structural and aeroelastic validation of the FEM-based aeroelastic tool is proposed: due to similarities between helicopter and wind turbine rotors, applications on helicopter rotors are firstly discussed, then the analysis of wind turbine rotor performance is presented.

4.1 Validation of Beddoes-Leishman model for 2D airfoils

The B-L model is herein validated through the analysis of 2D airfoils undergoing harmonic pitch motion about the quarter-chord point. Numerical results are compared to experimental data. Figure 4.1 presents the aerodynamic normal force and moment coefficients hysteresis loops for the $NACA0012$ airfoil [31] for the motion law $\alpha(s) = 10 + 10sin(ks)$ where $k = 0.099$ whereas Figure 4.2 shows similar results for the S809 airfoil [43] (Figure 4.3) oscillating about a mean angle of 7°, with amplitude of 10° and reduced frequency of 0.077. For both test cases, numerical predictions show that the proposed implementation of the B-L model reproduces C_N and C_M magnitude with reasonable accuracy in the considered range of α. Slight overestimation on C_N is observed in the reattachment phase during the downstroke for the normal force coefficient, whereas major discrepancies appear on C_M, even if the general quality of the numerical data is still reasonable. The reduced accuracy of the B-L model for the reattachment phase is confirmed in the work of Leishman and Crouse [31]. Indeed, during this phase, the inherent randomness of the flow induces significant variations of the airloads over the airfoil, and thus, its behavior during the downstroke phase is more difficult to be simulated. Nevertheless, the overall quality of predictions remains satisfactory. Greater differences in the hysteresis loop of the moment coefficient are evidenced on the $S809$ airfoil. A devoted tailoring of the semi-empirical coefficients appearing in the aerodynamic formulation should improve the numerical predictions: the present analysis has been performed

by using the same set of parameters provided by [31] for the NACA airfoil.

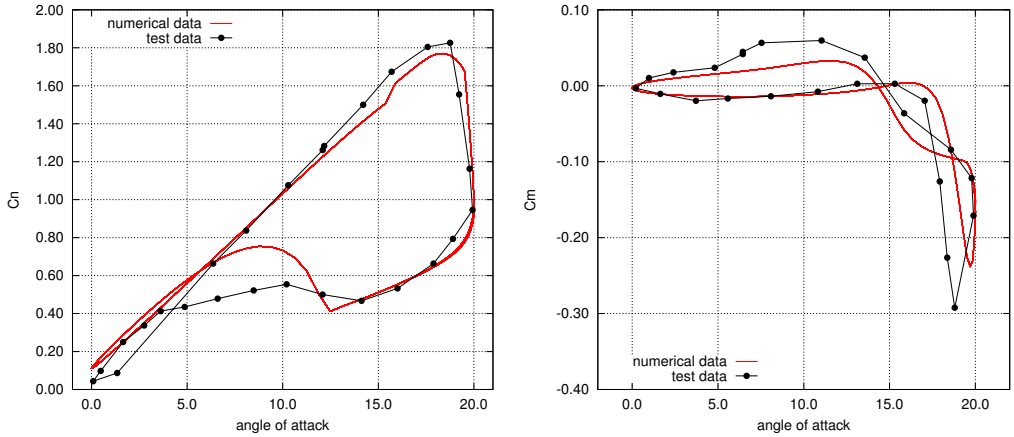

Figure 4.1: Normal force (left) and moment (right) coefficients for the NACA0012 airfoil

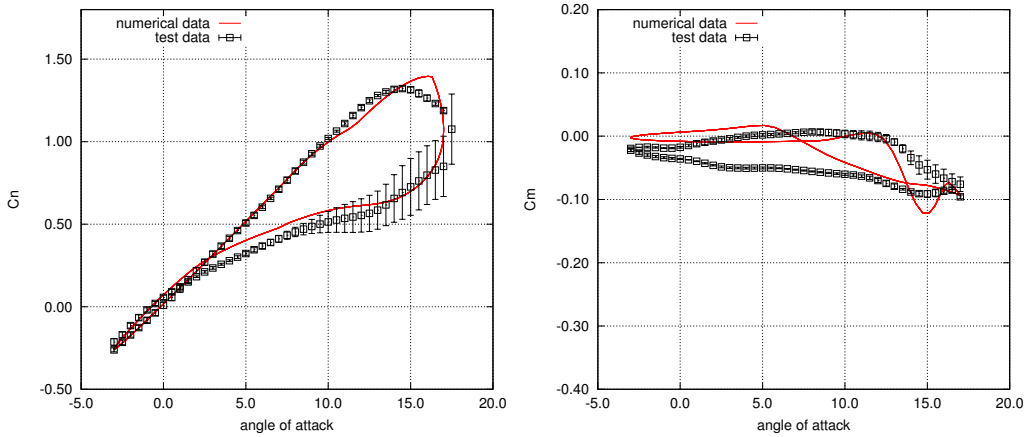

Figure 4.2: Normal force (left) and moment (right) coefficients for the $S809$ airfoil

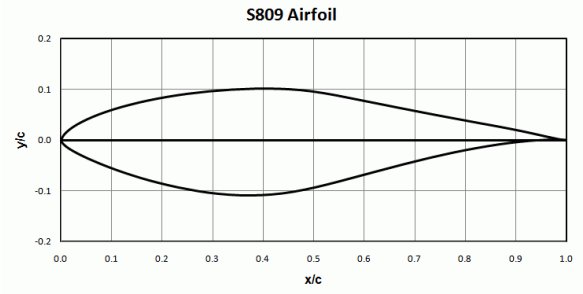

Figure 4.3: S809 airfoil

4.2 3D applications of Beddoes-Leishman model

4.2.1 Oscillating finite wing

Validation of the enhanced B-L aerodynamic model herein proposed is accomplished through application to oscillating finite-span wings and comparison with experimental results. Indeed, in this context, a wide experimental activity has been performed in 2013 at the CNR-INSEAN towing-tank on 3D translating-pitching wings with different sectional shapes. These tests have demonstrated to be a valid tool for the assessment of dynamic stall models [44].

The experimental activity has been focused on the measurement of unsteady hydrodynamic loads acting on translating and harmonically pitching wings, in order to characterize dynamic stall onset. With this aim, the wind is mounted below the water surface on a carriage translating at selected advance speeds, whilst a combined mechanical/electronical device denoted as Planar Motion Mechanism (PMM) allows the wing motion control by combining sinusoidal and non-sinusoidal signals. The main drive system's features are reported in Table 4.1.

Device	Manufacturer	Model	Features
Motor	Kollmorgen	AKM83T	Power: 16100 W Max torque: 130 Nm with resolver or encoder
Servo amplier	Kollmorgen	ServoStar 772	70A .3*480V 50/60 Hz

Table 4.1: PMM's drive system components and their main features

The instantaneous angular position of the wing, with respect to the water-flow direction, is measured by transducers placed on the rotational axis whereas an appropriately designed dynamometric balance, located above the free-surface and instrumented by LVDT (Linear Variable Displacement Transducers) sensors, yields transversal and longitudinal hydroloads measurements. A flange connects the submerged wing both to the balance and the rotating part of the PMM device. Since free surface effects are largely unavoidable with this setup, the presence of a canoe completes the experimental set-up (Figure 4.4) .

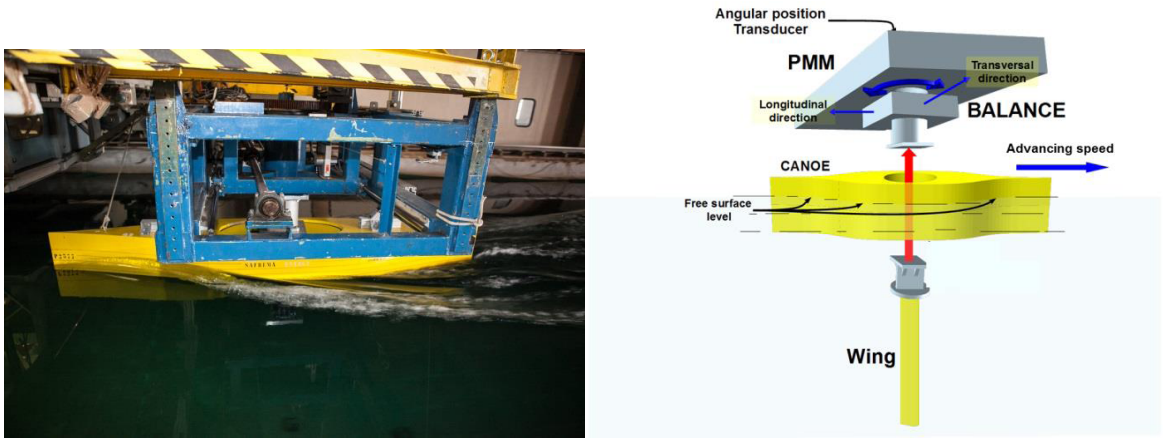

Figure 4.4: Experimental setup

The wing examined in the following is straight, rectangular, with $S809$ airfoil non-twisted cross sections (Figure 4.3), span $b = 1.12\,m$, chord $c = 0.225\,m$, translating at constant speed, V , and oscillating about the

quarter-chord axis. Test conditions, summarized in Table 4.2, are such that no cavitation occurs, with the angle of attack range that is large enough to induce leading edge separation. These data represent only a small part of the experimental campaign designed with the specific aim of fully validating the proposed aerodynamic models at different operating conditions (Reynolds number, pitching motion reduced frequency, advance speed).

Reynolds number	1160000
Advance speed	$5.173\,m/s$
Mean pitch angle	8°
Pitching amplitude	10°
Pitching frequency	$0.6\,Hz$

Table 4.2: $S809$ wing test conditions

Numerical results are obtained using a BEM solver in which B-L model is used to predict lift and drag coefficients through the four aerodynamic coupling methods described in Section 3.3.1. Numerical airloads predictions are compared with those measured experimentally in Figure 4.5. They are defined as

$$\begin{aligned} C_L &= \frac{2L}{\rho V^2 bc} \\ C_D &= \frac{2D}{\rho V^2 bc} \end{aligned} \tag{4.1}$$

with L and D denoting wing lift and drag, whereas ρ is the fluid medium density. Dynamic stall onset is characterized by increase of lift with respect to static values and by considerable loads hysteresis. These correlations demonstrate that the proposed aerodynamic models are able to capture the main features of unsteady wing aerodynamics and of dynamic stall phenomena. Indeed, all aerodynamic models show a satisfactory capability to predict lift coefficient in the pitch oscillation range examined. However, the correlation of Methods 1 and 3 with experimental data is of excellent accuracy, whilst Methods 2 and 4 tend to underestimate lift increase induced by the leading edge vortex traveling along the upper part of the wing. All methods applied present good accuracy of drag coefficient predictions in the upstroke phase of wing motion, but these are overestimated during the downstroke phase. This reduced accuracy of the B-L model is confirmed in [31]. As for the case of the 2D airfoil (see Section 4.1), the B-L model shows a reduced accuracy in the flow reattachment phase. The consequence on drag prediction is evident. Nevertheless, the overall quality of predictions remains satisfactory.

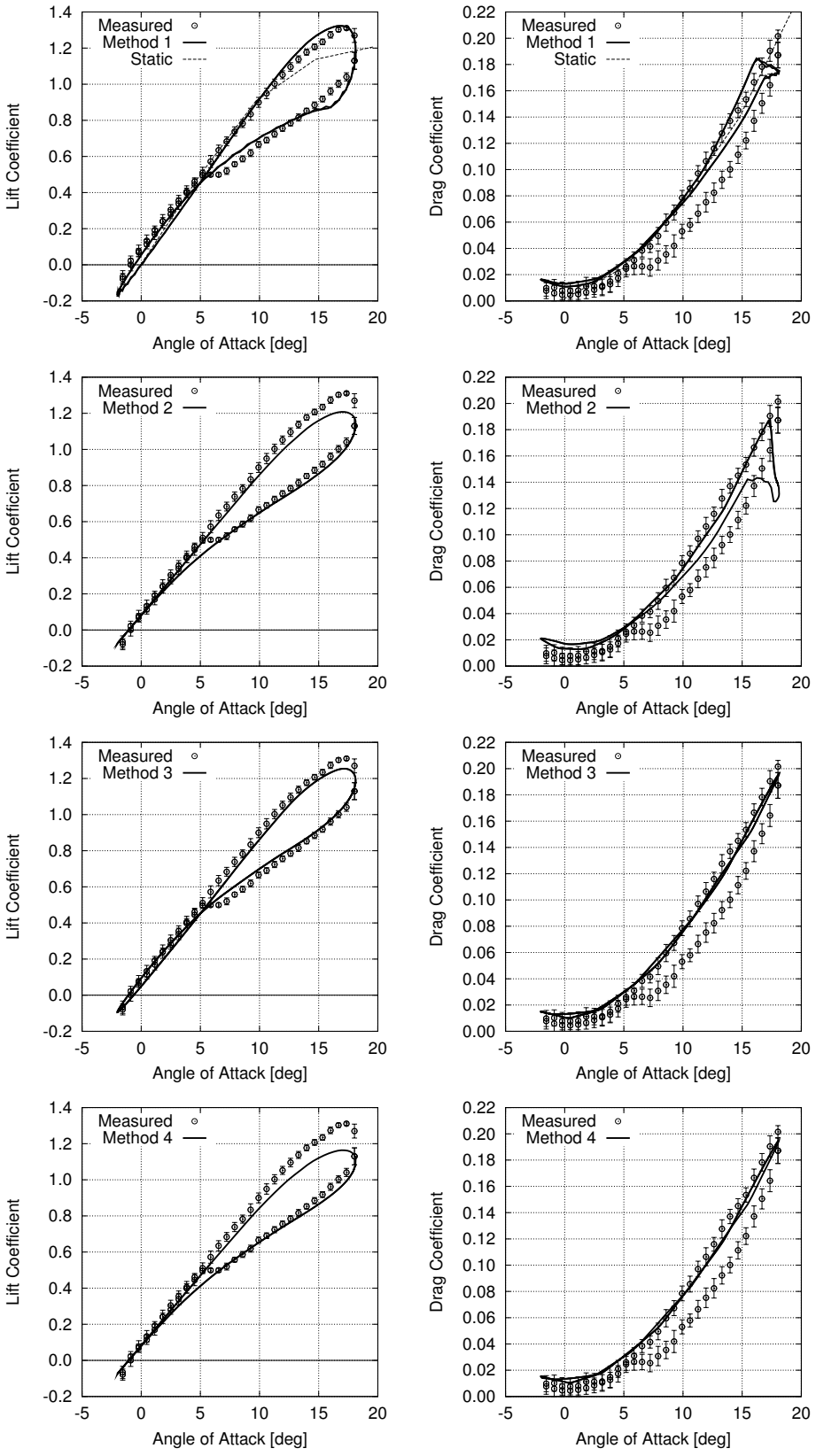

Figure 4.5: Lift and drag coefficients on pitching wing: measured data vs numerical predictions by Methods 1-4 (from top to bottom)

4.2.2 Horizontal axis wind turbine

This section addresses the aeroelastic analysis of a wind turbine rotor. For this application, the proposed Beddoes-Leishman aerodynamic model is coupled with the nonlinear, integro-differential formulation governing structural dynamics of bending-torsional blades subject to moderate deformations described in Section 3.1.3.1. The resulting aeroelastic differential system is integrated through the Galerkin approach and the computational efficiency technique (described in Section 3.1.3.1) for spatial integration of additional aerodynamic states related to wake vorticity and dynamic stall is adopted. Time-marching solution algorithm is applied fro evaluating responses to arbitrary inputs. The aeroelastic analysis is carried out on the NREL Phase VI wind turbine rotor in axial flow conditions [45]. It is a $10.58m$ diameter, two-bladed rotor with cross sections having the shape of $S809$ airfoils starting from radial position at one quarter of the blade, and circular shape at the root region (transition from circular to non-circular sections is achieved through a conical surface, as shown in Figure 4.6). In the three-quarter radius outer region, the blades are linearly tapered, with a nonlinear distribution of twist (Figure 4.7). Further details on rotor mechanical and geometrical characteristics can be found in the works of Hand et al [45] and Giguère and Selig [46]. The following numerical simulations have been obtained considering a constant blade pitch of 3° at the tip section and null pre-cone angle.

Figure 4.6: CAD rendering of NREL wind turbine blade

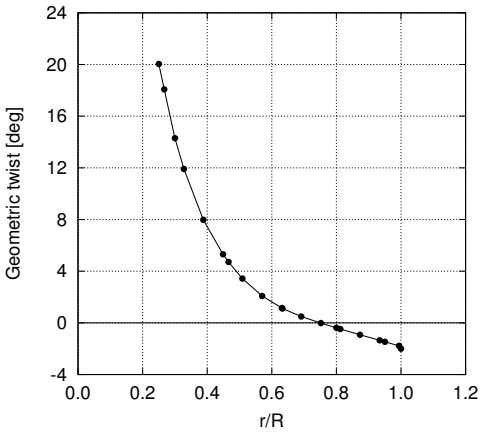

Figure 4.7: Distribution of the geometric twist along the blade

4.2.2.1 Assessment of the spectral method approach

In order to assess the numerical efficiency of the novel methodology proposed for integration of B-L model within the aeroelastic solver (Section 3.1.3.1), it is compared with a strip theory approach consisting in solving

the equations of the aerodynamic state variables at a discrete number of blade sections and then extending their values along the blade through interpolation. With this aim, firstly a convergence analysis on the order of the interpolating polynomial function used to describe the spanwise distribution of the rigid motion boundary condition is performed. Corresponding predictions of turbine performance computed by Method 1 (see Section 3.3.1) at wind speed V_w equals to 7 and $10\,m/s$ are presented in Table 4.3, which shows negligible sensitivity ($\Delta\%$) to increase of the polynomial order $n = 5$. Similarly, for the strip theory approach, Table 4.4 presents the analysis of the discrete number of blade sections on which the aerodynamic state equations are solved. Convergence values of turbine thrust and torque are obtained using 25 sections uniformly distributed along blade span.

Order of interpolating function	Thrust [N]				Torque [Nm]			
	$7\,m/s$	$\Delta\%$	$10\,m/s$	$\Delta\%$	$7\,m/s$	$\Delta\%$	$10\,m/s$	$\Delta\%$
0	1481	–	1912	–	1672	–	2916	–
1	1130	23.7	1667	12.8	828	50.4	1625	44.3
3	1115	1.32	1595	4.32	804	2.89	1465	9.85
4	1122	0.62	1566	1.82	806	0.25	1398	4.57
5	1120	0.18	1546	1.28	807	0.12	1367	2.21
6	1121	0.09	1544	0.13	808	0.12	1365	0.14

Table 4.3: Convergence analysis on the order of the interpolating function

Number of sections	Thrust [N]				Torque [Nm]			
	$7\,m/s$	$\Delta\%$	$10\,m/s$	$\Delta\%$	$7\,m/s$	$\Delta\%$	$10\,m/s$	$\Delta\%$
5	1236	–	1579	–	926	–	1598	–
10	1155	6.55	1488	5.76	819	11.5	1399	9.04
20	1133	1.90	1466	1.48	790	3.54	1339	4.29
25	1128	0.44	1461	0.34	785	0.63	1327	0.89
30	1128	0.00	1459	0.13	784	0.13	1324	0.23

Table 4.4: Convergence analysis for the strip theory approach

In the frame of preliminary design tools, computational costs are a crucial issue. The proposed aeroelastic formulation is implemented in research codes that are only partially optimized in terms of computation performance. The most expensive part of each simulation is related to BEM calculations of wake inflow and/or attached flow sectional airloads by a code that is not parallel. A free-wake computation at a single turbine operating point using blade/wake grids ensuring numerically converged results can take up to $5\,h$ on a single-CPU Intel Xeon© 2.93 GHz PC, whereas a prescribed-wake computation requires about $10\,s$. Once the input data from BEM are provided, computational time for the aeroelastic analysis is $11\,s$ on a 24-CPU Intel Xeon© 2.93 GHz PC. The comparison between the numerical performance of the novel and of the strip theory approach is summarized in Table 4.5, which highlights the greater efficiency of the novel approach both in terms of number of degrees of freedom and computational time. Regarding number of degrees of freedom reported in Table 4.5, strip theory approach involves 12 unknowns (as the number of the additional aerodynamic states of the B-L model, see Section 3.1.3) for each aerodynamic section. On the contrary, the novel technique requires, for the first nine B-L aerodynamic states, 6 DOFs to characterize the rigid motion and 1 to describe bending and torsion displacements; the last three aerodynamic states of the B-L model are analyzed with the strip theory approach

since their governing equations are piecewise continuous (see Section 3.1.3.1). Note that, as a consequence of the high values of blade stiffness characteristic provided in [45], 1 shape function is sufficient to reproduce bending and torsion displacements.

	Strip theory	Novel approach	Percentage gain
Number of DOFs	$25 \cdot 12 = 300$	$6 \cdot 9 + 1 \cdot 9 + 1 \cdot 9 + 25 \cdot 3 = 147$	51 %
Computational time	$42\,s$	$11\,s$	74 %

Table 4.5: Numerical efficiency

Next, the influence of blade elasticity on rotor performance is investigated. Turbine thrust and torque computed by Method 1, considering blade deformation effects, are compared with those evaluated under rigid-blade rotor assumption in Figure 4.8. These demonstrate that, for the case examined, blade deformations barely affect predicted rotor performance. Indeed, this is a consequence of blade stiffness characteristics provided in the work of Hand et al [45] that yield very small blade elastic deflections, as proven in Figure 4.9, where blade tip bending and torsion displacements evaluated for $5\,m/s \leq V_w \leq 25\,m/s$ are depicted.

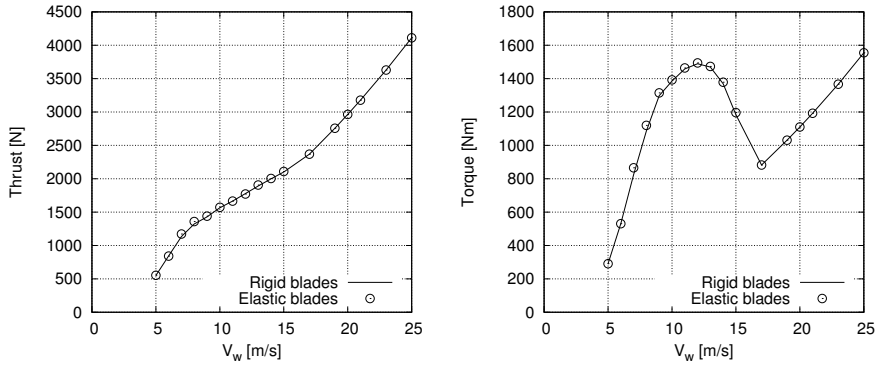

Figure 4.8: Influence of blade elasticity on predicted thrust (left) and torque (right)

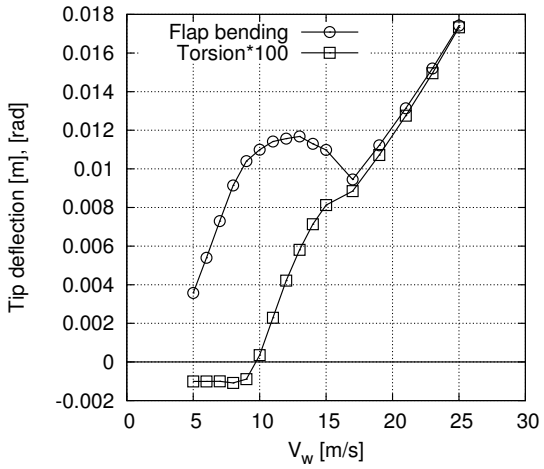

Figure 4.9: Flap bending and torsion blade tip displacements

4.2.2.2 Rotor stability analysis

Concerning the aeroelastic stability analysis, widely used techniques are based on the evaluation of the time-marching aeroelastic response to perturbations [47], or on the eigenanalysis of the aeroelastic system linearized about a steady-periodic equilibrium condition [24]. The latter is extensively applied in rotorcraft and wind turbines aeroelasticity [23], and is adopted here, as well. In order to define the eigenproblem to be solved, the contributions given by the unsteady aerodynamic BEM solver to Methods 1-4 have to be approximated in a finite-state form: this implies the determination of either a state-space representation of the (dynamic) wake inflow [48] or a state-space representation of blade loads [49]. In addition, observing that in non-axial flow configurations, the aeroelastic operator is of periodic coefficient type, once mass, damping and stiffness matrices of the linearized small-perturbation aeroelastic equations system are derived, the multiblade-variables transformation is performed, followed by constant coefficient approximation [23].

The results of the turbine stability analysis (see Section 3.1.3.1) are presented in Figures 4.10-4.12. These have been obtained by application of Method 1 (Section 3.3.1), which consists in linearizing the aeroelastic equations whilst considering a frozen wake inflow (i.e. a static wake inflow that is assumed to be independent on blade aeroelastic perturbations). Figure 4.10 presents the turbine aeroelastic eigenvalues predicted in the most critical condition, namely, that corresponding to the maximum wind speed examined, $V_w = 25\,m/s$. Stable response to perturbations is assured, as detailed by the zoom of the low-damping region illustrated in Figure 4.11. For lower wind velocities, the aeroelastic behavior of the turbine is confirmed to be stable, as shown in Figure 4.12 that concerns the eigenvalues evaluated considering $V_w = 10\,m/s$. In Figures 4.10-4.12, the zero-frequency eigenvalues are related to the additional aerodynamic states introduced by the B-L aerodynamic model, whereas the remaining ones concern the first flap, lag and torsion modes (from lower to higher frequency).

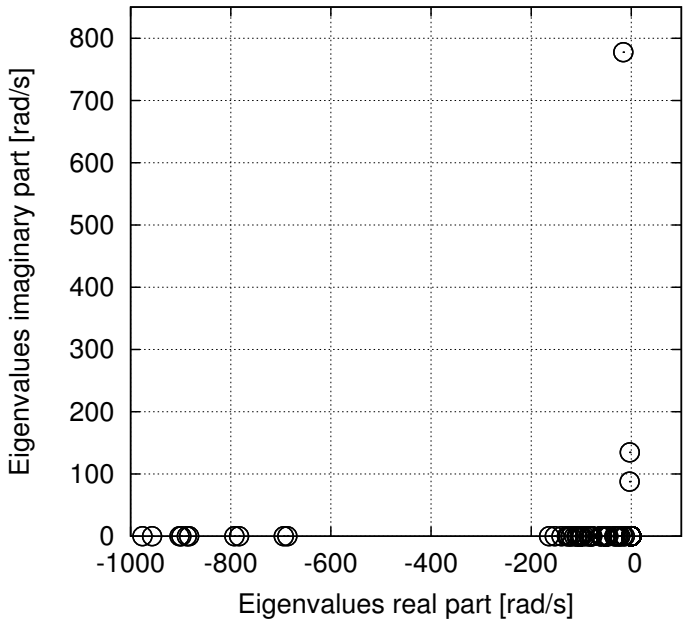

Figure 4.10: Rotor aeroelastic eigenvalues, $V_w = 25\,m/s$

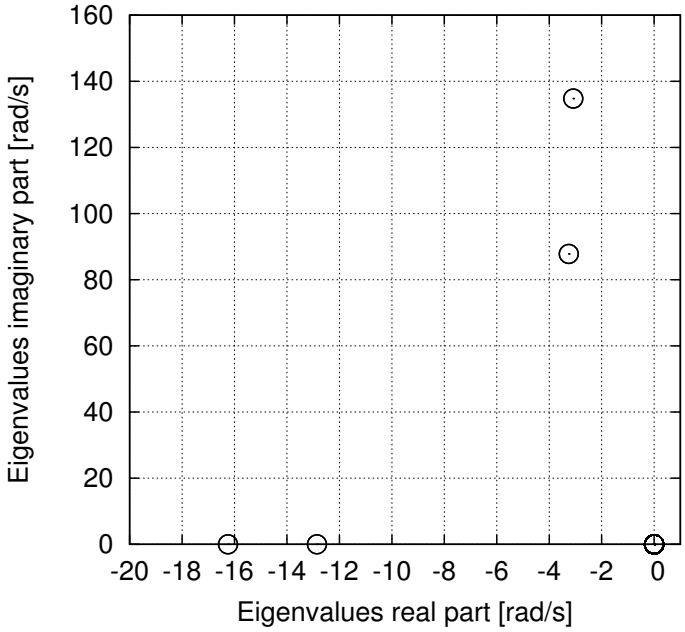

Figure 4.11: Low-damping aeroelastic eigenvalues, $V_w = 25\,m/s$

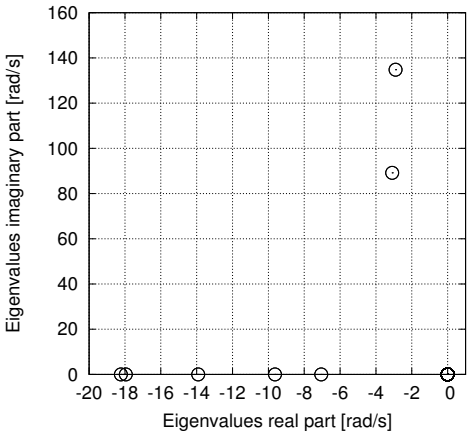

Figure 4.12: Rotor aeroelastic eigenvalues, $V_w = 10\,m/s$

4.2.2.3 Rotor response analysis

Time marching response of the complete, nonlinear aeroelastic system to perturbations is addressed in this section. This mode of solution, in addition to the harmonic balance one, is of fundamental interest in that capable of investigating operating conditions different from periodic rotor response (like, for instance, those occurring in the presence of arbitrary gust or non-uniform wind distribution). Akin to the previous section, these computations have been performed by application of Method 1, under the assumption of static-inflow. For wind speed equal to $10\,m/s$, Figure 4.13 presents the turbine response to a perturbation of blade flap bending degree of freedom in terms of the first additional aerodynamic state, which is governed by a first-order

dynamics. Its rigid component, uncoupled with structural dynamics and forced by rigid-blade local angle of attack, shows, as expected, a first-order behavior, whereas the bending component, because of blade stiffness, has a free dynamics with a damped oscillatory response.

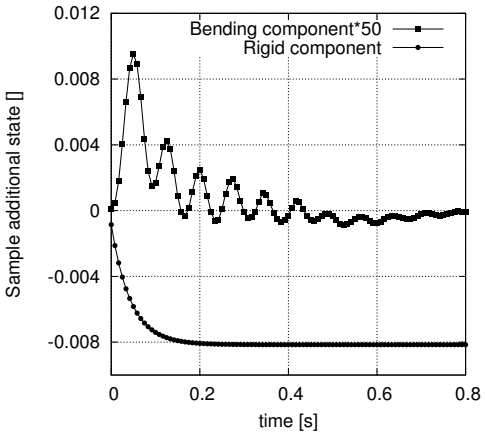

Figure 4.13: Bending and rigid components time marching solution for additional aerodynamic state x_1

The application of the logarithmic decrement rule to these time signals allows the identification of the damping coefficient that can be compared with the one determined through the eigenvalue analysis of the linearized system. Table 4.6 compares the perturbed response dynamics of rigid and bending components of state x_1 as determined from the eigenanalysis (Figure 4.12) and from the time marching solution. Although not coincident, these appears to be in good agreement. Increasing discrepancies amongst the two methodologies arise when blade stiffness is reduced to 40% of the design value. In fact, under this condition, the use of a time marching approach is mandatory to describe occurring relevant structural and aerodynamic nonlinearities.

x_1 component	Blade stiffness	Eigenvalues analysis		Logarithmic decrement rule		Perc. errors	
		Freq (rad/s)	Damp (rad/s)	Freq (rad/s)	Damp (rad/s)	ϵ_ω%	ϵ_α%
Bending	NREL	$\omega = 89.12$	$\alpha = 3.09$	$\omega = 87.8$	$\alpha = 3.16$	-1.48	$+2.26$
	40% NREL	$\omega = 63.3$	$\alpha = 3.24$	$\omega = 54.6$	$\alpha = 3.96$	-13.7	$+22.2$
Rigid	NREL	$\omega = 0.0$	$\alpha = 7.01$	$\omega = 0.0$	$\alpha = 7.23$	/	$+3.13$
	40% NREL	$\omega = 0.0$	$\alpha = 3.81$	$\omega = 0.0$	$\alpha = 4.14$	/	$+8.66$

Table 4.6: Frequency and damping associated to x_1 aeroelastic response to flap bending perturbation

4.2.2.4 Rotor performance prediction

The four proposed methods for rotor aerodynamic simulation are finally used to predict wind turbine blade airloads at the steady equilibrium condition. A crucial issue when the BEM solver is introduced to adapt airfoil theories to wind turbine aerodynamics applications is the definition of the range of wind speed in which it can be conveniently used to provide accurate corrections of 2D predictions. Indeed, as the wind speed increases, larger portions of the blade start experiencing massive flow separations, with BEM predictions providing overestimated airloads and non-physical high values of induced velocity. Literature CFD analyses of this test case [50] show that at low wind speed ($V_w = 5 - 7\,m/s$) the flow over the blade is attached except for the region closer to the root, whilst at the stall onset condition ($V_w = 10\,m/s$) separation occurs close to mid span at leading edge, and at mid

chord up to 90% of the blade span. Thus, massive flow separation is not present yet ([50], [51]). At $V_w = 13\,m/s$ (stall condition), the separation starting at $r/R = 0.47$, gradually extends over 60% of blade span, progressively leading to deep stall conditions ($V_w = 20 - 25\,m/s$). In the present analysis, BEM correction is applied at those sections where an angle of attack not higher than 20° occurs (this is considered as the threshold bounding fully separated flow region). This value corresponds to the mean distribution of estimated effective sectional angle of attack at $V_w = 13\,m/s$ [52]. Both Viterna-Corrigan and centrifugal pumping global corrections are turned off. Figure 4.14 shows spanwise distribution of normal (C_N) and tangential (C_T) blade section force coefficients for $V_w = 7\,m/s$ (top) and $V_w = 10\,m/s$ (bottom). The following definitions are used: $C_N = 2N/\rho V^2 c$ and $C_T = 2T/\rho V^2 c$, where N and T are normal and tangential section forces, whilst ρ denotes air density. Results obtained by Methods 1–4 are compared with experimental data provided by pressure transducers placed along the chord of five representative blade sections [51]. Predictions by the BEM solver are included as baseline data. Figure 4.14 (top) shows that Method 2 provides results that have a good level of accuracy. In particular, it improves BEM results at inner sections, where flow separation starts arising ($0.3 < r/R < 0.47$). Methods 1 and 3 tend to slightly underestimate section airloads over a wide blade portion, whereas Method 4 yields an overall underprediction of loads. Note that, only when C_N and C_T associated to attached flow are provided directly by the BEM solver (Methods 2 and 4), they tend towards zero at blade tip, whilst, for Methods 1 and 3, the inclusion of rotor wake inflow is not sufficient to correctly predict this behavior (Section 3.3.1). Differently, at blade root, the presence of the hub and of the cylindrical region yields non-zero values of local airloads. At $V_w = 10\,m/s$, Figure 4.14 (bottom) shows increasing discrepancies between numerical predictions and experimental data (particularly those concerning C_N). As reported in [51], at this wind speed, blade flow is extremely unstable, right at the onset of stall. Nevertheless, satisfactory airloads predictions at blade sections characterized by null or limited flow separation ($r/R \geq 0.63$) are provided by Method 2, whilst the BEM solver tends to overestimate loads.

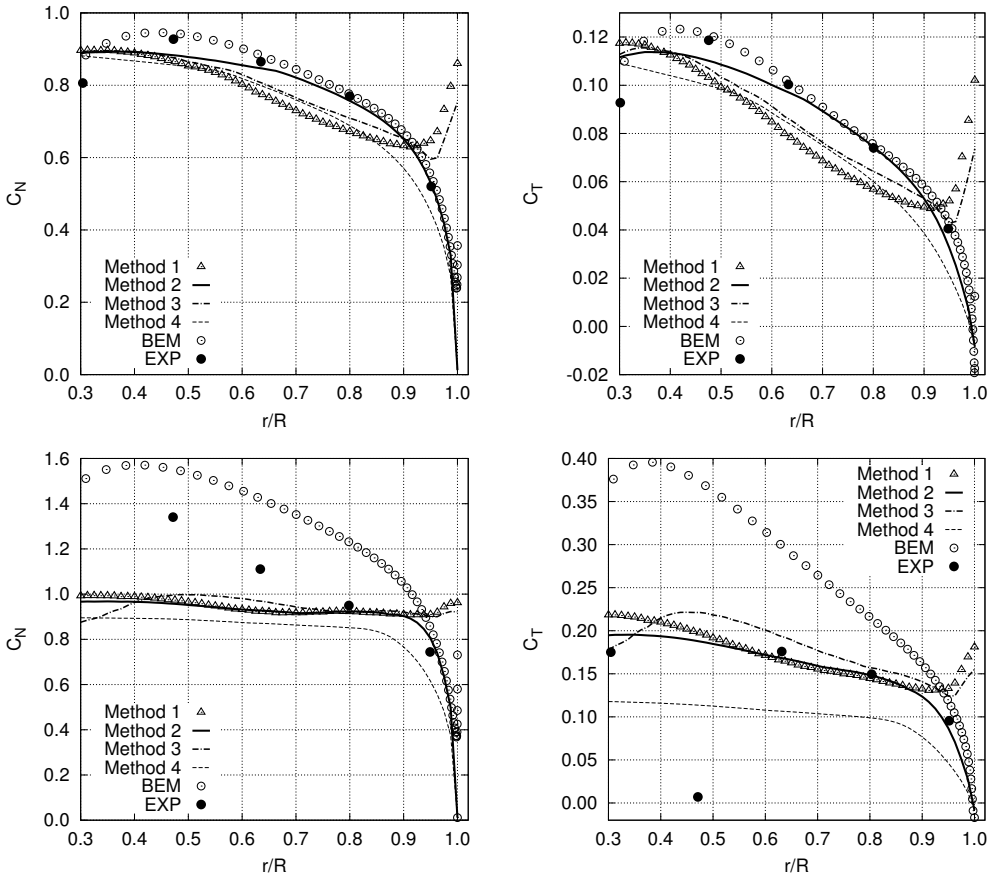

Figure 4.14: Section force coefficients for $V_w = 7\,m/s$ (top) and $V_w = 10\,m/s$ (bottom)

Further, the accuracy of wind turbine global loads predictions is examined in Figure 4.15 (top), which compares turbine thrust and power evaluated by the four methods proposed (still without centrifugal pumping and Viterna-Corrigan corrections) with experimental measurements. Fully potential-flow simulations by the BEM solver are included as well. For $V_w = 10\,m/s$, Methods 1, 2 and 3 provide results of satisfactory quality whilst, above this critical wind speed, increasing underestimation of thrust and overestimation of power are observed. The worst results are from Method 4, which yields underestimation of loads throughout the considered wind speed range. As expected, BEM results are of good accuracy up to wind speed for which flow separation region is of very limited extent ($V_w = 7\,m/s$). In order to improve the quality of simulations at high wind speeds, aerodynamic Methods 1–4 are applied at those sections where the angle of attack is lower than 20°, whereas airloads are determined through flat-plate formulas modified with Snel centrifugal pumping correction elsewhere (note that for $V_w = 17\,m/s$, all blade sections experience angle of attack greater than 20°). Figure 4.15 (bottom) shows that predictions based on the combination of Methods 1, 2 and 3 with high-angle-of-attack formulations are in good agreement with measurements, with the best power predictions given by Method 2. Still, results based on Method 4 provide underestimated values of thrust and power.

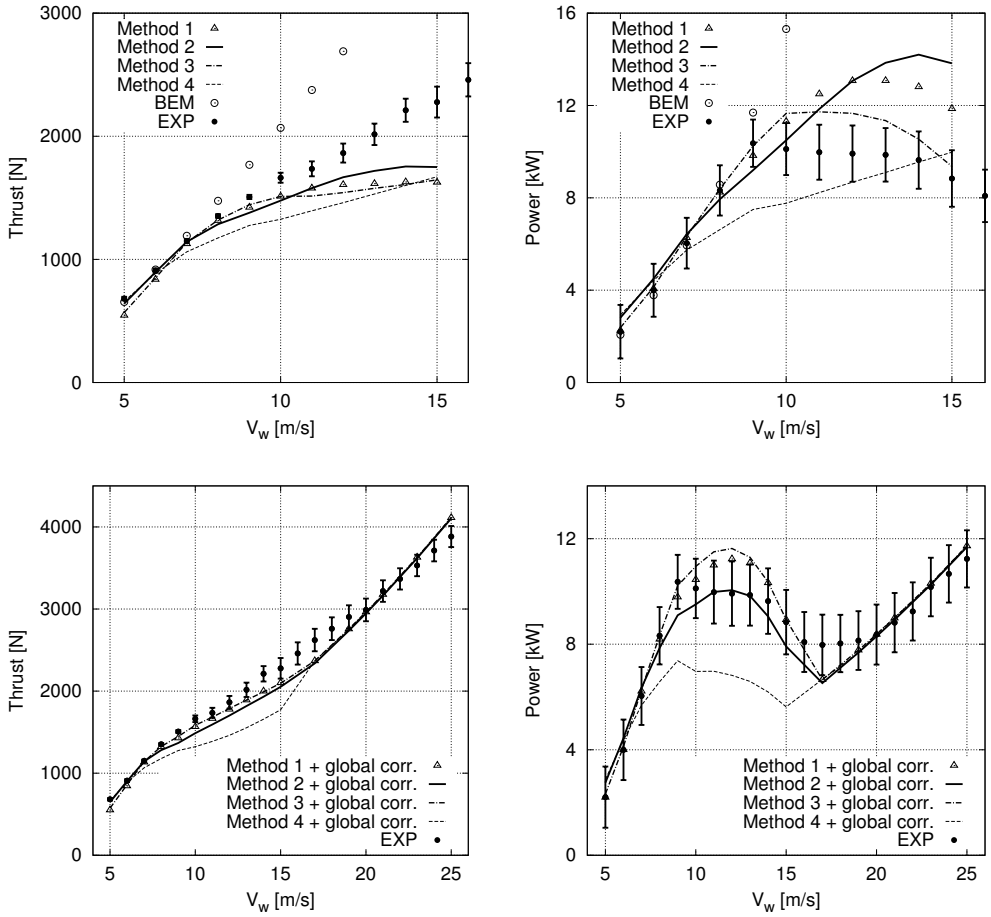

Figure 4.15: Turbine thrust (left) and power (right) predictions without (top) and with (bottom) high-angle-of-attack corrections

In order to assess the accuracy of the proposed approach with respect to state-of-art BEMT codes, the widely-used $FAST^{©}$ numerical tool is used here as a benchmark. An overview of $FAST^{©}$ aeroelastic modelling is provided in the work of Jonkman [53]. It is worth noting that rotor aerodynamics modelling is based on the same formulation used in Method 1 of the present work, with the only difference that wake induced inflow is provided here by a BEM solver, whilst $FAST^{©}$ uses a standard BEMT approach. Figure 4.16 shows that Method 2 (which has been demonstrated to be the most accurate amongst those proposed) provides power predictions that are comparable with $FAST^{©}$ outcomes up to $V_w = 17\,m/s$, whilst above this condition, Method 2 is better correlated to experimental data.

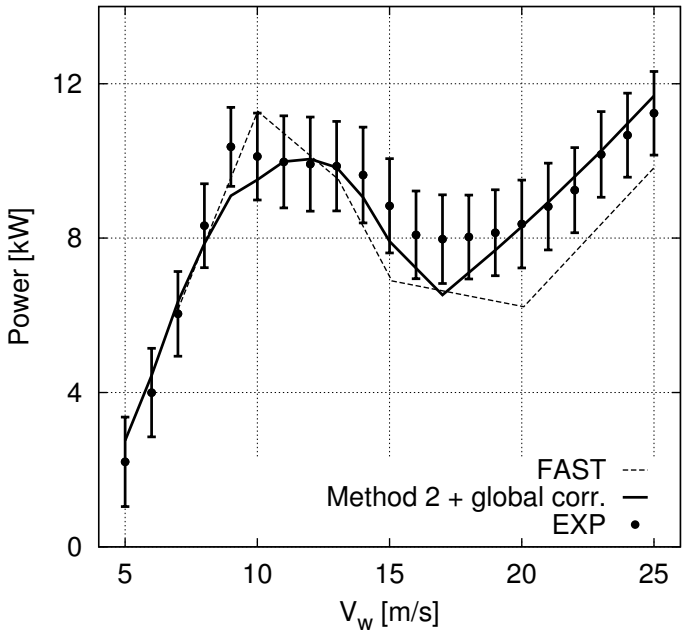

Figure 4.16: Turbine power: predictions by Method 2 compared with $FAST^{©}$ results

4.3 FEM solver validation

The developed FEM aeroelastic tool is herein validated through comparison with analytical, numerical and experimental data. Due to similarities between helicopter and wind turbine rotor blades, applications firstly concern structural and aeroelastic analyses of helicopter rotors in hovering and forward flight, then blade response and performance of a wind turbine rotor are addressed. The numerical time-marching solution of the large set of differential equations obtained by the FEM discretization of the present nonlinear aeroelastic problem is a very complex task. In the present section, first these numerical issues and the proposed solutions are analyzed. Then the application of the present FEM model to the analysis of helicopter and wind turbine rotors is discussed.

4.3.1 Numerical issues of time integration algorithms

A widely used technique for solving systems of Ordinary Differential Equations is the time marching approach. Nevertheless, numerical instabilities in the computed solution have been found in the analysis of scattering problems [54, 55] or analyzing stiff systems [**?**, 56]. In the framework of FEM-based problems, a well known numerical issue that arises in the solution of a set of ODEs to be solved through a time marching algorithm is due to the forcing terms that appear in the equations and are nonlinear function of the system unknowns. These terms should be, in principle, computed at the actual step of the integration. Using the implicit Newmark-β or Crank-Nicolson scheme, a widely used technique relies on the evaluation of these terms at the previous step of the iteration. Nevertheless, if the nonlinear forcing terms are relevant, through this kind of approach numerical errors can propagate from step to step and accumulate as the number of steps increases. This causes exponentially growing high frequency oscillations of the solution that yields to numerical instability (see Figure

4.17, in which the aeroelastic solution has been obtained through the Crank-Nicolson scheme). The approach used in the present work to overcome these issues is to use a higher order time integration scheme (Runge-Kutta) and to minimize the nonlinear content of the forcing terms by linearizing the differential system of equations as much as possible.

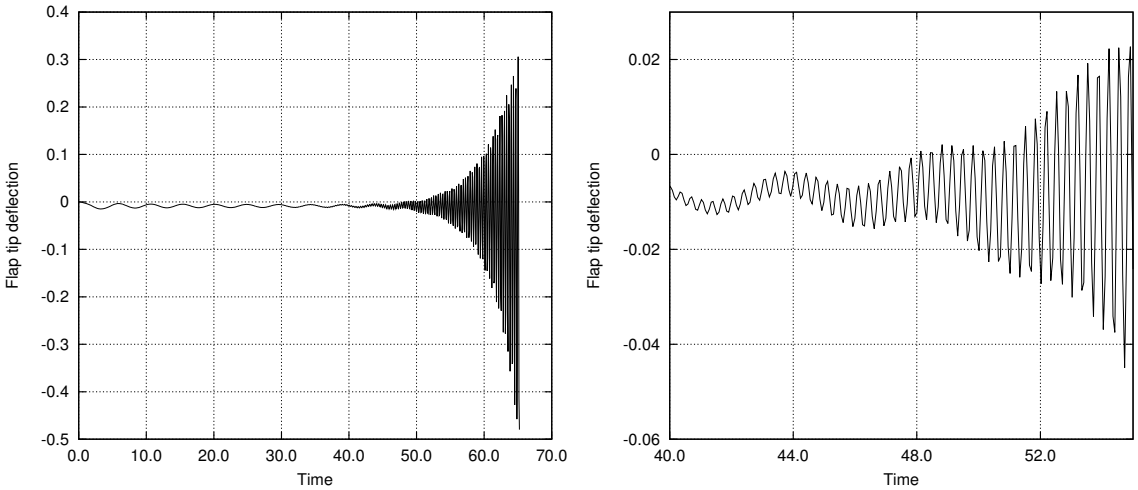

Figure 4.17: Typical numerical instability of a time marching solution, zoom is highlighted on the right)

Different time marching algorithm have been used in this work. Among the proposed methods, the Runge-Kutta algorithm is the most accurate one and doesn't present numerical instabilities. Furthermore, due to its higher order accuracy, the number of time steps per revolution (and, consequently, the computational costs) can be significantly reduced with respect to other integration methods.

The Newmark-β algorithm (see Appendix B.2) provides the solution of the aeroelastic system without the necessity of transforming it into the normal form. However, this kind of time integration algorithm shows numerical problems when the set of ODEs to be solved consists of second order and first order ones. In particular, for the present aeroelastic formulation, this happens when blade aerodynamics is modeled through the Beddoes-Leishman theory. In fact, the additional aerodynamic states introduced by this approach are governed by first order ODEs. The solution of this mixed set of ODEs through the Newmark-β algorithm shows an unphysical high frequency oscillation that can be avoided by introducing a combined solution scheme (see Appendix B.4) in which the second order ODEs are solved through the Newmark-β algorithm whereas the first order ones are solved by Crank-Nicolson (see Figure 4.18).

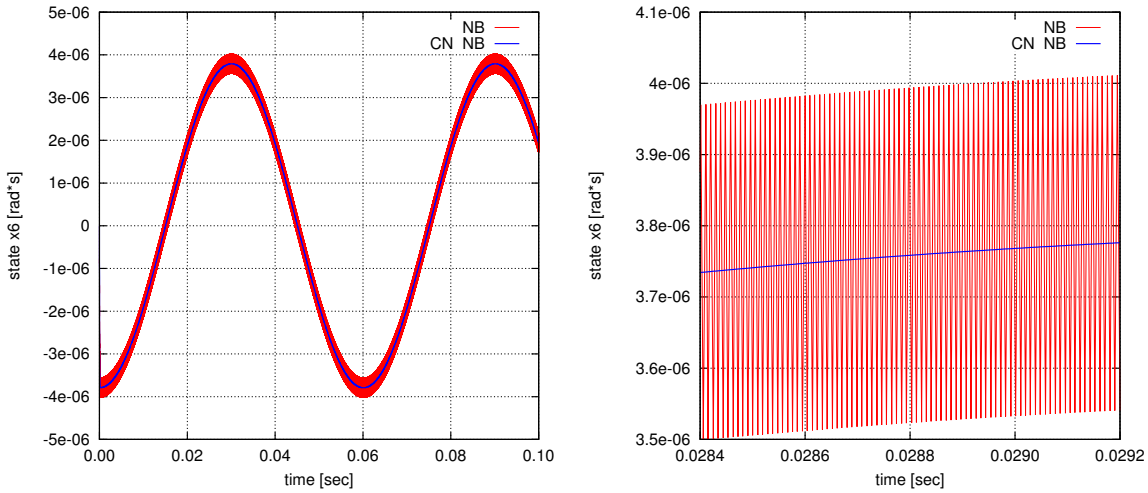

Figure 4.18: Comparison of the solution of an additional B-L aerodynamic state, zoom is highlighted on the right

To avoid numerical instabilities due to nonlinearities of the aeroelastic problem, integration of the linearized system in equation (B.1) can be performed. First the global force vector is decomposed into structural and aerodynamic contributions as follows:

$$\mathbf{F} = \mathbf{F}_c^{str} + \mathbf{F}_{Nl}^{str}(\mathbf{q}) + \mathbf{F}_{Nli}^{str}(\dot{\mathbf{q}}) + \mathbf{F}_c^{aer} + \mathbf{F}_l^{aer}(\mathbf{q}, \dot{\mathbf{q}}, \ddot{\mathbf{q}}) + \mathbf{F}_{Nl}^{aer}(\mathbf{q}, \dot{\mathbf{q}}) \tag{4.2}$$

where $\mathbf{F}_c^{str}$ and $\mathbf{F}_{Nl}^{str}$ are vectors retaining constant (i.e. independent on system degrees of freedom) and nonlinear structural forcing terms, respectively, whilst $\mathbf{F}_{Nli}^{str}$ contains nonlinear double integral structural terms [19]. If the analytical expressions of aerodynamic terms as a function of system unknowns are available, the aerodynamic force vector can also be decomposed into a constant part ($\mathbf{F}_c^{aer}$), a linear ($\mathbf{F}_l^{aer}$) and nonlinear ($\mathbf{F}_{Nl}^{aer}$) contribution. Aerodynamic linear terms are added to the structural ones on the left hand side of the equation. In details, they can be written in the following matricial form:

$$\mathbf{F}_l^{aer} = \mathbf{M}^{aer}\ddot{\mathbf{q}} + \mathbf{C}^{aer}\dot{\mathbf{q}} + \mathbf{K}^{aer}\mathbf{q} \tag{4.3}$$

Instead, a first order approximation of the Taylor series is applied to nonlinear contributions:

$$\begin{aligned} \mathbf{F}_{Nl}^{str} &= \mathbf{F}_{Nl}^{str}|_{\mathbf{q}_e} + \mathbf{K}_t^{str}|_{\mathbf{q}_e}(\mathbf{q} - \mathbf{q}_e) \\ \mathbf{F}_{Nli}^{str} &= \mathbf{F}_{Nli}^{str}|_{\mathbf{q}_e} + \mathbf{C}_t^{str}|_{\mathbf{q}_e}(\dot{\mathbf{q}} - \dot{\mathbf{q}}_e) \\ \mathbf{F}_{Nl}^{aer} &= \mathbf{F}_{Nl}^{aer}|_{\mathbf{q}_e} + \mathbf{K}_t^{aer}|_{\mathbf{q}_e}(\mathbf{q} - \mathbf{q}_e) + \mathbf{C}_t^{aer}|_{\mathbf{q}_e}(\dot{\mathbf{q}} - \dot{\mathbf{q}}_e) \end{aligned} \tag{4.4}$$

in which $\mathbf{K}_t$ and $\mathbf{C}_t$ represent Jacobian matrices that contribute to the stiffness and damping matrix of the aeroelastic system, whilst $\mathbf{q}_e$ is the steady equilibrium solution. Note that, in equation (4.4) $\dot{\mathbf{q}}_e = 0$. Finally, substituting equations (4.3) and (4.4) into equation (B.1) yields the following aeroelastic system to be integrated:

$$\mathbf{M}^{tot}\ddot{\mathbf{q}} + \mathbf{C}^{tot}\dot{\mathbf{q}} + \mathbf{K}^{tot}\mathbf{q} = \mathbf{F}^{tot} \tag{4.5}$$

where

$$\begin{aligned}
\mathbf{M}^{tot} &= \mathbf{M} - \mathbf{M}^{aer} \\
\mathbf{C}^{tot} &= \mathbf{C} - \mathbf{C}^{aer} - \mathbf{C}_t^{str}|_{\mathbf{q}_e} - \mathbf{C}_t^{aer}|_{\mathbf{q}_e} \\
\mathbf{K}^{tot} &= \mathbf{K} - \mathbf{K}^{aer} - \mathbf{K}_t^{str}|_{\mathbf{q}_e} - \mathbf{K}_t^{aer}|_{\mathbf{q}_e} \\
\mathbf{F}^{tot} &= \mathbf{F}_c^{str} + \mathbf{F}_c^{aer} + \mathbf{F}_{Nl}^{str}|_{\mathbf{q}_e} + \mathbf{F}_{Nli}^{str}|_{\mathbf{q}_e} + \mathbf{F}_{Nl}^{aer}|_{\mathbf{q}_e} - \mathbf{K}_t^{str}|_{\mathbf{q}_e}\mathbf{q}_e - \mathbf{K}_t^{aer}|_{\mathbf{q}_e}\mathbf{q}_e
\end{aligned} \tag{4.6}$$

The steady equilibrium solution is obtained applying Newton-Raphson scheme to the following system

$$\mathbf{K}^{tot}\mathbf{q}_e = \mathbf{F}^{tot}\left(\mathbf{q}_e\right) \tag{4.7}$$

The solution of large number of finite element equations for blade response is a computationally expensive task due to the number of degrees of freedom. In order to reduce computational costs and avoid numerical problems related to undamped high frequency degrees of freedom, a suitable reduction of the number of unknowns of the problem is achieved by transforming the aeroelastic equations (B.1) into the modal space using a set of modal functions as follows:

$$\left[\Phi^T\mathbf{M}\Phi\right]\left[\Phi^T\ddot{\mathbf{q}}\right] + \left[\Phi^T\mathbf{C}\Phi\right]\left[\Phi^T\dot{\mathbf{q}}\right] + \left[\Phi^T\mathbf{K}\Phi\right]\left[\Phi^T\mathbf{q}\right] = \left[\Phi^T\mathbf{F}\right] \tag{4.8}$$

where Φ is the matrix collecting natural modes. The final equations of motion in the modal space can be written as

$$\mathbf{M}_\Phi\ddot{\mathbf{q}}_\Phi + \mathbf{C}_\Phi\dot{\mathbf{q}}_\Phi + \mathbf{K}_\Phi\mathbf{q}_\Phi = \mathbf{F}_\Phi \tag{4.9}$$

The actual nodal deflections $\mathbf{q}$ can be obtained from normal mode coordinates $\mathbf{q}_\Phi$ using the transformation:

$$\mathbf{q} = \Phi\mathbf{q}_\Phi \tag{4.10}$$

Finally, to avoid numerical instabilities in undamped aeroelastic systems analyzed, dissipation of energy due to material damping has been also considered assuming a material with a linear visco-elastic behavior, the stresses in equation 2.13 must be modified with a new contribution that is a linear function of the strain rates:

$$\begin{aligned}
\sigma_{xx} &= E^*\dot{\epsilon}_{xx} \\
\sigma_{x\eta} &= G^*\dot{\epsilon}_{x\eta} \\
\sigma_{x\zeta} &= G^*\dot{\epsilon}_{x\zeta}
\end{aligned} \tag{4.11}$$

where E^* and G^* are coefficients which take into account internal damping of the material in tension and shear, respectively. Thus, the virtual work of the structural dissipative forces for the $b-th$ blade is

$$\delta W_{Db} = \int_0^R \iint_A \left(E^*\dot{\epsilon}_{xx}\delta\epsilon_{xx} + G^*\dot{\epsilon}_{x\eta}\delta\epsilon_{x\eta} + G^*\dot{\epsilon}_{x\zeta}\delta\epsilon_{x\zeta}\right) d\eta d\zeta\, dx \tag{4.12}$$

in which only the direct linear damping terms associated with the dependent variables are retained. Substituting equations (2.15), (2.16) and (2.17) into equation (4.12), integrating over the cross section, and retaining only linear direct damping terms leads to:

$$\delta W_{Db} = \int_0^R \left(d_1\delta u' + d_2\delta\phi'' + d_3\delta\phi' + d_4\delta v'' + d_5\delta w'' + d_6\delta\phi'\right) dx \tag{4.13}$$

where

$$\begin{aligned} d_1 &= E^* A \dot{u}' \\ d_2 &= E^* C_1 \dot{\phi}'' \\ d_3 &= E^* B_1 \theta_{pt}'^2 \dot{\phi}' \\ d_4 &= E^* \left(I_{\zeta\zeta} cos^2\theta + I_{\eta\eta} sin^2\theta \right) \dot{v}'' \\ d_5 &= E^* \left(I_{\zeta\zeta} sin^2\theta + I_{\eta\eta} cos^2\theta \right) \dot{w}'' \\ d_6 &= G^* J \dot{\phi}' \end{aligned} \tag{4.14}$$

These contributions are added to the gyroscopic matrix of equation (2.47) to obtain the total damping matrix of the aeroelastic system.

4.3.2 Helicopter rotor structural analysis

A non rotating Bernoulli-type linear beam clamped at root and undergoing uncoupled elastic twist, flap and lag deformation is considered first. Beam structural and geometric properties are summarized in Table 4.7 (left). Beam eigenfrequencies are presented in Table 4.7 (right) showing good correlation of FEM predictions with analytical results.

Geometric & Structural properties	
Length	$5.029\,m$
Lag bending stiffness	$8 \cdot 10^5\,Nm^2$
Flap bending stiffness	$6 \cdot 10^5\,Nm^2$
Torsion stiffness	$1 \cdot 10^6\,Nm^2$

Beam eigenfrequencies $[rad/s]$		
	Analytical	FEM
I lag	87.91	87.92
II lag	551.01	551.02
III lag	1542.97	1542.96
I flap	32.10	32.10
II flap	201.19	201.20
III flap	563.41	563.40
I torsion	321.56	321.56
II torsion	964.69	964.69
III torsion	1607.82	1607.90

Table 4.7: Non-rotating beam: geometric and structural properties (left), predicted eigenfrequencies compared to analytical results (right)

The same level of accuracy of numerical results is shown in Table 4.8 for the two-bladed hingeless rotor experimentally tested in [57]. The comparison is performed for a torsionally soft rotor with zero precone, droop and collective pitch, considering both a soft and a stiff flexure.

Non-rotating blade natural frequencies $[Hz]$				
	Soft Flexure		Stiff Flexure	
	Exp	FEM	Exp	FEM
I lag	22.02	22.56	23.76	23.34
I flap	5.19	5.18	5.25	5.19
II flap	32.50	32.69	32.75	32.80
I torsion	38.38	36.50	44.73	43.59

Table 4.8: Two-bladed hingeless rotor: FEM predictions compared to experimental data

Then, rotating frequencies and natural mode shapes of a four-bladed hingeless helicopter rotor in hovering are addressed. Vehicle properties are described in [27]: rotor blades are uniform with a linear pre-twist of $-8°$. A collective pitch angle of $9°$ is used to couple blade flap, lag and torsion modes. Hinge offset is modeled as a rigid element without any degree of freedom. Blades natural frequencies predicted by the present FEM model are listed in Table 4.9 showing a good level of accuracy with respect to results from the FEM approach proposed in [27]. The same high quality of numerical prediction is achieved for the first three flap and lag bending modes as well as for the first two torsion modes (see Figure 4.19).

Rotating blade natural frequencies $[Hz]$		
	FEM [27]	Present FEM model
I lag	4.71	4.63
II lag	27.95	28.00
III lag	70.67	70.44
I flap	7.38	7.42
II flap	21.71	21.59
III flap	47.98	47.78
I torsion	22.69	22.51
II torsion	66.66	66.55

Table 4.9: Four-bladed hingeless rotor: present predictions compared to data in [27]

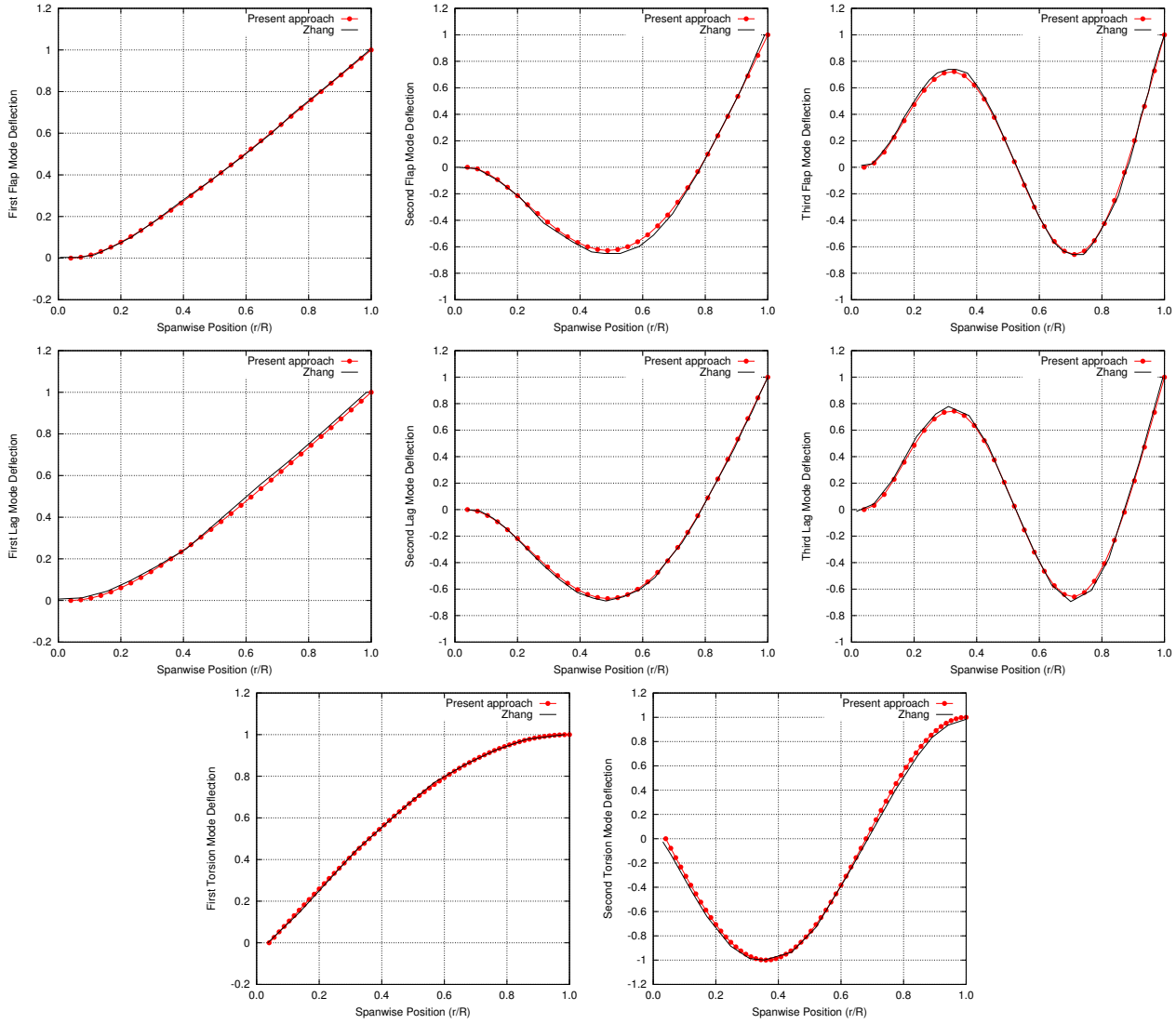

Figure 4.19: FEM predictions of blade natural modes shapes for a four-bladed hingeless helicopter rotor: present approach compared to data in [27]

4.3.3 Helicopter rotor aeroelastic analysis

4.3.3.1 Hover condition

FEM based numerical tool is then applied to the aeroelastic analysis of a two-bladed hingeless helicopter rotor in hover. Detailed description of the test case can be found in [58]: rotor blades are untwisted, without structural damping, root offset and chordwise axis offset. The blade has $NACA0012$ airfoil sections and a rectangular planform shape, and the rotor is operating at an angular velocity of $1000\,rpm$. Structural properties of the blade are found in [58]. Several values of collective pitch are considered along with two precone settings ($\beta = 0^\circ$ and $\beta = 5^\circ$). Figure 4.20 shows predicted thrust loading along blade span for $\theta = 8^\circ$ and $\beta = 0^\circ$. Nondimensional loading coefficient is herein defined as $dc_T/ds = (2dT/dr)/\rho V^2 c$, where $s = r/R$, dT denotes section elemental

thrust, ρ is the air density, V is the local total velocity and c is the section chord. First, the proposed blade aerodynamics model is validated assuming a rigid bladed rotor. For the present assessment, blade aerodynamics is based on the application of the Greenberg theory in hover condition (see Section 3.1.2.1) with the assumption of $C(k) = 1$ (quasi-steady approximation). The aerodynamic model is enhanced by the rotor wake inflow provided by a 3D BEM solver to correct blade sections downwash. This approach can suitably enhance sectional aerodynamics with respect to a simple momentum theory approach yielding numerical predictions that are in excellent agreement with BEM outcomes up to 80% of blade span. Nevertheless, the inclusion of rotor wake inflow is not sufficient to correctly predict airloads near blade tip (see [62]).

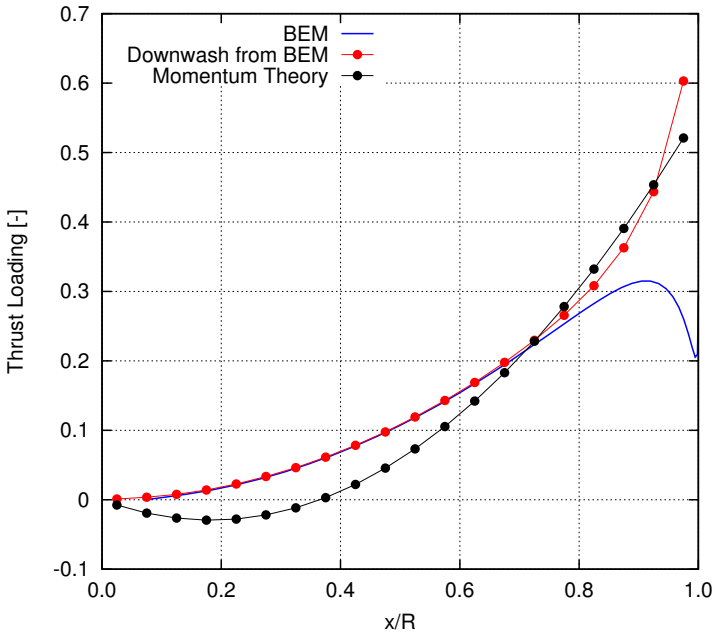

Figure 4.20: Thrust loading along span for a rigid blade ($\theta = 8^\circ$ and $\beta = 0^\circ$)

For the same rotor, blade deformations are then addressed. The present formulation is compared to the modal approach proposed in [58] where the Theodorsen theory (see Section 3.1.1) is used to describe blade sections airloads. FEM analysis is herein performed using 50 elements along blade span to ensures negligible sensitivity to further refinements. This yields an excellent agreement with numerical results in [58] in terms of thrust loading acting on a deformable blade (see Figure 4.21). The same quality of predictions is achieved for blade tip flap, lag and torsion displacements at several collective pitch settings and for $\beta = 0^\circ$ and $\beta = 5^\circ$, as shown in Figure 4.22.

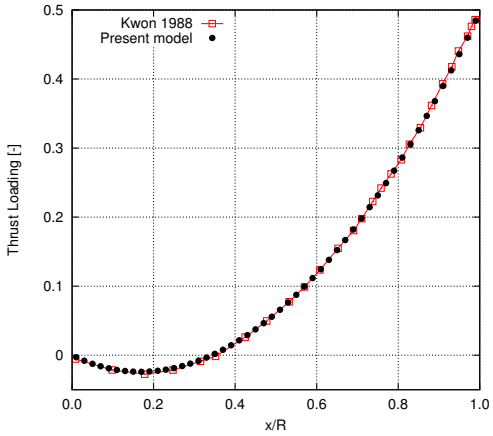

Figure 4.21: Thrust loading along span for a deformable blade ($\theta = 8°$ and $\beta = 0°$)

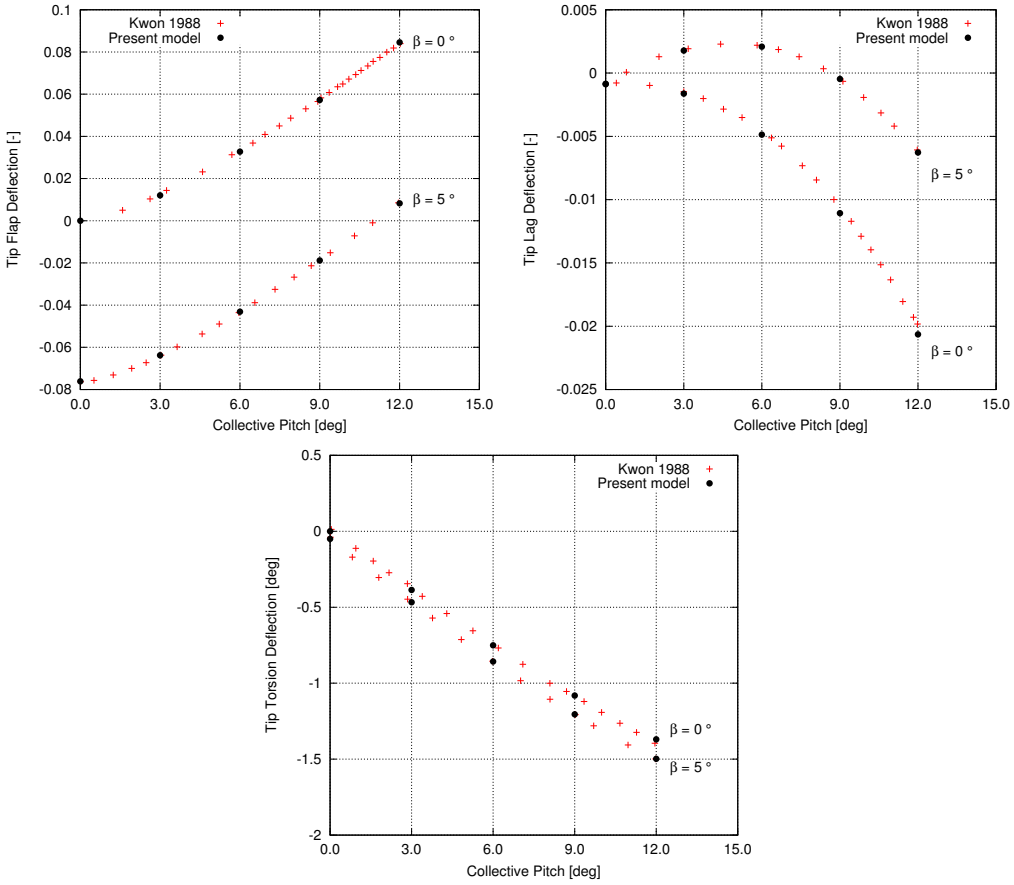

Figure 4.22: Predicted blade tip displacements for a two-bladed hingeless helicopter rotor in hover: present approach compared to data in [58]

For the following numerical simulation, integration of the linearized system is performed (see Section 4.3.1). Dealing with a rotor in hovering condition, the aeroelastic problem in equation (4.5) is characterized by constant

coefficients. The steady equilibrium solution $\mathbf{q}_e$ is computed then, the blade is perturbed by an amount equal to 10% of the equilibrium deflections and released. The unsteady blade motion under the interaction of elastic blade and applied aerodynamic loads is then computed through a time marching solution scheme based on the Newmark-β algorithm (see Section B.2). Figures 4.23, 4.24 and 4.25 show nondimensional perturbations for lag, flap and torsion at the blade collective pitch angle of 8°. Numerical predictions of the present tool are in excellent agreement with numerical data in [58].

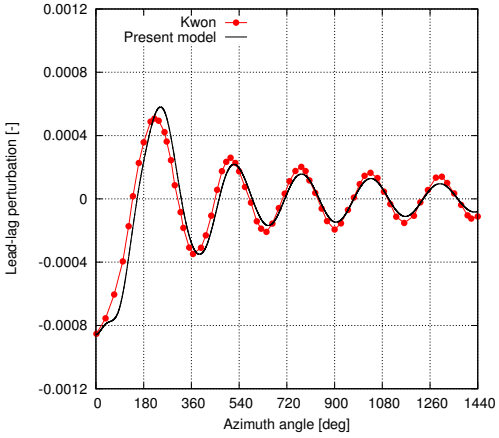

Figure 4.23: Nondimensional lag deflection perturbation time history

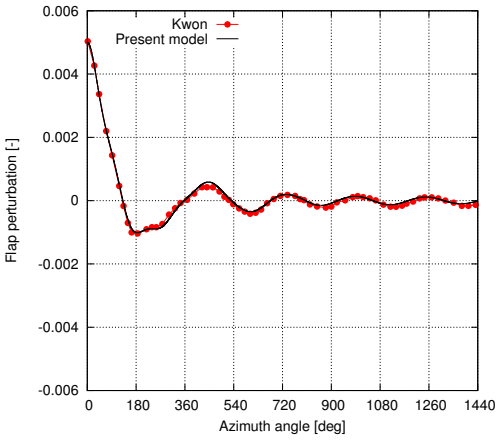

Figure 4.24: Nondimensional flap deflection perturbation time history

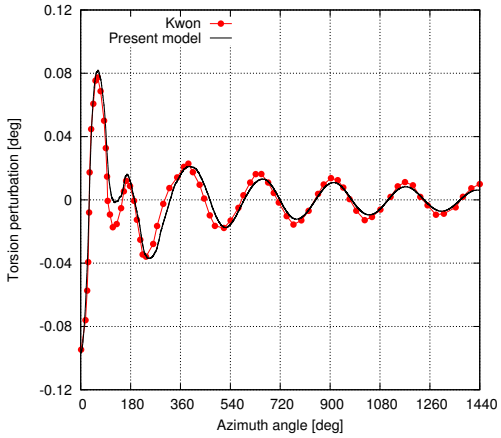

Figure 4.25: Nondimensional torsion deflection perturbation time history

An analysis of the effect of aerodynamic modelling on perturbation deflections predictions is then presented. In details predicted time evolutions of blade tip deflections in term of lag, flap and torsion are shown in Figures 4.26, 4.27 and 4.28. The quasi-steady approximation of the Greenberg theory ($C(k) = 1$) provides numerical predictions which are, as expected, very different from those provided by unsteady formulations. Results from Theodorsen theory and Beddoes-Leishman model are in good agreement and this underlines that significant flow separations don't occur for the analyzed test conditions.

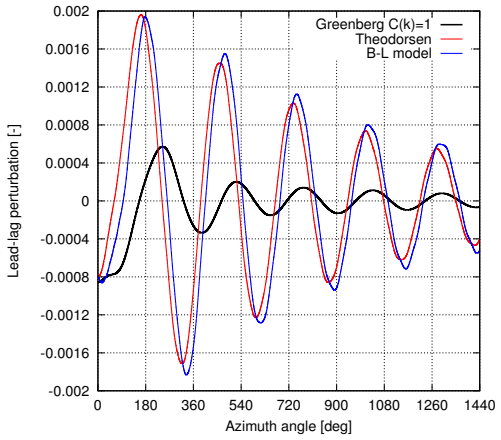

Figure 4.26: Nondimensional lag deflection perturbation time history

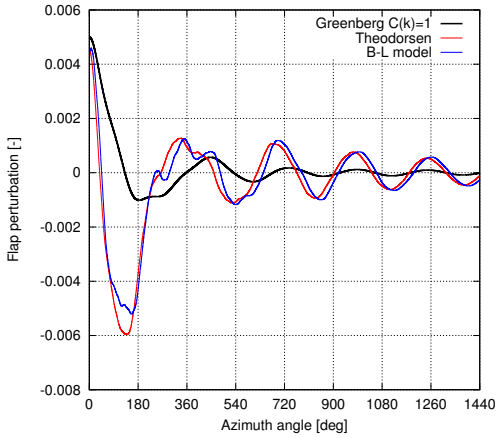

Figure 4.27: Nondimensional flap deflection perturbation time history

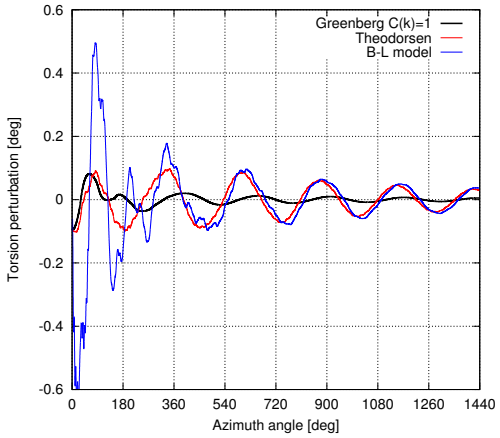

Figure 4.28: Nondimensional torsion deflection perturbation time history

4.3.3.2 Forward flight condition

The same four-bladed hingeless helicopter rotor [27] already analyzed in hover condition is then considered at different forward flight advance ratios. Quasi-steady blade element aerodynamic model (Section 3.1.1.1) with a linear variation of inflow (Drees model, Section 3.2.2) is applied. Two different advance ratios are analyzed and corresponding rotor trim controls are reported in Table 4.10.

	$\mu = 0.15$	$\mu = 0.30$
θ_0	6.83°	8.59°
θ_{1c}	1.80°	1.80°
θ_{1s}	−2.44°	−5.40°
α_s	1.22°	3.91°

Table 4.10: Trim controls

The modal reduction method is herein applied (see Section 4.3.1). In order to achieve an accurate solution

for the nodal deflections, coupled rotating normal mode shapes are used to define matrix Φ. Specifically, in the present analysis three flap, three lag and two torsion modes are considered. Figure 4.29 presents periodic time histories of blade tip deflections during a revolution for two different advance ratios ($\mu = 0.15$ and $\mu = 0.30$). For both conditions, FEM predictions are in excellent agreement with numerical data [27] in terms of lag and torsion deformations. Slight overestimation of tip flap deflection is observed, even if the general quality of numerical prediction is still good.

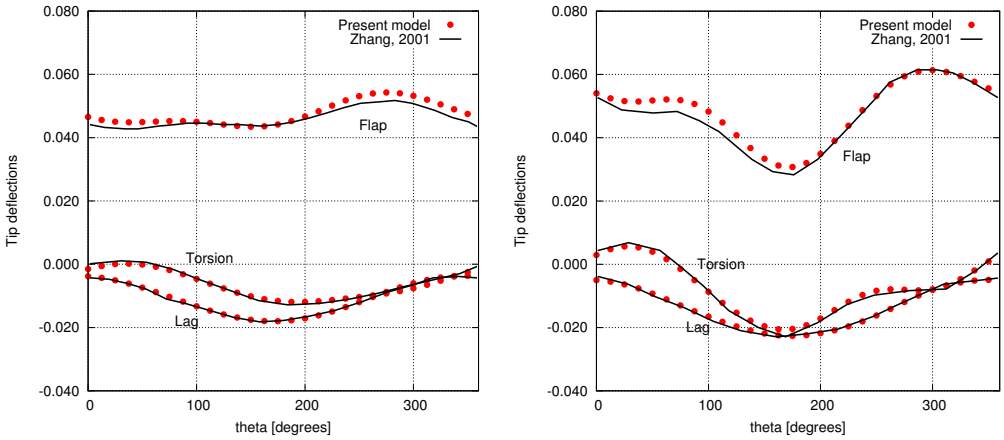

(a) $\mu = 0.15$ (b) $\mu = 0.30$

Figure 4.29: Blade tip deformations

For the same rotor, hub loads are also investigated. Figure 4.30 shows the $4/rev$ nondimensional vibratory hub loads for advance ratio $\mu = 0.30$. Predictions of the FEM solver are in good agreement with numerical data in [27].

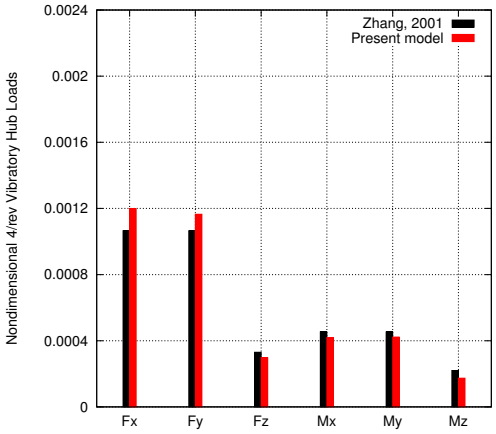

Figure 4.30: 4/rev vibratory hub loads

4.3.4 Horizontal axis wind turbine performance

The proposed FEM aeroelastic solver [59, 60] is then applied to the analysis of the NREL horizontal axis wind turbine already analyzed in Section 4.2.2.

In the present analysis, steady aerodynamics based on the Glauert theory [61] is applied with 3D correction provided by the Snel model (see Section 3.3.2.2). BEM wake inflow correction to downwash at the 3/4-chord point is considered only at those sections where an angle of attack not higher than 15° occurs (this is considered as the threshold bounding fully separated flow region). Corrections for high angles of attack regimes are not included in the model. For this test case, rotor aeroelastic calculations in Figure 4.31 show that blade stiffness characteristics [45] are such that very small blade deflections occur (see also the modal analysis in Section 4.2.2.1). In this figure, blade tip bending displacements evaluated for wind speed $5\,m/s \leq V_w \leq 19\,m/s$ are depicted (the corresponding blade tip torsion is almost zero). Results from present approach are compared to those provided by the validated modal aeroelastic solver [62] presented in Section 4.2.2.

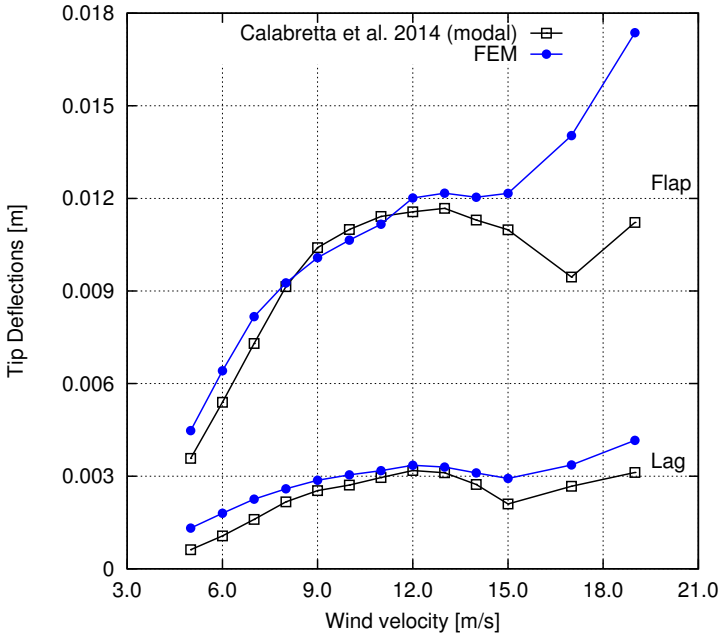

Figure 4.31: Turbine flap and lag bending blade tip displacements

Finally, the proposed aeroelastic tool is applied to evaluate wind turbine delivered thrust and power at the steady equilibrium conditions. The accuracy of wind turbine performance predictions is examined in Figure 4.32, showing that the present approach yields a satisfactory agreement with measurements in the range $5\,m/s \leq V_w \leq 17\,m/s$. In order to improve global loads predictions at high-angle-of-attack conditions, semi-empirical models, discussed in Section 3.3.2 and already validated in the numerical tool based on a spectral approach (see Section 4.2.2.4) should be included in the model.

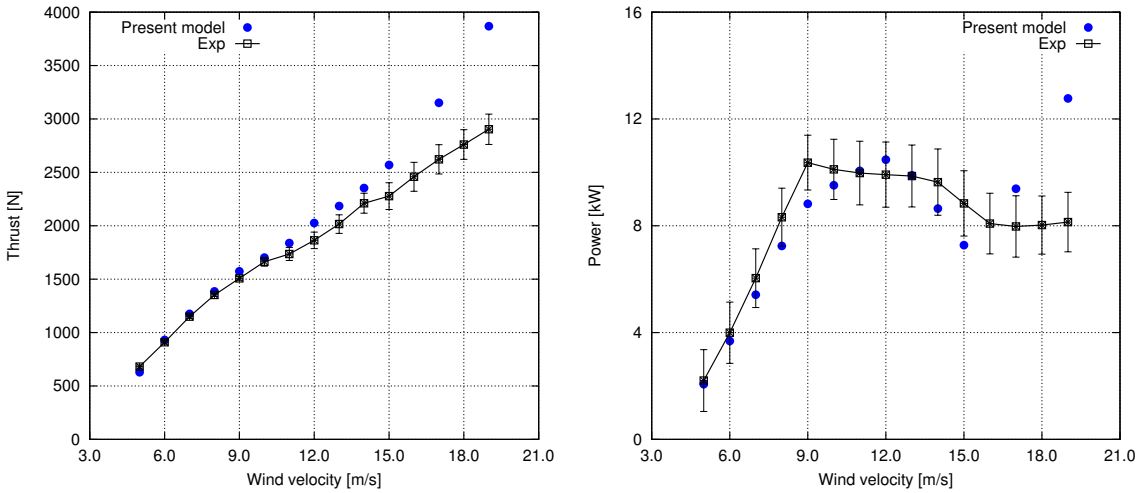

Figure 4.32: Turbine performance predictions: thrust (left) and power (right)

Chapter 5

Conclusions

Due to the large dimensions of the rotor system currently used in wind turbines plants, aeroelasticity assumes a crucial role in the design stage, where the availability of fast and accurate prediction tools is nowadays a need for engineers and researchers to accurately evaluate performance of such devices during their operational life.

These considerations have inspired the present thesis aimed at assessing a FEM-based aeroelastic formulation for the analysis of horizontal axis wind turbines in different working conditions. A key-point of this work is the choice of the more accurate aerodynamic model able to capture the main physical phenomena occurring on the blades and in the flow field surrounding them. In this context, different sectional aerodynamic theories have been analyzed and discussed; the most complete has been formulated by Beddoes-Leishman taking into account unsteady effects due to both shed vorticity and dynamic stall onset. Focusing on 2D airfoils undergoing harmonic pitch motion about the quarter chord point, the comparison with available numerical data highlights that the Beddoes-Leishman aerodynamic model is fully adequate into predict the unsteady airloads.

The inclusion of three-dimensional effects has been accomplished by coupling a 3D solver based on a Boundary Element Method for incompressible, potential flows and the B-L model; this gives four aerodynamic formulations including shed vorticity, dynamic stall, leading and trailing edge separations, as well as three dimensional wake induced effects. Numerical results carried out from these models applied on a test-case concerning an oscillating/translating 3D wing in water highlight the capability of the proposed formulations into capture the hydroloads measured during a devoted experimental campaign performed at CNR-INSEAN towing-tank. Specifically:

- The main features of unsteady wing aerodynamics and of dynamic stall phenomena, especially for lift coefficient, are well predicted.
- The inherent randomness of the flow during the reattachment phase induces significant variations of the airloads over the wing and thus, numerical simulations of the downstroke phase do not match very well experimental results. This is particularly evident in terms of drag hysteresis loop.

Next, the aeroelastic formulation based on a spectral approach has been validated through a comparison with experimental results performed on the NREL horizontal axis wind turbine. The main results are:

- Predictions given by three of the four BEM/B-L coupling strategies are of good quality up to the onset of massive stall. Results from Method 2 are the most accurate whereas those coming from Method 4 show

the poorest agreement.

- The transition from attached to separated flow conditions remains a critical issue to be modeled when dealing with performance predictions.
- Semi empirical models have been successfully applied to extend to massively separated flow (high wind speed) conditions the accurate prediction of wind turbine thrust and power.
- Comparison with results provided by the well known $FAST^{©}$ code has shown that Method 2 yields predictions that are in good agreement with those obtained by a state-of-art BEMT approach up to $V_w = 17m/s$, whilst a better correlation with experimental data is observed above this threshold.
- Blade deformations scarcely affect turbine performance for this specific test case.
- A novel approach for the spatial integration of the additional aerodynamic states of the B-L model has been proposed. The effectiveness of this technique has been verified, showing its advantages with respect to a strip theory approach, commonly used for application of two-dimensional models in three-dimensional problems.

Finally, the aeroelastic formulation based on the FEM technique has been validated. Due to aeroelastic similarities between helicopter and wind turbine rotor blades, different types of helicopter main rotors in hovering and forward flight have been considered for validation purposes; then, blade response and performance of NREL horizontal axis wind turbine have been evaluated. Conclusions and observations can be summarized as follows:

- Making reference to helicopter rotors, structural dynamics modeling has been successfully validated by comparing mode shapes and nonrotating/rotating blade natural frequency with available experimental and numerical results.
- The aeroelastic formulation has been validated in terms of section airloads and steady state aeroelastic displacements for a hovering helicopter rotor. Furthermore, the time-history of the blade tip displacement induced by small perturbations about the hovering equilibrium condition, has been compared successfully with literature data.
- A comparison with literature data shows that the proposed tool is fully able to accurately predict time histories of the blade tip deflections and rotor hub loads.
- Application to a wind turbine test case has proven that the present solver well predicts blade deformation and delivered rotor thrust and power over a wide range of operating conditions, as shown by comparison with numerical and experimental data available in literature.

Appendix A

Derivations of terms appearing in blade energy expressions

In this appendix, procedure with which terms appearing in equations (2.19) and (2.33) are obtained, is presented. Let us consider the first term of equation (2.14). Substituting equation (2.18) into (2.15) and analyzing just the first contribution of (2.18) yields:

$$\delta U_b = \int_0^R \iint_A (E\epsilon_{xx}\delta\epsilon_{xx})\, d\eta d\zeta\, dx = \int_0^R \iint_A \left(Eu_e^{'}\delta u_e^{'}\right) d\eta d\zeta\, dx \tag{A.1}$$

Deflections are only function of the position along the span, so it can be rewritten as

$$\delta U_b = \int_0^R \left(u_e^{'}\delta u_e^{'} \iint_A E\, d\eta d\zeta\right)\, dx \tag{A.2}$$

where $EA = \iint_A E\, d\eta d\zeta$ represents the axial stiffness of the section. Finally, in nondimensional form (reference parameters are listed in Section 2.2):

$$\delta\bar{U}_b = \frac{\delta U_b}{m_0\Omega_0^2R^3} = \frac{1}{m_0\Omega_0^2R^3}\int_0^{R/R} \left(\bar{EA}m_0\Omega_0^2R^2\, \bar{u_e^{'}}\, \delta\bar{u_e^{'}}\right)\, d\bar{x}R = \int_0^1 \left(\bar{EA}\bar{u_e^{'}}\delta\bar{u_e^{'}}\right)\, d\bar{x} \tag{A.3}$$

in which $\bar{}$ indicates nondimensional quantities. $\bar{EA}\bar{u_e^{'}}$ is one term of $\bar{U}_{\bar{u_e^{'}}}$ (equation 2.19) and it represents a contribution of the elemental stiffness matrix.

For gyroscopic and mass matrix terms let us consider kinetic energy expression. For example, the following contributions for V_b and δV_b are analyzed:

$$\begin{aligned} V_b &= \dot{x}_1 \\ \delta V_b &= \delta\dot{x}_1 - \Omega\delta y_1 \end{aligned} \tag{A.4}$$

Equation (2.32) becomes

$$\delta T_b = \int_0^R \iint_A (\rho_s\dot{x}_1 \cdot (\delta\dot{x}_1 - \Omega\delta y_1))\, d\eta d\zeta\, dx \tag{A.5}$$

Considering only the first term of δV_b, remembering that equation (A.5) must to be integrated between two

different time step (see equation (2.11)), we can take time integration into the space one as follows

$$\delta\Pi = \int_{\psi_1}^{\psi_2} \left[\int_0^R \iint_A (\rho_s \dot{x}_1 \cdot \delta\dot{x}_1)\, d\eta d\zeta\, dx \right] d\psi = \iiint_V \int_{\psi_1}^{\psi_2} (\rho_s \dot{x}_1 \cdot \delta\dot{x}_1)\, d\psi\, dV \tag{A.6}$$

then integrating by parts yields:

$$\int_{\psi_1}^{\psi_2} (\rho_s \dot{x}_1 \cdot \delta\dot{x}_1)\, d\psi = \rho_s \dot{x}_1 \cdot \delta x_1 |_{\psi_1}^{\psi_2} - \int_{\psi_1}^{\psi_2} (\rho_s \ddot{x}_1 \cdot \delta x_1)\, d\psi \tag{A.7}$$

On the right hand side of equation (A.7), the first term is equal to zero for the homogeneous boundary conditions. Now, replacing equation (A.7) into (A.5), and then into (2.11) yields

$$\delta\Pi = \int_{\psi_1}^{\psi_2} \left[\int_0^R \iint_A \left[\rho_s \left(-\ddot{x}_1 \delta x_1 - \dot{x}_1 \Omega \delta y_1 \right) \right] d\eta d\zeta\, dx \right] d\psi \tag{A.8}$$

Finally, expression of these contributions of kinetic energy in nondimensional form is

$$\delta\bar{T}_b = \frac{\delta T_b}{m_0 \Omega_0^2 R^3} = \frac{1}{m_0 \Omega_0^2 R^3} \int_0^{R/R} \iint_A \rho_s \left(-\bar{\ddot{x}}_1 \Omega^2 R \delta\bar{x}_1 R - \bar{\dot{x}}_1 \Omega R \Omega \delta\bar{y}_1 R \right) d\eta d\zeta\; d\bar{x} R \tag{A.9}$$

denoting with $\mu_s = \frac{\iint_A \rho_s d\eta d\zeta}{m_0}$ the nondimensional mass section yields

$$\delta\bar{T}_b = \int_0^1 \mu_s \left[-\bar{\ddot{x}}_1 \left(\frac{\Omega}{\Omega_0} \right)^2 \delta\bar{x}_1 - \bar{\dot{x}}_1 \left(\frac{\Omega}{\Omega_0} \right)^2 \delta\bar{y}_1 \right] d\bar{x} \tag{A.10}$$

Dependence of section degrees of freedom is outlined substituting equations (2.29) and (2.18) into (A.10). For example, just considering the first term of equations (2.29) and (2.18) yields

$$\delta\bar{T}_b = \int_0^1 \mu_s \left[-\bar{\ddot{u}}_e \left(\frac{\Omega}{\Omega_0} \right)^2 \delta\bar{u}_e - \bar{\dot{u}}_e \left(\frac{\Omega}{\Omega_0} \right)^2 \delta\bar{v} \right] d\bar{x} \tag{A.11}$$

The first term of the above expression represents a contribution of $\bar{T}_{\bar{u}_e}$ (equation 2.33) and it will contribute to the elemental mass matrix, whilst the other one is a part of $\bar{T}_{\bar{v}}$ and being a Coriolis force term it will compose the gyroscopic matrix.

Centrifugal force contribution which derives from kinetic energy is here discussed. The following expressions for V_b and δV_b are analyzed:

$$\begin{aligned} V_b &= \Omega x_1 \\ \delta V_b &= \Omega \delta x_1 \end{aligned} \tag{A.12}$$

In this case, equation (2.32) is

$$\delta T_b = \int_0^R \iint_A \left(\rho_s \Omega^2 x_1 \cdot \delta x_1 \right) d\eta d\zeta\, dx \tag{A.13}$$

From equations (2.18) and (2.29), terms reported in the next expression are the only ones which are considered

$$\begin{aligned} x_1 &= x \\ \delta x_1 = \delta u &= \textstyle\int_0^x v'\delta v' dx \end{aligned} \tag{A.14}$$

So the argument of equation (A.13) in nondimensional form can be written as

$$\mu_s \left(\frac{\Omega}{\Omega_0}\right)^2 \bar{x} \cdot \int_0^{\bar{x}} v'\delta v' d\xi = \frac{d}{d\bar{x}} \int_0^{\bar{x}} \mu_s \left(\frac{\Omega}{\Omega_0}\right)^2 \bar{x} d\bar{x} \cdot \int_0^{\bar{x}} v'\delta v' d\xi \tag{A.15}$$

Denoting with $u = \int_0^{\bar{x}} v'\delta v' d\xi$ and $v = \int_0^{\bar{x}} \mu_s \left(\frac{\Omega}{\Omega_0}\right)^2 \bar{x} d\bar{x}$, knowing that $udv = uv| - \int vdu$, expression above becomes

$$\frac{d}{d\bar{x}} \int_0^{\bar{x}} \mu_s \left(\frac{\Omega}{\Omega_0}\right)^2 \bar{x} d\bar{x} \cdot \int_0^{\bar{x}} v'\delta v' d\xi = \left[\int_0^{\bar{x}} \mu_s \left(\frac{\Omega}{\Omega_0}\right)^2 \bar{x} d\bar{x} \cdot \int_0^{\bar{x}} v'\delta v' d\xi\right]_0^1 - \int_0^{\bar{x}} \mu_s \left(\frac{\Omega}{\Omega_0}\right)^2 \bar{x} d\bar{x} v'\delta v' \tag{A.16}$$

Splitting the last integral into two parts, yields

$$\left[\int_0^{\bar{x}} \mu_s \left(\frac{\Omega}{\Omega_0}\right)^2 \bar{x} d\bar{x} \cdot \int_0^{\bar{x}} v'\delta v' d\xi\right]_0^1 - \int_0^1 \mu_s \left(\frac{\Omega}{\Omega_0}\right)^2 \bar{x} d\bar{x} v'\delta v' + \int_{\bar{x}}^1 \mu_s \left(\frac{\Omega}{\Omega_0}\right)^2 \bar{x} d\bar{x} v'\delta v' \tag{A.17}$$

where the addition of the first two terms gives a null contribution whilst the last one represents part of the centrifugal force.

Appendix B

Numerical methods for aeroelastic system integration

In this section, three finite-difference schemes for the integration of the initial value problem governing rotor aeroelasticity are presented.

B.1 Crank-Nicolson algorithm

The aeroelastic system to be integrated is

$$\mathbf{M}\ddot{\mathbf{q}} + \mathbf{C}\dot{\mathbf{q}} + \mathbf{K}\mathbf{q} = \mathbf{F} \tag{B.1}$$

The Crank-Nicolson algorithm is an implicit numerical scheme applicable on first order problems. To this aim, by defining $\dot{\mathbf{q}} = \mathbf{x}$ and substituting it into equation (B.1) one obtains

$$\mathbf{M}\dot{\mathbf{x}} + \mathbf{C}\mathbf{x} + \mathbf{K}\mathbf{q} = \mathbf{F} \tag{B.2}$$

Thus, the system of N ODEs is transformed into a new system with $2N$ equations

$$\begin{cases} \dot{\mathbf{q}} = \mathbf{x} \\ \dot{\mathbf{x}} = -\mathbf{M}^{-1}\mathbf{K}\mathbf{q} - \mathbf{M}^{-1}\mathbf{C}\mathbf{x} + \mathbf{M}^{-1}\mathbf{F} \end{cases} \tag{B.3}$$

which can be put in the following matricial (normal) form

$$\begin{Bmatrix} \dot{\mathbf{q}} \\ \dot{\mathbf{x}} \end{Bmatrix} = \begin{bmatrix} \mathbf{O} & \mathbf{I} \\ -\mathbf{M}^{-1}\mathbf{K} & -\mathbf{M}^{-1}\mathbf{C} \end{bmatrix} \begin{Bmatrix} \mathbf{q} \\ \mathbf{x} \end{Bmatrix} + \begin{Bmatrix} \mathbf{O} \\ \mathbf{M}^{-1}\mathbf{F} \end{Bmatrix} \tag{B.4}$$

Introducing the following notations

$$\mathbf{z} = \begin{Bmatrix} \mathbf{q} \\ \mathbf{x} \end{Bmatrix} \quad \mathbf{A} = \begin{bmatrix} \mathbf{O} & \mathbf{I} \\ -\mathbf{M}^{-1}\mathbf{K} & -\mathbf{M}^{-1}\mathbf{C} \end{bmatrix} \quad \mathbf{f} = \begin{Bmatrix} \mathbf{O} \\ \mathbf{M}^{-1}\mathbf{F} \end{Bmatrix} \tag{B.5}$$

yields

$$\dot{\mathbf{z}} = \mathbf{A}\mathbf{z} + \mathbf{f}\left(t,\, \mathbf{z}\right) \tag{B.6}$$

Backward difference approximation is used for the velocity, vector $\mathbf{Az}$ is replaced by its mean value, whilst at each iteration step the force vector (depending on the unknown degrees of freedom) is assumed equal to that evaluated at the previous one:

$$\begin{aligned} \dot{\mathbf{z}} &= \tfrac{1}{\Delta t}\left(\mathbf{z}_{n+1} - \mathbf{z}_n\right) \\ \mathbf{Az} &= \tfrac{1}{2}\left[\left(\mathbf{Az}\right)_{\,n+1} + \left(\mathbf{Az}\right)_{\,n}\right] \\ \mathbf{f} &= \mathbf{f}_n \end{aligned} \tag{B.7}$$

Substituting equations (B.7) into the second of equations (B.4) yields the solution for the $n+1$ step

$$\mathbf{z}_{n+1} = \left(\mathbf{I} - \frac{\Delta t}{2}\mathbf{A}_{n+1}\right)^{-1}\left[\left(\mathbf{I} + \frac{\Delta t}{2}\mathbf{A}_n\right)\mathbf{z}_n + \Delta t \cdot \mathbf{f}_n\right] \tag{B.8}$$

with the initial condition $\mathbf{z}\left(0\right) = \mathbf{z}_0$. Numerical accuracy of this scheme is $O\left(\Delta t^2\right)$.

B.2 Newmark-β algorithm

The Newmark-β algorithm is a second order numerical scheme and it is a one step implicit method for solving ordinary differential equations. Second order systems can be directly integrated with this scheme without the necessity to put them in a normal form.
The following approximation for the unknown vector is used

$$\mathbf{q} = \beta\mathbf{q}_{n+1} + \left(1 - 2\beta\right)\mathbf{q}_n + \beta\mathbf{q}_{n-1} \tag{B.9}$$

whilst central difference approximations for velocity and acceleration are applied

$$\begin{aligned} \dot{\mathbf{q}} &= \gamma\tfrac{\mathbf{q}_{n+1} - \mathbf{q}_{n-1}}{\Delta t} \\ \ddot{\mathbf{q}} &= \tfrac{\mathbf{q}_{n+1} - 2\mathbf{q}_n + \mathbf{q}_{n-1}}{\Delta t^2} \end{aligned} \tag{B.10}$$

The variables β and γ are numerical parameters that control both the stability of the method and the amount of numerical damping introduced into the system by the method. The 'average acceleration' is one of the most used method in which $\beta = 0.25$ and $\gamma = 0.5$; this values assure that the scheme will be unconditionally stable and numerical damping will not be introduced in the system.
Substituting equations (B.9) and (B.10) into (B.1) yields the following expression for the vector $\mathbf{q}$ at the step $n+1$:

$$\mathbf{q}_{n+1} = -\mathbf{A}^{-1}\left[\mathbf{D}\mathbf{q}_{n-1} + \mathbf{B}\mathbf{q}_n - \mathbf{F}_n\Delta t^2\right] \tag{B.11}$$

where

$$\begin{aligned} \mathbf{A} &= \mathbf{M} + \gamma \cdot \Delta t \cdot \mathbf{C} + \beta \cdot \Delta t^2 \cdot \mathbf{K} \\ \mathbf{D} &= \mathbf{M} - \gamma \cdot \Delta t \cdot \mathbf{C} + \beta \cdot \Delta t^2 \cdot \mathbf{K} \\ \mathbf{B} &= -2 \cdot \mathbf{M} + \left(1 - 2\beta\right) \cdot \Delta t^2 \cdot \mathbf{K} \end{aligned} \tag{B.12}$$

The problem initial conditions are $\mathbf{q}(0) = \mathbf{q}_0$ and $\dot{\mathbf{q}}(0) = \dot{\mathbf{q}}_0$. Numerical accuracy of this scheme is $O\left(\Delta t^2\right)$.

B.3 Runge-Kutta algorithm

The most commonly used explicit method for the solution of first order ordinary differential equations is the fourth order Runge-Kutta algorithm. For the state space form of the aeroelastic system (B.4), already seen in Section (B.1), the solution is obtained as

$$\mathbf{z}_{n+1} = \mathbf{z}_n + \frac{1}{6}\left(\mathbf{k}_1 + 2\cdot\mathbf{k}_2 + 2\cdot\mathbf{k}_3 + \mathbf{k}_4\right) \tag{B.13}$$

where

$$\begin{aligned} \mathbf{k}_1 &= \Delta t \cdot \hat{\mathbf{f}}\left(t_n,\ \mathbf{z}_n\right) \\ \mathbf{k}_2 &= \Delta t \cdot \hat{\mathbf{f}}\left(t_n + \tfrac{\Delta t}{2},\ \mathbf{z}_n + \tfrac{1}{2}\cdot\mathbf{k}_1\right) \\ \mathbf{k}_3 &= \Delta t \cdot \hat{\mathbf{f}}\left(t_n + \tfrac{\Delta t}{2},\ \mathbf{z}_n + \tfrac{1}{2}\cdot\mathbf{k}_2\right) \\ \mathbf{k}_4 &= \Delta t \cdot \hat{\mathbf{f}}\left(t_n + \tfrac{\Delta t}{2},\ \mathbf{z}_n + \mathbf{k}_3\right) \end{aligned} \tag{B.14}$$

in which $\hat{\mathbf{f}} = \mathbf{A}\mathbf{z} + \mathbf{f}$ and the initial condition is $\mathbf{z}(0) = \mathbf{z}_0$. Thus, the fourth-order Runge-Kutta method requires four evaluations of the right-hand side for each step Δt; truncation error is of order $O\left(\Delta t^5\right)$.

B.4 Newmark-β and Crank-Nicolson combined solution scheme

This section proposes a combined solution scheme in which the second order ODEs are solved through the Newmark-β algorithm whereas the first order ones are solved by Crank-Nicolson method. Specifically, in the present thesis, first order ODEs are introduced to describe the dynamics of the additional states appearing in the Beddoes-Leishman sectional aerodynamic formulation.
In details, the aeroelastic differential system to be solved is

$$\mathbf{M}\ddot{\mathbf{q}} + \mathbf{C}\dot{\mathbf{q}} + \mathbf{K}\mathbf{q} = \mathbf{f}\left(\mathbf{x}, \dot{\mathbf{x}}, \mathbf{q}, \dot{\mathbf{q}}, \ddot{\mathbf{q}}\right) \tag{B.15}$$

where the dynamics of the additional aerodynamic states $\mathbf{x}$ is governed by the following first order ODEs

$$\dot{\mathbf{x}} = \mathbf{A}\mathbf{x} + \boldsymbol{\mathcal{F}}\left(\mathbf{q}, \dot{\mathbf{q}}\right) \tag{B.16}$$

with initial conditions $\mathbf{q}(0) = \mathbf{q}_o$, $\dot{\mathbf{q}}(0) = \dot{\mathbf{q}}_o$ and $\mathbf{x}(0) = \mathbf{x}_o$.
Following Newmark-β algorithm, the aeroelastic solution $\mathbf{q}$ can be computed at the step $n+1$, then $\boldsymbol{\mathcal{F}}_{n+1}$ is evaluated and Crank-Nicolson scheme provides the new additional aerodynamic states solution $\mathbf{x}_{n+1}$. Finally, Newmark-β is applied to calculate the new aeroelastic solution and the process is iterated up to convergence.

Appendix C

Definition of the state-space Beddoes-Leishman model matrices

The state-space constant matrices in equations (3.53) are given by

$$\mathbf{A} = \begin{bmatrix} a_{11} & 0 & 0 & 0 & 0 & 0 & 0 & 0 \\ 0 & a_{22} & 0 & 0 & 0 & 0 & 0 & 0 \\ 0 & 0 & a_{33} & 0 & 0 & 0 & 0 & 0 \\ 0 & 0 & 0 & a_{44} & 0 & 0 & 0 & 0 \\ 0 & 0 & 0 & 0 & a_{55} & 0 & 0 & 0 \\ 0 & 0 & 0 & 0 & 0 & a_{66} & 0 & 0 \\ 0 & 0 & 0 & 0 & 0 & 0 & a_{77} & 0 \\ 0 & 0 & 0 & 0 & 0 & 0 & 0 & a_{88} \end{bmatrix} \quad \mathbf{B} = \begin{bmatrix} 1 & 0.5 \\ 1 & 0.5 \\ 1 & 0 \\ 0 & 1 \\ 1 & 0 \\ 1 & 0 \\ 0 & 1 \\ 0 & 1 \end{bmatrix} \tag{C.1}$$

$$\mathbf{C} = \begin{bmatrix} c_{11} & c_{12} & c_{13} & c_{14} & 0 & 0 & 0 & 0 \\ c_{21} & c_{22} & 0 & 0 & c_{25} & c_{26} & c_{27} & c_{28} \end{bmatrix} \quad \mathbf{D} = \begin{bmatrix} \frac{4}{M} & \frac{1}{M} \\ -\frac{1}{M} & -\frac{7}{12M} \end{bmatrix} \tag{C.2}$$

where the elements in matrix $\mathbf{A}$ are given by

$$\begin{aligned} a_{11} &= -\tfrac{2V}{c} b_1 \beta^2 & a_{22} &= -\tfrac{2V}{c} b_2 \beta^2 \\ a_{33} &= -\tfrac{1}{K_\alpha T_I} & a_{44} &= -\tfrac{1}{K_q T_I} \\ a_{55} &= -\tfrac{1}{b_3 K_{\alpha M} T_I} & a_{66} &= -\tfrac{1}{b_4 K_{\alpha M} T_I} \\ a_{77} &= -\tfrac{2V}{c} b_5 \beta^2 & a_{88} &= -\tfrac{1}{K_{qM} T_I} \end{aligned} \tag{C.3}$$

while elements in matrix $\mathbf{C}$ are

$$\begin{aligned} c_{11} &= C^S_{N\alpha} \tfrac{2V}{c} \beta^2 A_1 b_1 & c_{12} &= C^S_{N\alpha} \tfrac{2V}{c} \beta^2 A_2 b_2 \\ c_{13} &= \tfrac{4}{M} \left(\tfrac{-1}{K_\alpha T_I} \right) & c_{14} &= \tfrac{1}{M} \left(\tfrac{-1}{K_q T_I} \right) \\ c_{21} &= c_{11} \left(0.25 - x_{ac} \right) & c_{22} &= c_{12} \left(0.25 - x_{ac} \right) \\ c_{25} &= \tfrac{-1}{M} \left(\tfrac{-A_3}{b_3 K_{\alpha M} T_I} \right) & c_{26} &= \tfrac{-1}{M} \left(\tfrac{-A_4}{b_4 K_{\alpha M} T_I} \right) \\ c_{27} &= -\tfrac{C^S_{N\alpha}}{16} \tfrac{2V}{c} \beta^2 b_5 & c_{28} &= \tfrac{-7}{12M} \left(\tfrac{-1}{K_{qM} T_I} \right) \end{aligned} \tag{C.4}$$

and x_{ac} is the nondimensional position of the airfoil aerodynamic centre.

Appendix D

Spatial integration technique for additional aerodynamic states

The novel approach proposed for the spatial integration of the equations describing spanwise continuous B-L aerodynamic states, $\mathbf{x}_{1-9}$, is here applied to a simple, illustrative case study. Let us consider a slender, unswept, untapered, uniform wing in uniform, rectilinear flight. For aeroelastic modelling purposes, it is suitably described by a structural dynamics bending-torsion, linear, beam-like model, combined with aerodynamic loads. This yields, for the elastic axis coinciding with the center-of-mass axis,

$$\begin{aligned} m\ddot{w} + EI_y w^{IV} &= L\left(w, \phi, \theta\right) \\ J_E\ddot{\phi} - GJ\phi^{II} &= M_E\left(w, \phi, \theta\right) \end{aligned} \tag{D.1}$$

where w is the bending displacement, ϕ is the cross-section torsion angle, θ is the undeformed wing section pitch angle with respect to freestream, m is the mass per unit length, J_E is the sectional moment of inertia about the elastic axis, whereas EI_y and GJ denote bending and torsional stiffnesses, respectively. The aerodynamic forcing terms in equation (D.1) are sectional lift, L, and moment about the elastic axis, M_E. These, under the assumption of inviscid, attached flow, might be modeled through the two-dimensional Theodorsen theory, which provides analytic expressions for aerodynamic loads on thin airfoils undergoing pitching and plunging motion [25]. In the complex-frequency domain, for $\hat{s} = s\,b/V$ representing the reduced Laplace variable, with b and V denoting, respectively, semi-chord length and freestream velocity, when elastic axis and quarter-chord line coincide it gives [25]

$$\begin{aligned} \tilde{L} &= \pi\,\rho\,b\,V\,\hat{s}\,\tilde{v}_{1/2}(\hat{s}) + 2\pi\,\rho\,V\,b\,C(\hat{s})\,\tilde{v}_{3/4}(\hat{s}) \\ \tilde{M}_E &= \pi\,\rho\,b^2\,V\,\hat{s}\,[\tilde{v}_{1/2}(\hat{s}) - 1/2\tilde{v}_{3/8}(\hat{s})] \end{aligned} \tag{D.2}$$

with $v_\xi = v_\xi(w, \phi, \theta)$ denoting relative wind upwash at the ξ chordwise position, for $0 \leq \xi \leq 1$ and $\xi = 0$ at the leading edge. The generalized Lift Deficiency Function, $C(\hat{s})$, is a transcendental function of $\hat{s}$ [63], originally derived in the frequency domain for analysis of airfoil aerodynamic response to harmonic plunge and pitch motion [25]. In order to derive a finite-state aeroelastic wing formulation, the following second-degree Pade' approximation for $C(\hat{s})$ is assumed

$$C(\hat{s}) \approx \frac{1}{2}\frac{(\hat{s}-z_1)(\hat{s}-z_2)}{(\hat{s}-p_1)(\hat{s}-p_2)} \tag{D.3}$$

that, once expanded in partial fractions, yields

$$C(\hat{s}) \approx \frac{1}{2} + \frac{a_1}{(\hat{s}-p_1)} + \frac{a_2}{(\hat{s}-p_2)} \tag{D.4}$$

with zeroes, z_1, z_2, and poles, p_1, p_2 given, for instance, in [64]. Then, combining equation (D.2) with equation (D.4), transforming into dimensional time domain, and next coupling with equation (D.1) provides the following wing aeroelastic formulation

$$\begin{aligned}
&m\,\ddot{w} + EI_y\,w^{IV} = \pi\,\rho\,b^2\,\dot{v}_{1/2} + 2\pi\,\rho\,V\,b\,[0.5\,v_{3/4} + (a_1\,V/b)\,r_1 + (a_2\,V/b)\,r_2] \\
&J_E\,\ddot{\phi} - GJ\,\phi^{II} = \pi\,\rho\,b^3\,[\dot{v}_{1/2} - 1/2\dot{v}_{3/8}] \\
&\dot{r_1} - (p_1\,V/b)\,r_1 = v_{3/4} \\
&\dot{r_2} - (p_2\,V/b)\,r_2 = v_{3/4}
\end{aligned} \tag{D.5}$$

with r_1, r_2 denoting the additional aerodynamic states introduced by the Pade' approximation for $C(\hat{s})$, which are fully equivalent to states x_1, x_2 of the B-L model applied for turbine aeroelasticity.

Observing that under small perturbation assumption, sectional downwash, v_ξ, may be expressed in terms of a linear combination of wing bending, torsion and rigid pitch attitude and that, in particular,

$$v_{3/4} = \dot{w} + b\,\dot{\phi} + V\,(\phi + \theta)$$

the additional states, r_1, r_2, are decomposed into sub-states, each depending on a different term contributing to downwash: those forced by wing bending, r_{1w}, r_{2w}, those forced by wing torsion, $r_{1\phi}, r_{2\phi}$, and those independent of wing deformation, $r_{1\theta}, r_{2\theta}$. Because of linearity of the aerodynamic model applied, this yields the following aeroelastic formulation

$$\begin{aligned}
m\ddot{w} + EI_y w^{IV} &= \pi\rho b^2\dot{v}_{1/2} + 2\pi\rho V b[0.5v_{3/4} + (a_1 V/b)(r_{1\theta} + r_{1w} + r_{1\phi}) + (a_2 V/b)(r_{2\theta} + r_{2w} + r_{2\phi})] \\
J_E\,\ddot{\phi} - GJ\,\phi^{II} &= \pi\,\rho\,b^3\,[\dot{v}_{1/2} - 1/2\dot{v}_{3/8}] \\
\dot{r}_{1\theta} - (p_1\,V/b)\,r_{1\theta} &= V\,\theta \\
\dot{r}_{1w} - (p_1\,V/b)\,r_{1w} &= \dot{w} \\
\dot{r}_{1\phi} - (p_1\,V/b)\,r_{1\phi} &= b\,\dot{\phi} + V\,\phi \\
\dot{r}_{2\theta} - (p_2\,V/b)\,r_{2\theta} &= V\,\theta \\
\dot{r}_{2w} - (p_2\,V/b)\,r_{2w} &= \dot{w} \\
\dot{r}_{2\phi} - (p_2\,V/b)\,r_{2\phi} &= b\,\dot{\phi} + V\,\phi
\end{aligned} \tag{D.6}$$

where the description of the additional aerodynamic states is fully equivalent to the model presented in equation (3.64) for wind turbine aeroelasticity.

The relevant advantage of this approach appears when the Galerkin method (perfectly suitable for aeroelastic applications) is applied for the spatial integration of the aeroelastic system. Indeed, observing that, in principle, the spanwise distribution of the additional aerodynamic states, r_1, r_2, is unknown and is not subject to specific constraints, their differential decomposition in equation (D.6) clearly suggests that the most appropriate spanwise

distribution for each sub-state coincides with that used for the variable appearing in the corresponding forcing term. Namely, for wing deformations described through the following linear combinations

$$w(x,t) = \sum_m w_m(t)\Psi_m(x), \qquad \phi(x,t) = \sum_n \phi_n(t)\Upsilon_n(x) \tag{D.7}$$

with $\Psi_m(x)$ and $\Upsilon_n(x)$ denoting suitable sets of linearly independent shape functions that satisfy the homogeneous boundary conditions, and for undeformed wing pitch angle distribution, $\theta = \theta(x)$, the additional aerodynamic states are conveniently described as

$$\begin{array}{lll} r_{1\theta}(x,t) = r_{1\theta}(t)\,\theta(x), & r_{1w}(x,t) = \sum_m r_{1w_m}(t)\Psi_m(x), & r_{1\phi}(x,t) = \sum_n r_{1\phi_n}(t)\Upsilon_n(x) \\ r_{2\theta}(x,t) = r_{2\theta}(t)\,\theta(x), & r_{2w}(x,t) = \sum_m r_{2w_m}(t)\Psi_m(x), & r_{2\phi}(x,t) = \sum_n r_{2\phi_n}(t)\Upsilon_n(x) \end{array} \tag{D.8}$$

Finally, spatial integration is completed by projecting each equation in equation (D.6) onto shape functions used for the description of the relevant variable.

Bibliography

[1] J.L.Tangler. 'The evolutionof rotor and blade design'. American Wind Energy Association WindPower 2000, Palm Springs, California. 2000.

[2] C.Bottasso, F.Campagnolo and A.Croce. 'Multi-disciplinary constrained optimization of wind turbines'. Multibody System Dynamics. 27(1). 2012.

[3] G.Marmidis, S.Lazarou and E.Pyrgioti. 'Optimal placement of wind turbines in a wind park using Monte Carlo simulation'. Renewable Energy, 33(7). 2008.

[4] C.Bak, F.Zhale, R.Bitsche, T.Kim, A.Yde, L.C.Henriksen, A.Natarajan and M.H.Hansen. 'Description of the DTU 10 MW reference wind turbine'. DTU Wind Energy Report-I-0092, Techincal University of Denmark, Fredericia. 2013.

[5] M.O.L.Hansen, J.N.Sorensen, S.Voutsinas, N.Sorensen, H.Aa. Madsen. 'State of the art in wind turbine aerodynamics and aeroelasticity'. Progress in Aerospace Sciences, 42: 285-330. 2006.

[6] J.G.Leishman. 'Challenges in modelling the unsteady aerodynamics of wind turbines'. Wind Energy, 5: 85-132. 2002.

[7] M.Carrin, R.Steiji, M.Woodgate, G.N.Barakos, X.Munduate and S.Gomez-Iradi. 'Aeroelastic analysis of wind turbines using a tightly coupled CFD-CSD method'. Journal of Fluids and Structures, 50: 392-415. 2014.

[8] D.O.Yu and O.J.Kwon. 'Predicting wind turbine blade loads and aeroelastic response using a coupled CFD-CSD method'. Renewable Energy, 70: 184-196. 2014.

[9] P.K.Chaviaropoulos, N.N.Soerensen, M.O.L.Hansen, I.G.Nikolaou, K.A.Aggelis, J.Johansen, Mac Gaunaa, T.Hambraus, H.F.von Geyr, C.Hirsch, K.Shun, S.G.Voutsinas, G.Tzabiras, Y.Perivolaris and S.Z.Dyrmose. 'Viscous and aeroelastic effects on wind turbine blades'. The VISCEL Project. Part I-II. Wind Energy, 6: 365-403, 2003.

[10] S.G.Koh and D.H.Wood. 'Formulation of a vortex wake model for horizontal-axis wind turbines'. Wind Engineering, 15: 196-210, 1991.

[11] S.Oye. 'A simple vortex model'. Proceedings of the 3rd IEA Symposium on the Aerodynamics of Wind Turbines, ETSU, Harwell (UK), 4.1-5.15. 1990.

[12] L.Greco, C.Testa and F.Salvatore. 'Design oriented aerodynamic modelling of wind turbine performance'. Journal of Physics, Conference Series, 75. 2007.

[13] P.P.Friedmann. 'Aeroelastic modeling of large wind turbines'. Journal of the American Helicopter Society. 21(4): 17-28. 1976.

[14] D.H.Hodges and E.H.Dowell. 'Nonlinear equations of motion for the elastic bending and torsion of twisted nonuniform rotor blades'. NASA TN D-7818, 1974.

[15] B.S.Kallesoe. 'Equations of motion for a rotor blade, including gravity, pitch action and rotor speed variations'. Wind Energy, 10(3): 209-230. Chichester (England). 2007.

[16] D.L.Laird. 'A numerical manufacturing and design tool odyssey'. Proceedings of AIAA/ASME. Wind Energy Symsposium. Reno, USA, 2001.

[17] D.A.Peters and R.A.Ormiston. 'The effects of second order blade bending on the angle of attack of hingeless rotor blades'. Journal of the American Helicopter Society, 18(4), October 1973.

[18] A.Datta. 'Fundamental understanding, prediction and validation of rotor vibratory loads in steady level flight'. PhD Thesis, University of Maryland, 2004.

[19] D.H.Hodges and R.Ormiston. 'Stability of Elastic Bending and Torsion of Uniform Cantilever Rotor Blades in Hover with Variable Structural Coupling'. NASA TND8192 (1976).

[20] G.Bernardini, J.Serafini, M.Molica Colella and M.Gennaretti. 'Analysis of a structural-aerodynamic fully coupled formulation for aeroelastic response of rotorcraft'. Aerospace Science and Technology, 29: 175-184, 2013.

[21] M.Gennaretti, M.Molica Colella, G.Bernardini. 'Prediction of tiltrotot vibratory loads with inclusion of wing-proprotor aerodynamic interaction'. Journal of Aircraft, 47: 71-79. 2010.

[22] M.Gennaretti and G.Bernardini. 'Aeroelastic response of helicopter rotors using a 3-D unsteady aerodynamic solver'. The Aeronautical Journal, 110, 2006.

[23] W.Johnson. 'Helicopter theory'. Princeton University Press, Princeton, NJ. 1980.

[24] T.Ashuri. 'Beyond classical upscaling. Integrated aeroservoelastic design and optimization of large offshore wind turbines'. PhD dissertation, Delft University of Technology. 2012.

[25] T.Theodorsen. 'General theory of aerodynamic instability and the mechanism of flutter'. NACA Report 496, 1935.

[26] J.G.Leishman. 'Principles of helicopter aerodynamics'. Cambridge aerospace series.

[27] J.Zhang. 'Active-passive hybrid optimization of rotor blades with trailing edge flaps'. The Pennsylvania State University, PhD Thesis, 2001.

[28] J.D.Anderson. 'Modern compressible flow. with historical perspective'. McGraw-Hill Book Co. 1982.

[29] M.H.Hansen, M.Gaunaa, and H.Aa.Madsen. 'Beddoes-Leishman Type Dynamic Stall Model in State-Space and Indicial Formulations'. Risoe Technical Report no. 1354(EN), 2004.

[30] J.G.Leishman and T.S.Beddoes. 'A Semi-Empirical Model for Dynamic Stall'. Journal of the American Helicopter Society, Vol. 34, no. 3, pp. 3-17, 1989.

[31] J.G.Leishman and G.L.Jr.Crouse. 'State-Space Model for Unsteady Airfoil Behavior and Dynamic Stall'. AIAA Paper 89-1319, pp. 1372-1383, 1989.

[32] C.Chawin. 'Nonlinear Aeroelastic Behavior of Aerofoils Under Dynamic Stall'. PhD Thesis, University of London, May 2007.

[33] H.Wagner. 'Uber die entstehung des dynamischen auftriebes von tragflugeln'. Zeitschrift fur angewandte mathematik und mechanik, 5(1): 17-35. 1925.

[34] J.G.Leishman and K.Q.Nguyen. 'State-space representation of unsteady airfoil behavior'. AIAA Journal, 28 (5). 1990.

[35] H.Lomax. 'Indicial aerodynamics'. AGARD manual on aeroelasticity. 1968.

[36] T.S.Beddoes. 'Practical computation of unsteady lift'. Vertica, 8(1). 1984.

[37] P.R.Payne. 'Helicopter dynamics and aerodynamics'. Pitman & Sons, London. 1959.

[38] M.Gennaretti and G.Bernardini. 'Novel boundary integral formulation for blade-vortex interaction aerodynamics of helicopter rotors'. AIAA Journal, 45: 175-184. 2007.

[39] L.Greco, R.Muscari, C.Testa and A.Di Mascio. 'Marine propellers performance and flow-field features prediction by a free-wake panel method'. Journal of Hydrodynamics, Ser. B, 6: 780-795, 2014.

[40] J.Martinez, L.Bernabini, O.Probst and C.Rodriguez. 'An improved BEM model for the power curve prediction of stall-regulated wind turbines'. Wind Energy, 8: 385-402, 2005.

[41] H.Snel. 'Review of the present status of rotor aerodynamics'. Wind Energy, 1:46-69, 1998.

[42] C.Lindenburg. 'Investigation into Rotor Blade Aerodynamics'. ECN-C–03-025. July 2003.

[43] S.Gupta and J.G.Leishman. 'Dynamic Stall Modelling of the S809 Aerofoil and Comparison with Experiments'. Wind Energy, Vol. 9, no. 6, pp. 521-547, 2006.

[44] W.G.Bousman. 'Evaluation of Airfoil Dynamic Stall Characteristics for Maneuverability'. Journal of the American Helicopter Society, Vol.46, no. 4, pp. 239-250, 2001.

[45] M.M.Hand, D.A.Simms, L.J.Fingersh, D.W.Jager, J.R.Cotrell, S.Schreck and S.M.Larwood. 'Unsteady aerodynamics experiment phase VI: wind tunnel test configuration and available data compaigns'. NREL/TP-500-29955, 2001.

[46] P.Giguère and M.S.Selig. 'Design of a tapered and twisted blade for the NREL combined experiment rotor'. NREL/SR-500-26173, Golden (Colorado), USA, 1999.

[47] J.Holierhoek. 'Aeroelasticity of large wind turbines'. PhD dissertation, Delft University of Technology, The Netherlands. 2008.

[48] M.Gennaretti, R.Gori, J.Serafini, G.Bernardini and F.Cardito. 'Rotor dynamic wake inflow finite-state modelling'. Proceedings of the 33rd AIAA Applied Aerodynamics Conference, Dallas (TX), 2015.

[49] M.Gennaretti and L.Greco. 'A time-dependent coefficient reduced-order model for unsteady aerodynamics of proprotors'. Journal of Aircraft, 42: 138-147. 2005.

[50] M.M.Yelmule and E.V.S.J. Anjuri. 'CFD predictions of NREL phase VI rotor experiments in NASA/AMES wind tunnel'. International Journal of Renewable Energy Research, 3: 261–269, 2013.

[51] N.N.Sorensen, J.A.Michelsen and S.Schreck. 'Navier–Stokes predictions of the NREL phase VI rotor in the NASA Ames 80ft x 120ft wind tunnel'. Wind Energy, 5: 151–169, 2002.

[52] T.Sant, G.van Kuik and G.J.W.van Bussel. 'Estimating the angle of attack from blade pressure measurements on the NREL phase VI rotor using a free wake vortex model: axial conditions'. Wind Energy, 9: 549–577, 2006.

[53] J.M.Jonkman. 'Modeling of the UAE wind turbine for refinement of FAST_AD'. NREL/TP-500-34755, Golden (Colorado), USA, 2003.

[54] P.D.Smith. 'Instabilities in time marching methods for scattering: cause and rectification'. Electromagnetics, 10: 439-451. 1990.

[55] B.P.Rynne. 'Instabilities in time marching methods for scattering problems'. Electromagnetics, 6: 129-144. 1986.

[56] L.F.Shampine and S.Thompson. 'Stiff systems'. Scholarpedia, 2(3): 2855.

[57] D.L.Sharpe. 'A Comparison of Theory and Experiment for Aeroelastic Stability of a Hingeless Rotor Model in Hover'. Proceedings of the Integrated Technology Rotor Methodology Assessment Workshop, Moffett Field (CA, USA), 1983.

[58] O.J.Kwon. 'A technique for the prediction of aerodynamics and aeroelasticity of rotor blades'. Georgia Institute of Technology. PhD Thesis, 1988.

[59] A.Calabretta, C.Testa, L.Greco and M.Gennaretti. 'Assessment of a FEM-Based Formulation for Horizontal Axis Wind Turbine Rotors Aeroelasticity'. Applied Mechanics and Materials, Vol. 798, pp. 75-84, Oct. 2015.

[60] A.Calabretta, C.Testa, L.Greco and M.Gennaretti. 'Finite element analysis of horizontal axis wind turbines performance'. Proceedings of the VI International Conference on Computational Methods in Marine Engineering, MARINE 2015, 15-17 June 2015, Rome, Italy.

[61] S.P.Breton, F.N.Coton and G.Moe. 'A study on different stall delay models using a prescribed wake vortex scheme and NREL phase VI experiment'. European wind energy conference and exhibition. Milan (Italy). 2007.

[62] A.Calabretta, M.Molica Colella, L.Greco and M.Gennaretti. 'Assessment of aerodynamics models for wind turbines aeroelasticity'. Proceedings of the Conference on Advances in Civil, Environmental and Materials Research (ACEM20014), 2014, Busan (South Korea).

[63] J.W.Edwards. 'Unsteady aerodynamic modelling and active aeroelastic control'. Stanford University, CA, SUDAAR 504, Stanford University, Stanford (California, USA), 2013.

[64] C.Venkatesan and P.P.Friedmann. 'New approach to finite-state modeling of unsteady aerodynamics'. AIAA Journal, 24: 1889–1897, 1986.

[65] A.Calabretta, M.Molica Colella, L.Greco, G.Dubbioso, C.Testa, M.Gennaretti. 'A comprehensive numerical model for horizontal axis wind turbines aeroelasticity'. Proceedings of the RUZGEM Conference. Turkey, 2013.